

UNIVERSITY OF LJUBLJANA
FACULTY OF MATHEMATICS AND PHYSICS
DEPARTMENT OF PHYSICS

Natan Osterman

Study of viscoelastic properties, interparticle potentials and self-ordering in soft matter with magneto-optical tweezers

DOCTORAL THESIS

ADVISER: assoc. prof. dr. Igor Poberaj

COADVISER: assist. prof. dr. Dušan Babič

Ljubljana, 2009

UNIVERZA V LJUBLJANI
FAKULTETA ZA MATEMATIKO IN FIZIKO
ODDELEK ZA FIZIKO

Natan Osterman

**Študij viskoelastičnih lastnosti, meddelčnih
potencialov in samourejanja v mehki snovi z
magneto-optično pinceto**

DOKTORSKA DISERTACIJA

MENTOR: izr. prof. dr. Igor Poberaj

SOMENTOR: doc. dr. Dušan Babič

Ljubljana, 2009

Zahvala

Iskreno se zahvaljujem mentorju izr. prof. dr. Igorju Poberaju in somentorju doc. dr. Dušanu Babiču za izvrstne ideje, vodenje pri raziskavah, pomoč pri izdelavi doktorskega dela in za čas, ki sta ga v zadnjih petih letih vložila vame. Dr. Jurij Kotar je izdelal odlično magnetno pinceto in mi pomagal pri njeni uporabi. Raziskave nematskih koloidov so bile uspešne zaradi izjemnega vodstva dr. Mojce Vilfan in sodelovanja prof. dr. Martina Čopiča in dr. Mihe Ravnika. Mnogo koristnih nasvetov mi je dal dr. Miha Škarabot. Pri raziskavah samourejanja koloidnih delcev v magnetnem polju ne bi šlo brez doc. dr. Primoža Zihlerla in dr. Jureta Dobnikarja. Meritve mikroeologije bakterij so potekale v sodelovanju s skupino izr. prof. dr. Davida Stoparja z Biotehniške fakultete; dr. Tjaša Danevčič in Maja Borič sta vztrajno pripravljali bakterijske vzorce, pri teoretični obravnavi mi je pomagal dr. Andrej Vilfan.

Dr. Pietro Cicuta kindly hosted me in his group at Cavendish Laboratory, Cambridge.

Uroš Jorgačevski je mojstrsko izdeloval zelene mehanske dele za eksperiment. Blaž Kavčič in mnogi drugi kolegi iz FMF in IJS so mi mnogokrat pomagali na dolgi poti do doktorata. Gospa Jasmin Anžiček je vedno prijazno našla ugodno rešitev birokratskih problemov.

Za podporo in spodbudo sem posebno hvaležen družini. Hvala Gaji, da mi vedno stoji ob strani.

Abstract

In the PhD thesis we use magneto-optical tweezers to study various aspects of soft matter systems. The first part is focused on interparticle potentials of confined nematic colloids. We precisely measure repulsive liquid crystal mediated force between two colloidal particles with quadrupolar symmetry of the director. The force is found to have $1/x^6$ dependence on separation for particle surface-to-surface separations smaller than the sample thickness. At larger separations we demonstrate that the interparticle potential decreases exponentially due to the effect of the confinement.

In the second part of the thesis we study the relationship between isotropic interparticle potentials and resulting many body structures. Using magnetic tweezers we induce various interaction potentials in two- and three dimensional systems of superparamagnetic colloidal particles. We demonstrate that a combination of perpendicular external static magnetic field and geometric confinement creates hard-core/soft-shoulder potential which stabilizes many unusual mesophases of colloidal particles. Complex interparticle potentials can be also induced by time modulation of external magnetic field. Precession of the field on a surface of a cone with a "magic" opening angle 54.7° averages out the $1/r^3$ term of dipolar interparticle interaction. We show that the local field effect gives rise to $1/r^6$ isotropic attraction between particles and that the potential is pair-wise non-additive. We demonstrate that the interaction stabilizes single colloidal chains and hexagonal close-packed colloidal sheets in 3D.

In the last part of the thesis we outline several methods that can be used with optical tweezers to measure the microrheological behavior of materials. We implement a system for passive one-particle and active one- and two-particle microrheology consisting of high-resolution video tracking module and optical tweezers for micro-manipulation of probe particles. We test the system on water and then use it to measure the mechanical properties of the growing bacterial population of *Vibrio sp.* The stiffness of the extracellular matrix is found to be very small, whereas its viscosity increases with age and reaches a maximum of approximately $\eta \approx 3.3 \times 10^{-3}$ Pas.

Keywords: magneto-optical tweezers, complex fluids, colloids, nematic liquid crystal, self-assembly, microrheology

PACS: 85.70.Sq, 47.57.-s, 61.30.Jf, 81.16.Dn, 83.85.Cg

Povzetek

Doktorsko delo obravnava raziskave mehke snovi z magneto-optično pinceto. V prvem delu se osredotočimo na meddelčne potenciale nematskih koloidov. Natančno izmerimo odbojno strukturno silo med dvema koloidnima delcema s kvadrupolno simetrijo direktorja. Ugotovimo potenčno odvisnost sile od meddelčne razdalje, ko je razdalja med površinama delcev manjša od debeline vzorca. Pri večjih razdaljah meddelčni potencial eksponentno pojema zaradi ograjenosti tekočega kristala.

V drugem delu se posvetimo povezavi med meddelčnimi potenciali in nastalimi večdelčnimi strukturami. Z magnetno pinceto induciramo razne tipe meddelčnih potencialov v dvo- in trodimenzionalnih sistemih superparamagnetnih koloidnih delcev v vodi. Pokažamo, da kombinacija pravokotnega statičnega magnetnega polja in geometrijske ograjenosti v dveh dimenzijah ustvari zmehčan izotropni odbojni potencial, ki stabilizira neobičajne mezofaze koloidnih delcev. Kompleksne meddelčne potenciale ustvarimo tudi s časovno modulacijo zunanjega magnetnega polja. Precesija polja po površini stožca z "magičnim" vršnim kotom 54.7° izpovpreči $1/r^3$ člen v interakciji. Z računom pokažemo, da je zaradi vpliva lokalnih magnetnih polj delcev interakcijski potencial izotropno privlačen z $1/r^6$ odvisnostjo in parsko neaditiven. Predstavimo stabilne večdelčne strukture v treh dimenzijah: enojne verige in tesno zložene heksagonalne "plahte".

V zadnjem delu obravnavamo nekaj metod za meritev mikroroloških lastnosti z optično pinceto. S kombinacijo optične pincete, ki služi za mikromanipulacijo sond, in modula za videomikroskopijo naredimo sistem za pasivne enodelčne ter aktivne eno- in dvodelčne mikrorološke meritve. Sistem testiramo v vodi in ga nato uporabimo za meritve mehanskih lastnosti rastoče bakterijske populacije *Vibrio sp.* Ugotovimo, da je elastičnost ekstracelularne bakterijske matrike zelo majhna, njena viskoznost pa s starostjo narašča do največje vrednosti približno $\eta \approx 3.3 \times 10^{-3}$ Pas.

Ključne besede: magneto-optična pinceta, kompleksne tekočine, koloidi, nematski tekoči kristali, samosestava, mikrorologija

PACS: 85.70.Sq, 47.57.-s, 61.30.Jf, 81.16.Dn, 83.85.Cg

Contents

1	Introduction	7
2	Experimental techniques	13
2.1	Optical tweezers	13
2.1.1	Principle of operation	14
2.1.2	Basic design	15
2.1.3	Force calibration	15
2.1.4	Experimental setup	17
2.2	Magnetic tweezers	19
2.2.1	Superparamagnetic beads	21
2.2.2	Magnetic interaction	21
2.2.3	Calibration of the magnetic force	23
2.3	Imaging	24
3	Interparticle potentials of nematic colloids	25
3.1	Introduction	25
3.1.1	Formal description of interparticle interaction	27
3.1.2	Effect of confinement	29
3.2	Experimental details	30
3.2.1	Liquid crystal	30
3.2.2	Cell preparation	30
3.2.3	Force calibration	31
3.3	Results and discussion	32
3.3.1	Motion of free beads from different starting separations	33
3.3.2	Static measurement of LC-mediated force	34
3.3.3	Dynamic measurements	35
3.3.4	Effect of confinement	36
3.3.5	Temperature dependence of interaction	38
3.4	Conclusion and outlook	39
4	Engineered potentials	41
4.1	Introduction	41
4.2	Experimental details	44
4.3	Static magnetic field in 2D system	45

4.3.1	Isotropic repulsion	45
4.3.2	Anisotropic dipolar interaction	47
4.4	Static magnetic field in quasi-2D system	49
4.4.1	Measurement of interparticle potential	50
4.4.2	Phase behavior of a system with softened repulsion	51
4.5	Static magnetic field in a 3D system	53
4.5.1	Low filling fractions	53
4.5.2	High filling fractions	55
4.6	Rotating magnetic field in 2D system	58
4.6.1	Inplane rotation of field	58
4.6.2	Rotation of tilted magnetic field	59
4.6.3	Measurement of interparticle potential	63
4.6.4	Many-body effect	64
4.6.5	Assembly of colloidal superstructures	65
4.7	Residual interaction induced at magic angle rotation	66
4.8	Conclusion and outlook	72
5	Viscoelastic properties of bacterial networks	75
5.1	Introduction	75
5.1.1	Passive microrheology	77
5.1.2	Optical tweezers microrheology	78
5.1.3	One-particle passive MR	79
5.1.4	One-particle active MR	80
5.1.5	Two-particle active MR	81
5.1.6	Rheology of bacterial networks	83
5.2	Experimental details	84
5.2.1	Preparation of bacteria	85
5.3	Results and discussion	85
5.3.1	One-particle passive MR	85
5.3.2	One-particle active MR	89
5.3.3	Two-particle active MR	93
5.4	Conclusion and outlook	96
6	Conclusion	99
A	Numerical calculation of interaction energy of N particles	103
B	Calculation of pair energy	107
C	Particle tracking algorithms	111
	Bibliography	113
	List of publications related to the work described in this thesis	119

Razširjeni povzetek v slovenskem jeziku	121
6.1 Uvod	121
6.2 Eksperimentalne metode	122
6.3 Meddelčni potencial v ograjenem nematiku	125
6.4 Samourejanje superparamagnetnih koloidov v magnetnem polju . . .	129
6.5 Viskoelastičnost bakterijskih mrež	138

Introduction

Soft matter [1, 2] are materials with structural and dynamical properties between crystals and fluids comprising a variety of physical states. Examples of such materials range from "simple systems" (liquids, liquid crystals, colloids, polymer suspensions, foams, gels...) to the most complex biological systems of different length scales (proteins, lipids, DNA, RNA molecules, membranes, vesicles, cells, tissues). In spite of various forms of soft matter materials, their properties have common physicochemical origins, such as large number of internal degrees of freedom, weak interactions between structural elements (characteristic interaction energy is comparable to room temperature thermal energy), and a delicate balance between entropic and enthalpic contributions to the free energy. Thermal fluctuations, external fields and boundary conditions therefore play a significant role in the structure and properties of these materials, while quantum aspects can be generally neglected.

Soft matter is important in a wide range of technological applications and is of fundamental relevance in such diverse fields as chemical, environmental, and food industry. Structural and packaging materials, foams and adhesives, detergents and cosmetics, paints, food additives, lubricants and fuel additives, rubber in tires, liquid crystals for display devices, are classifiable as soft matter. Over the past years, soft matter science has been largely extended in its scope from the traditional areas such as colloids, liquid crystals and polymers to the study of biological systems and the development of novel composites and microfluidic devices.

Progress in soft matter research is driven largely by the available experimental techniques. Much of the work is concerned with understanding physics at the microscopic level, especially at the micro- and nanometer length scales. This gives soft matter studies a wide overlap with nanotechnology. Experimental methods can be divided into two broad classes: techniques for *observation* and techniques for *manipulation*.

Techniques such as static and dynamic light scattering, small-angle x-ray and neutron scattering are used to observe the bulk microscopic structural behavior of investigated samples. Main direct imaging methods include electron microscopy (TEM, SEM), various optical microscopy techniques (bright field, dark field, phase contrast, DIC, fluorescence and laser confocal scanning) and atomic force microscopy.

Local micromanipulation techniques are used to locally exert forces either to move structural elements to another position or just to monitor a local response of

the material (strain/stress relationship). Typical devices used for micromanipulation of soft materials are micromanipulators, atomic force microscope, magnetic tweezers and optical tweezers.

Optical tweezers (also called "laser tweezers") are a versatile tool for manipulation of micron-sized objects such as colloidal particles or living matter (single biomolecules, cell organelles, cells). Tightly focused laser beam is used to optically trap particles with index of refraction higher than that of the surrounding medium. Optical tweezers are a non-contact method (in contrast to micromanipulator or AFM), the force is exerted locally on a specific particle, and are therefore perfect tool to manipulate them. When combined with position sensing, tweezers can be used to precisely measure or apply forces in piconewton range, which is the magnitude found in interactions between individual protein molecules.

Optical tweezers have also some disadvantages. Sometimes piconewton forces aren't sufficient; nanonewton range would be handier. Laser beam can be partially absorbed by the sample, resulting in local heating which disturbs the measurement. In some soft matter materials, such as liquid crystals, the strong electric field of the focused laser beam can disturb the material and thereby change its properties.

A complementary tool to optical tweezers are magnetic tweezers - a device used to exert a force on magnetic particles embedded in a soft matter. Basically, magnetic tweezers consist of an electric current source and a set of coils that generate gradient magnetic field in the sample which results in magnetic force acting on the particles. By appropriate design of coil geometry large magnetic gradients, exerting forces in nanonewton range, can be generated. In contrast with optical tweezers, the force acts on all embedded magnetic particles. The magnitude and the direction of the force strongly depends on a particle position due to inhomogeneous nature of magnetic field gradients.

Similar device, homogenous magnetic tweezers¹, uses homogenous magnetic field to induce forces between superparamagnetic particles, embedded in an investigated material. In zero magnetic field, the particles don't possess any magnetic dipole moment, but as soon as the external magnetic field is applied magnetic dipole moments in the field direction are induced in the particles, which then interact via standard dipole-dipole interaction. Magnetic tweezers are suitable for precise force measurements since once the magnetic properties of the particles are known, the force between two particles depends only on two known parameters: the field magnitude (which is externally controlled and constant through the sample) and the separation between the particles (which can be directly measured using digital image analysis). A disadvantage of homogenous magnetic tweezers is lack of ability to manipulate single particles.

To get "the best of both worlds" we combined optical tweezers with homogeneous magnetic tweezers into magneto-optical tweezers. This combination enables experiments that are not or are hardly feasible by the use of either method alone. We used it to study three open problems in the field of soft matter: (i) interparticle interactions in nematic colloids, (ii) relationship between interparticle potentials and resulting ordered structures in a system of superparamagnetic particles and (iii) the

¹Actually both gradient and homogenous magnetic tweezers are inappropriately called "tweezers" since they don't enable manipulation of only one particle.

rheology of complex biological system. In the following paragraphs a brief introduction to the topics of the thesis is given, whereas more comprehensive introductions are at the beginning of each chapter.

★

Colloidal particles in liquid crystals (LC) are subjected to strong and highly anisotropic long-range forces acting between them. Uniform director field of a LC gets distorted if a particle is introduced into LC. The distortion depends on the size, shape and surface properties of the particle. If the particle has spherical shape and its surface induces planar orientation of the surrounding LC molecules, then the director field exhibits quadrupolar symmetry. If the sphere's surface induces perpendicular orientation of the molecules (homeotropic anchoring), the director field exhibits dipolar or quadrupolar symmetry, depending on the anchoring strength [3, 4]. The particles together with the surrounding perturbation of the director field are often called elastic dipoles or quadrupoles.

Interactions between colloidal particles in nematic LCs have been extensively investigated experimentally using combined optical microscopy and laser tweezers. Forces between two elastic dipoles were measured statically by determining the threshold power of optical tweezers, which was required to keep the beads at a given separation [5, 6, 7, 8]. A combination of static and dynamic measurements gave the angular dependence of the force between two elastic quadrupoles [7]. Dynamic measurements, where the trajectory of a released bead was observed, were used to study interactions between elastic quadrupoles and dipoles [9, 10].

Optical tweezers are handy tool to manipulate the colloidal particles but an important aspect has to be considered when used in LC. Strong electric field of the trapping laser significantly alters director field in the vicinity of the laser focus [11] which renders results hard to interpret. The reorientational effects can be reduced by choosing low birefringent LC or lowering the laser power [7, 6] but in both cases optical trap stiffness is reduced as well. An alternative approach that completely avoids these effects is the use of magnetic particles and magnetic field for their manipulation. First report of such interaction measurement was given by Poulin et al. [12]. Static magnetic field was used to analyze forces between homeotropic particles [13].

We implemented a similar idea using combined magneto-optic tweezers, which enable manipulation of single particles using optical tweezers and generation of both attractive and repulsive forces between superparamagnetic particles by using either static or rotating magnetic field. Due to low external magnetic field applied during the experiment (less than 10 mT) the LC director was not distorted. The system was used to study the interaction between planar colloidal particles in nematic LC enclosed in a homeotropic cell. The force between two elastic quadrupoles as a function of their separation was precisely measured for various sample thicknesses to quantify the effect of LC confinement. Temperature dependence of the interaction near the nematic to isotropic phase transition was measured to obtain the critical exponent of the force.

★ ★

One of the fundamental problems of the condensed matter physics is the relationship between the interparticle interactions and the collective structural behavior of many-body systems. The topic is especially interesting from the viewpoint of self-assembly, a process in which a system components (molecules, polymers, colloids or other basic building blocks) spontaneously organize into a larger ordered and/or functional structures [14, 15]. The form of final macroscopic structure is governed by the microscopic interactions between the components. At the microscale self-assembly is present as a concept to build metamaterials (for example, colloidal particles can self-assemble into complex super-structures that could be potentially used as a photonic band-gap materials) and in the field of microfluidics (micromixers, microvalves).

The relationship between the interparticle interactions and the resulting structures in atomic and molecular systems has been investigated theoretically and numerically. However, there are no such experimental studies since manipulation of the inter-atomic potentials is impossible. Some 30 years ago colloidal systems [16] had been found to be a suitable model for condensed matter systems. Statistical mechanical concepts known from the theory of liquids can be directly applied to ensemble of colloidal particles to provide a framework for relating the microscopic properties of single particles to the macroscopic properties. Colloidal systems are suitable for observation and in addition their properties can easily be manipulated. A change of particles or solvent properties or the addition of an external field (such as electric or magnetic) alters the macroscopic behavior of the system.

Commercially available monodisperse colloidal particles are currently available only in spherical shape. The resulting interparticle potential is isotropic which limits the set of ordered phases; the most common are the hexagonal lattice in two dimensions and the face centered cubic lattice in three dimensions [17, 18]. There are two feasible routes to obtain more complex colloidal structures, either by (i) *anisotropic* interparticle interactions which can be induced by surface treatment of particles [19], external fields [20] or liquid crystalline solvent [3] or by (ii) *isotropic* interaction potentials with radial profile more complicated than a simple power law. A simple realization of such interaction is an isotropic potential with radial profile, characterized by two length scales, e.g. a combination of hard-core and softer repulsive part. Numerical simulations predict that such interparticle potential induces a variety of mesophases [21, 22, 23, 24] between the fluid and the close packed crystal.

We used magneto-optical tweezers to induce various kinds of isotropic interaction potentials in a system of superparamagnetic colloids. The combination of a static magnetic field and confinement induced complex pair potentials with radial profile that could be tailored by varying the sample cell thickness. At critical thickness the mesophases stabilized by the hard core/soft shoulder interaction potential were observed.

Complex isotropic potentials induced by rotating magnetic field were also investigated. Especially interesting interaction potential arises when the magnetic field precesses on a cone with the "magic" opening angle $\theta_p = 54.7^\circ$. The $1/r^3$ term in dipolar interaction energy between the induced magnetic dipoles of the particles vanishes but due to the effects of the local fields the effective pair potential is isotropically attractive. The type of self assembled structures in such potential was found

to depend on the filling fraction of particles. We demonstrated that such potential can be used for stabilization colloidal superstructures.

★ ★ ★

The material properties of soft matter originate from their complex structures and dynamics with multiple characteristic length and time scales. An important material property is the shear modulus, which has been traditionally measured using rheometers but in the last two decades a number of microrheological (MR) techniques, used to locally measure viscoelastic parameters, has been developed. Microrheology has several advantages compared to traditional bulk rheometry: small quantities of samples are needed; it is possible to study heterogeneous environments; the upper range of accessible frequencies is higher (up to 10^5 Hz). This enables new insights into the microscopic foundation of viscoelasticity in soft matter systems.

There are two broad classes of MR techniques: *active* and *passive*. Passive MR techniques rely on fluctuations of probe particles due to thermal noise. Typically colloidal beads with a diameter between few tens of nanometers to several micrometers are embedded in the material, their free diffusion is observed either with dynamic light scattering [25], laser tracking [26] or videomicroscopy [27] and then a linear shear modulus is calculated.

Active MR techniques involve the active manipulation of small probes. The earliest experimental implementation of active MR was based on the manipulation of magnetic beads with an external magnetic field [28] almost a century ago. Nowadays micromechanical tools such as micropipettes [29] and atomic force microscopes [30] are used to directly strain materials, while optical tweezers [31] or magnetic bead microrheometers [32, 33, 34] are used to actively manipulate microparticles embedded in materials. These measurements are similar to conventional mechanical rheological techniques in which an external stress is applied to a sample and the resultant strain is measured to obtain the shear moduli. In this case micron-sized probes locally deform the material and probe the *local* viscoelastic response. Active measurements allow the possibility of applying sufficiently large stresses to stiff materials to obtain detectable strains. They can also be used to measure non-linear behavior if sufficiently large forces are applied to strain the material beyond the linear regime.

MR methods can be further divided according to the number of used probes to *one-particle* MR, where a motion of a single probe particle is tracked using various experimental techniques to get the viscoelasticity, and to *two-particle* MR where the correlated motion of two (or more) probes is analyzed to obtain the viscoelastic properties on larger length scales. This allows the characterization of bulk material properties even in the systems that are inhomogeneous on the length scale of the probe particle.

Optical tweezers can be employed for one-particle passive MR, where a particle is trapped in a stationary trap and its fluctuations are analyzed, and for one-particle active MR, which is required when thermal fluctuations can't induce measurable level of deformation or when the high-deformation response is studied. In one-particle active MR measurement the probe particle is trapped in an optical trap which position is harmonically oscillated [31, 35]. The complex viscoelastic modulus

of the investigated media is calculated from the response of the probe particle. Two-particle active MR involves two optical traps [36]. One particle is trapped in a harmonically oscillating stiff trap and is thus actively deforming the surrounding medium, while a second particle is trapped in a weak stationary trap and is used to monitor the deformation of the medium at a desired location.

Using optical tweezers we set up a system for measurements of microrheological properties of soft materials, including complex biological systems. In one experiment we are able to perform various microrheological measurements - one-particle passive and one- and two-particle active MR - to fully characterize local viscoelastic properties of the material. We check the system on rheology of water and then use it to monitor the development of viscoelasticity of bacterial extracellular matrix.

~

The thesis is organized as follows. In the following chapter the basic principles of optical and magnetic tweezers are explained. Our combined magneto-optical tweezers setup used for micromanipulation and imaging of individual particles is described. In Chapter 3 the measurement of interparticle potential of nematic liquid crystal colloids is reported. In Chapter 4 magnetic tweezers are used to engineer potentials between superparamagnetic particles and the formation of macroscopic structures is observed. The measurement of bacterial extracellular matrix rheology using optical tweezers is described in Chapter 5. The final concluding Chapter 6 summarizes the main results and findings presented in the thesis.

Experimental techniques

In this Chapter we describe the experimental techniques used to manipulate micron-sized particles and to exert and measure piconewton forces. First, a brief theory of operation and a basic design of optical tweezers are explained and then we focus on our implementation of tweezers. It consists of three main components: 1064 nm Nd-YAG CW laser, an inverted microscope with high numerical aperture objective and beam steering system, made of two computer-controlled, orthogonally positioned acousto-optic deflectors that enable quick and precise trap positioning and strength control. Then we describe magnetic tweezers, a device consisting of a computer controlled electrical current source and 3 orthogonally placed coil pairs used to create homogenous magnetic field in a sample. The field induces magnetic dipole moments in superparamagnetic particles which results in dipolar interaction between the particles. The interaction is in general anisotropic, but if the particles are confined to two dimensions it can be made isotropically repulsive or attractive, depending on the orientation of the external magnetic field. We conclude the Chapter with a description of particle imaging and tracking system. A fast CMOS camera is used to record the videos, which are subsequently analyzed off-line with custom particle tracking software.

2.1 Optical tweezers

Optical tweezers (also called "laser tweezers") are a micromanipulation technique that uses highly focused laser beam to trap, manipulate and measure forces on micron-sized dielectric particles. The field of optical tweezing was started by Ashkin [37] in early 1970's with the demonstration that micron-sized objects with a refractive index higher than the surrounding medium are drawn towards the center of a weakly focused laser beam. The objects were confined on the optical axis and propelled in the direction of light propagation. Ashkin was able to guide the particles in a liquid or air and even trap them in an inverted geometry where the laser light pressure was balanced by the gravitation force [38].

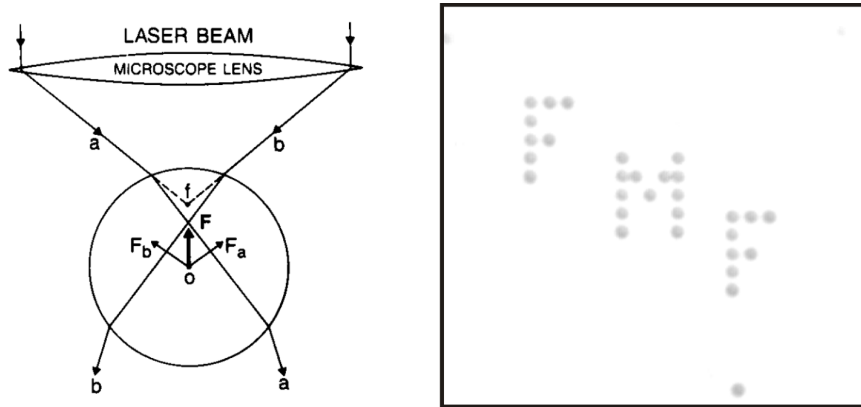


FIGURE 2.1: *Left*: Qualitative view of the trapping of a dielectric sphere. The refraction of a typical pair of rays a and b of the trapping beam gives forces F_a and F_b whose sum is pointing towards focus f . Reprinted from [46]. *Right*: Micrograph of $2\ \mu\text{m}$ silica beads trapped in 29 optical traps.

The single-beam gradient optical tweezers that enable three dimensional trapping of particles were developed by Ashkin, Chu¹, and coworkers in 1986 [39]. Since then there has been continuous development of the technique with many new applications. The technique has matured and today optical tweezers are highly effective research tool used in many fields (for a review see [40] or [41]). They are particularly important in biophysics and biology by providing a noninvasive means to manipulate cells, organelles and particles at sub-micron precision and to measure forces in the range of 0.1-100 pN [42, 43, 44, 45].

2.1.1 Principle of operation

An optical trap is created by focusing a laser beam to a diffraction-limited spot using a high numerical aperture objective. Strong gradient of light intensity near the focus creates a three dimensional potential well for objects with a refractive index higher than that of the surrounding medium. If there is no difference in refractive index between the particle and its surroundings, there is no optical force exerted on the particle. If the refractive index of the particle is lower than that of the medium, the particle is expelled from the beam center.

The optical force on a particle in a tightly focused laser beam can be decomposed into two components: a scattering component (radiation pressure) which acts in the direction of the beam propagation and a gradient component (which arises from induced dipole interactions with the electric field gradient) in the direction of highest light intensity. The particle is trapped at the point where the gradient component, the scattering component and the gravitational force balance.

The optical force acting on a particle can be analytically calculated in Rayleigh regime where a particle is much smaller or in ray optics regime where a particle is much larger than the wavelength of light used for trapping. However, optical tweezers are almost always used to trap particles with size comparable to the laser

¹Chu was awarded the Nobel Prize in Physics in 1997 for his research in cooling and trapping of atoms with laser light

wavelength, i.e. in Mie regime. The calculation of optical force on a trapped particle in this regime is quite complex and has to be performed numerically. For most applications of optical tweezers there is no need for force calculation - the tweezers are experimentally characterized and calibrated before they are used for quantitative measurements.

2.1.2 Basic design

A basic version of optical tweezers setup consists of a laser and an objective with high numerical aperture which creates one stationary optical trap. Since this would be quite limiting for experimental work, the setup usually includes a system for trap steering. There are many possibilities for a beam steering, starting from simple manual mirrors piezo-driven mirrors and more complex techniques such as spatial light modulators or acousto-optic deflectors.

Most optical tweezers are built around modified commercially available microscopes which are simultaneously used to image the sample. Often inverted microscopes are used because gravitational force on a trapped particle counteracts the scattering force so better trapping is obtain in three dimensions. The laser beam is fed into the objective using a dichroic mirror which reflects the trapping laser and transmits the light used for imaging. Samples are imaged by CMOS or CCD camera.

A laser is chosen according to optical tweezers application. Typically, a high power, single mode laser with good pointing stability and low power fluctuations is desired. For biological samples, lasers with infrared wavelengths are used to minimize laser absorption.

2.1.3 Force calibration

A spherical particle of refractive index n_2 embedded in a medium of refractive index n_1 in the proximity of a focused laser beam with wavelength larger than particle size (Rayleigh regime) "feels" a potential

$$U = -\frac{3Vn_1}{c} \left(\frac{n_2^2 - n_1^2}{n_2^2 + 2n_1^2} \right) I_0 e^{-r^2/w_0^2}, \quad (2.1)$$

where V is the volume of the particle, c is the speed of light, I_0 is the laser intensity and w_0 is beam waist diameter at the focus. The optical force on the particle as it moves from the equilibrium position $r = 0$ is

$$F = -\nabla U = \frac{6Vn_1}{cw^2} \left(\frac{n_2^2 - n_1^2}{n_2^2 + 2n_1^2} \right) I_0 e^{-r^2/w_0^2} r \hat{r}. \quad (2.2)$$

Therefore, for small displacement from the equilibrium position, an optical trap exerts an elastic force $F_i = k_i r_i$ ($i = x; y; z$), with k_i being the stiffness of the trap along a given direction. Normal optical traps are produced by a tightly focused Gaussian beams where radial forces are larger than the axial one ($k_x = k_y > k_z$).

In order to measure the force acting on a bead within an optical trap, one has to know the displacement of the bead from the equilibrium position and the stiffness of

the trap. There are numerous possibilities to measure the trap stiffness, but perhaps most popular is stiffness calibration from the power spectral density of the trapped particle's fluctuations and by the use of the equipartition theorem.

A trapped bead undergoes a confined Brownian motion. If the bead is embedded in a Newtonian fluid², the displacements from the equilibrium position $[x(t), y(t), z(t)]$ can be described by the Langevin equation³, which for one dimension is

$$m \frac{d^2 x}{dt^2} = -\gamma \frac{dx}{dt} - kx + F(t), \quad (2.3)$$

where k is the trap stiffness, m is the mass and $\gamma = 6\pi\eta a$ the viscous drag coefficient of the particle. $F(t)$ represents the random thermal force with average value of zero and a flat power spectrum

$$|F(f)|^2 = 4\gamma k_B T. \quad (2.4)$$

Micron sized particles moving with a typical velocity $\mu m/s$ have low Reynolds number, therefore the inertial term in (2.3) can be neglected. If (2.3) is transformed into frequency space, (2.4) can be used to obtain the power spectral density (PSD) of the $x(t)$ fluctuations

$$|X(f)|^2 = \frac{k_B T}{\gamma \pi^2 (f_c^2 + f^2)}, \quad (2.5)$$

where corner frequency $f_c = (k/2\pi\gamma)$ is directly related to trap stiffness k . The flat plateau at low frequencies

$$|X(0)|^2 = \frac{4\gamma k_B T}{k^2} \quad (2.6)$$

contains information on the confinement of the particle as well.

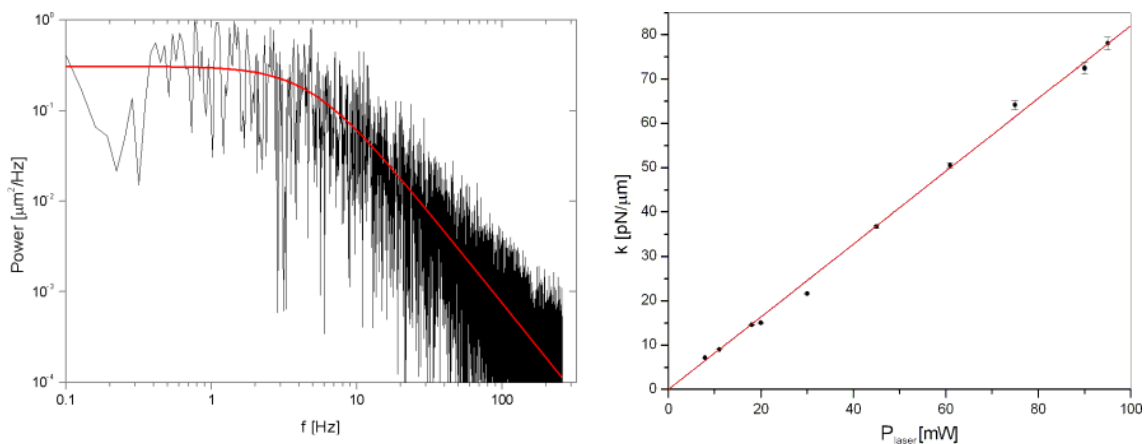


FIGURE 2.2: Calibration of optical trap stiffness. *Left*: Typical power spectral density of a trapped particle in water. Red curve is fit of (2.5) with $f_c = 4.92$ Hz. *Right*: Trap stiffness k for $1 \mu m$ silica bead trapped in water as a function of laser power.

²Newtonian fluid is a fluid whose stress is linearly proportional to strain rate. The constant of proportionality is the viscosity. Water is an example of Newtonian fluid.

³The equation holds for sufficiently stiff trap, where the particle fluctuations are always in the harmonic part of the potential well created by the trap.

The fastest way to calibrate the trap stiffness k of the trapped particle is by the use of the equipartition theorem

$$\frac{1}{2}k_B T = \frac{1}{2}k \langle x^2 \rangle. \quad (2.7)$$

By measuring the average squared displacement $\langle x^2 \rangle$ of the fluctuations of the trapped bead, the trap stiffness $k = k_B T / \langle x^2 \rangle$ is obtained.

The trap stiffness is typically linearly dependent on the power of the incident laser beam. This is demonstrated in Fig. 2.2 where we present the stiffness k as a function of laser power for $1 \mu\text{m}$ silica beads, trapped in water.

2.1.4 Experimental setup

Our laser tweezers are built around a commercial inverted optical microscope (Zeiss, Axiovert 200M) and infrared CW laser. The laser beam is spatially controlled with pair of acousto-optic deflectors (AA Opto-electronic, DTSXY-250-1064-002, frequency range of acoustic waves from 60-90 MHz), driven by a beam steering controller (Aresis, BSC-01) which enables creation of multiple optical traps and their precise positioning. A custom software running on a PC, connected with the beam steering controller and a CMOS camera (Pixelink, PLA-741), is used to manipulate the traps and record experimental videos. The schematics of experimental setup are shown in Fig. 2.4.

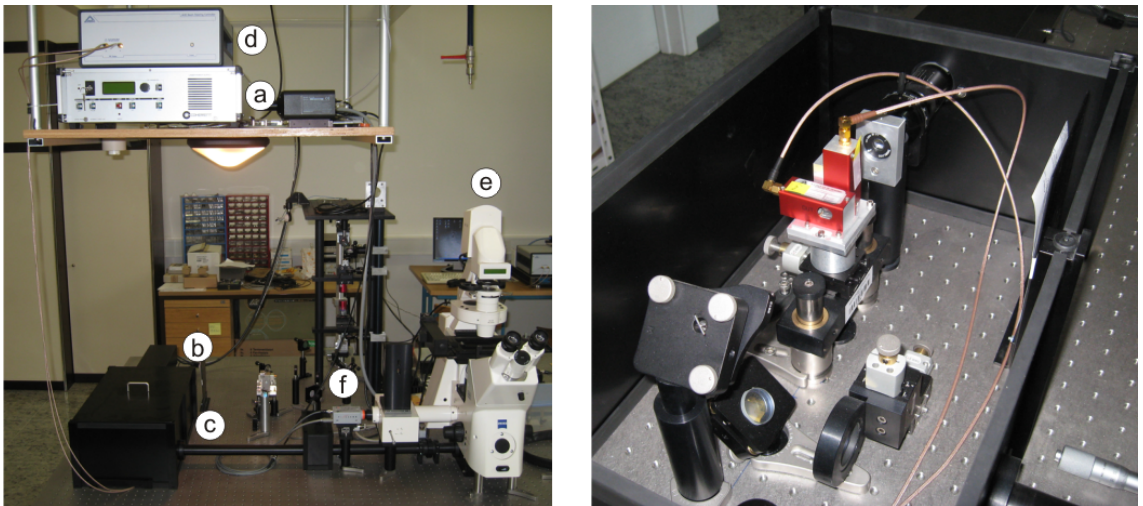


FIGURE 2.3: *Left:* Experimental setup: (a) laser diode driver, (b) laser head, (c) box with acousto-optic deflectors, (d) beam steering controller, (e) inverted microscope, (f) CMOS camera. *Right:* Acousto-optic deflectors and two mirrors for beam alignment.

The laser source is diode pumped ND:YAG laser (Coherent, Compass 1064-2500) with wavelength 1064 nm and 2.5 W of maximum power. It outputs linearly polarized Gaussian beam in TEM_{00} mode. The beam is expanded to match the entrance pupil of the acousto-optic deflectors (AODs), which are used to deflect the beam and therefore change its position in the sample.

A telescope optics and three mirrors are used to align the beam from the AODs to the entrance pupil of a high numerical aperture water immersion IR-optimized microscope objective (Zeiss, Achroplan 63x/0.9W). Optical elements in the beam path reduce the beam power. Transmission ratio from the laser through AODs, telescope optics and microscope tube lens is 28%, transmission of the objective is 51%, giving the total transmission of 14% from the laser to the sample. In experiments where AOD field flattening was used, the total transmission was additionally reduced to overall 10%.

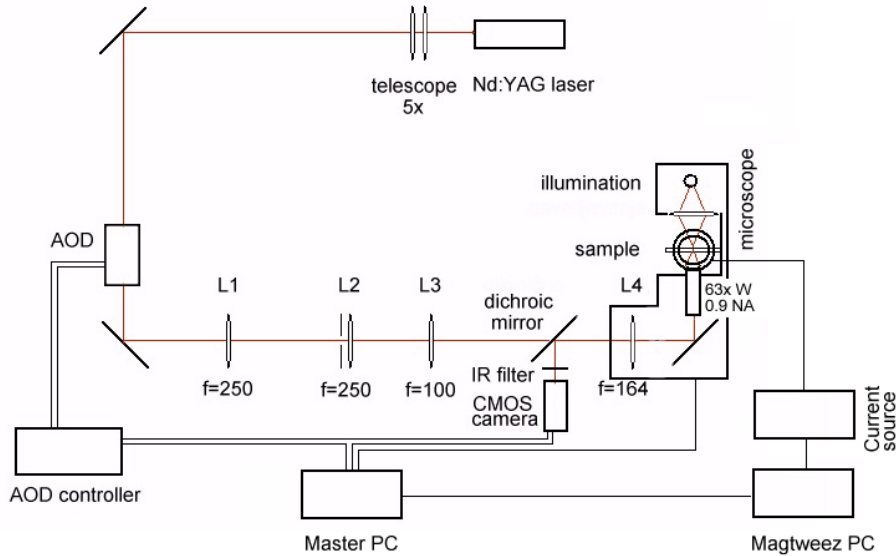


FIGURE 2.4: Schematics of the complete magneto-optical tweezers setup. Laser beam is expanded and guided through a pair of orthogonal acousto-optic deflectors to the entrance pupil of the microscope objective. Master PC controls the beam steering controller, a CMOS camera, inverted microscope and has network connection to magnetic tweezers PC that controls the current source for 3 pairs of coils mounted on the microscope.

The AOD diffraction angle depends on the frequency of acoustic wave and since the beam steering controller (BSC) creates it by direct digital synthesis (DDS) with relative frequency resolution 10^{-9} , the trap position can be changed in sub-nanometer steps. Trap stiffness is controlled by varying AOD transmission which depends on the acoustic wave amplitude. Multiple traps can be created by time sharing of the laser beam.

The beam steering controller supports up to a few thousands individual quasi-simultaneous traps or hundred thousands traps in a sequence. A pair of acoustic waves that define the trap position and stiffness (for x and y AOD) can be switched to different pair with user defined rate between 100 Hz and 100 kHz which is needed for time sharing of the beam for a creation of multiple traps. If the AOD switching rate is high then a particle, trapped in one of N simultaneous traps, "feels" as if it was trapped in a single trap with roughly N times lower stiffness. For example, if switching rate is 100 kHz and there are 10 simultaneous traps, each trap gets a laser pulse, 10^{-5} s long each $9 \cdot 10^{-5}$ s. Since the self-diffusion time ($\tau = \frac{3\pi\eta a^3}{2k_B T} \approx 0.14$ s for particles with radius $a = 0.5 \mu\text{m}$) is much longer than that, the particle is in a

quasi-stationary trapping potential. On the other side, lower AOD switching rate enable precise control over the movement of individual traps. For example, if the switching rate is 1000 Hz and there are 1000 traps, sequently arranged in a circle, the particle "feels" a single trap that is traveling around a circle with frequency 1 Hz.

The efficiency of AODs varies with frequency of acoustic wave which results in trap stiffness variation depending on its position. In order to maintain equal trap stiffness everywhere in a trapping region, AOD field flattening was used. A separate photodiode connected to the beam steering controller was used to scan the laser power across the complete trapping region. A field flattening look-up table was created and subsequently used directly in an acoustic wave generation procedure.

2.2 Magnetic tweezers

Magnetic tweezers are an instrument for exerting and measuring forces on magnetic particles using a magnetic field gradient. Forces are typically on the order of pico- to nanonewtons [34]. Due to their simple architecture, magnetic tweezers are one of the most popular and widespread biophysical techniques with typical applications in single-molecule micromanipulation, rheology of soft matter, and studies of force-regulated processes in living cells [47, 48, 49].

Another possibility to exert a magnetic force is to use a combination of a homogenous magnetic field and superparamagnetic particles. The device can't exert a force on a single isolated particle but rather a force acts between induced magnetic dipoles in the particles. By proper modulation of the amplitude and direction of the magnetic field either repulsive or attractive forces can be induced.

Homogeneous magnetic field in our setup is generated by three orthogonal sets of coils shown in Fig. 2.5. The magnitude and direction of the field are regulated by a 6-channel computer-controlled electrical current source⁴. Magnetic field components in x and y direction (xy plane is the imaging plane of the microscope) are produced by two orthogonal pairs of coils, whereas the field component in z direction (direction of optical axis) is produced by a pair of coils that are placed closer together.

To obtain a homogenous field the electrical current through two opposing coils should be the same. In left chart of Fig. 2.6 we show the measured magnetic field⁵ at sample location as a function of a current running through the corresponding pair of coils. The generated field B is proportional to the current I , $B = \alpha I$; the coefficients for field components in x and y directions are $\alpha_x = \alpha_y = 1.77$ mT/A, whereas the coefficient for z direction $\alpha_z = 10.3$ mT/A is larger because the distance between z coils is smaller than the distance between x or y coils.

The current source can generate arbitrary waveforms on six independent channels using direct digital synthesis which enables arbitrary scaling and rotation of the magnetic field in three dimensions. The maximum DC current is limited to 8A, giving a peak B_z of approximately 80 mT. However, due to high heat dissipation, DC currents up to 4 A that produce static magnetic fields up to 40 mT in z and

⁴The complete system of magnetic tweezers was designed and built by Dr. Jurij Kotar.

⁵The field was measured using high accuracy miniature ratiometric linear Hall-Effect sensor Honeywell SS496A1. The supply voltage 10 V was giving sensitivity 50 mV/mT.

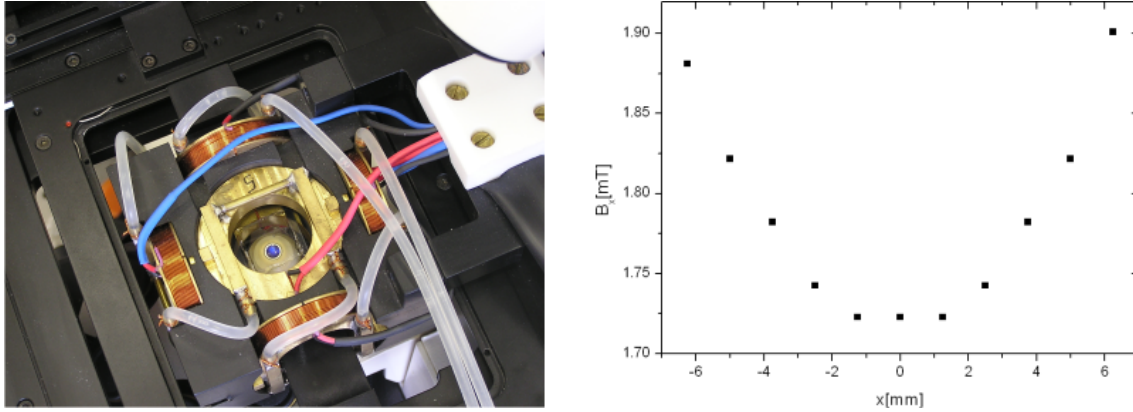


FIGURE 2.5: *Left*: Magnetic tweezers module mounted on the microscope; a sample cell and the objective are visible in the middle. Pairs of coils for field generation in x and y direction are further apart than coils for z direction. *Right*: Magnetic field in x direction as a function of position on x axis (a focal point of the microscope objective is at $x=0$).

7 mT in x and y can be produced and were found to be more than enough for all performed experiments.

Often a generation of AC magnetic field is desired. The maximum frequency of AC magnetic field is limited by the inductance of the coils and a maximum output voltage of the current source. To characterize the response of the single coil we observed the shape of generated harmonically oscillating current $I = I_0 \sin(2\pi ft)$ at fixed amplitude I_0 for different frequencies f . At given amplitude I_0 there is a maximum frequency f_{max} where the shape of the current curve is still sinusoidal, while above f_{max} the shape is distorted. In Fig. 2.6, where we present the dependence of f_{max} on coil current, one can see that for current amplitudes up to 1 A the maximum frequency of rotation is well above 1000 Hz, which was important for a generation of isotropically attractive magnetic forces.

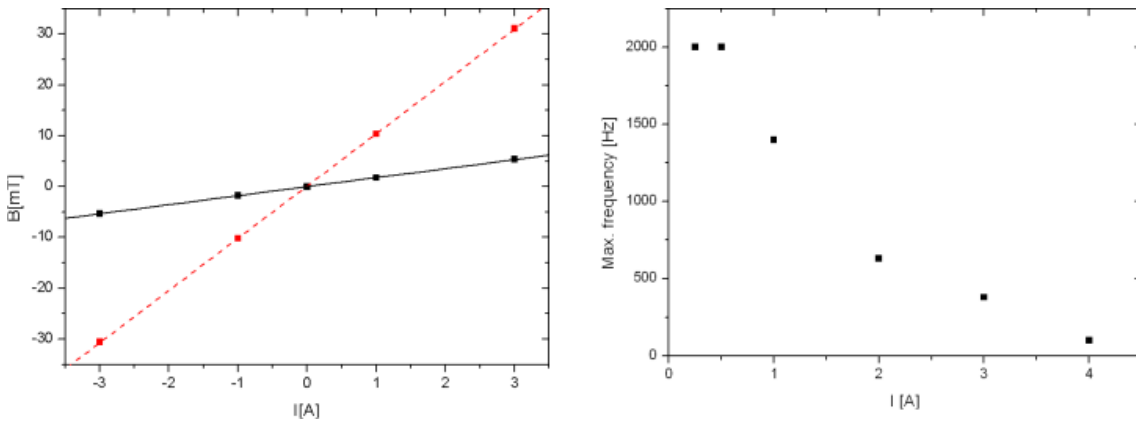


FIGURE 2.6: Calibration of magnetic tweezers. *Left*: Magnetic fields B_z and B_x at sample location as a function of coil current I . Field in z -direction B_z (red squares, red line is linear fit with slope 10 mT/A) is stronger than field in x -direction B_x (black squares, black line is linear fit with slope 1.72 mT/A) due to the layout of six coils. *Right*: Maximum frequency of non-distorted harmonic current oscillation as a function of current amplitude I .

2.2.1 Superparamagnetic beads

A superparamagnetic material is composed of small ferromagnetic clusters (e.g. crystallites) where the clusters are so small that magnetic polarization can spontaneously flip under thermal fluctuations. As a result, the material as a whole is not magnetized except when subjected to externally applied magnetic field. The rate of magnetization decay is governed by the Néel-Arrhenius equation.

External magnetic field \mathbf{B} aligns the dipole moments of superparamagnetic nanoparticles and thus induces magnetic dipole moment \mathbf{m} in the particle. The induced dipole moment is proportional to \mathbf{B} for small enough magnetic fields:

$$\mathbf{m} = \chi V \frac{\mathbf{B}}{\mu_0}. \quad (2.8)$$

Here V is the volume, χ is the magnetic susceptibility of the particle and $\mu_0 = 4\pi \times 10^{-7}$ Vs/Am is the inductance constant.

In all magnetic tweezers related experiments we used superparamagnetic beads, composed of Fe_2O_3 nanoparticles in polymer, produced by Dynal. Different sizes and surface chemistries are available under brand name *Dynabeads*. We were using the following two types, MyOne Carboxy and M450 Epoxy. Their properties, diameter σ , density ρ , magnetic susceptibility χ and magnetic dipole moment in $1mT$ magnetic field are shown in the following table (data taken from [50]).

Type	$\sigma[\mu m]$	$\rho[g/cm^3]$	χ	$\mathbf{m}[Am^2]@1mT$
MyOne Carboxy	1.05	1.7	1.37	$2.1 \cdot 10^{-16}$
M450	4.4	1.6	1.63	$1.8 \cdot 10^{-14}$

2.2.2 Magnetic interaction

The interaction of two dipoles

When magnetic dipole with magnetic moment \mathbf{m} is placed in an external magnetic field \mathbf{B} equal but opposite forces arise on each side of the dipole creating a torque

$$\mathbf{M} = \mathbf{m} \times \mathbf{B}. \quad (2.9)$$

This torque tries to align the dipole in the direction of magnetic field. The potential energy of such magnetic dipole in the external magnetic field is

$$E = -\mathbf{m} \cdot \mathbf{B}. \quad (2.10)$$

Let the magnetic dipole \mathbf{m}_1 be located at the origin of coordinate system. The magnetic field \mathbf{B}_1 created by \mathbf{m}_1 is

$$\mathbf{B}_1(\mathbf{r}) = \frac{\mu_0}{4\pi} \frac{3\mathbf{r}(\mathbf{m}_1 \cdot \mathbf{r}) - r^2 \mathbf{m}_1}{r^5}. \quad (2.11)$$

If the second magnetic dipole \mathbf{m}_2 is placed in the magnetic field of the first dipole \mathbf{B}_1 , the pair interaction energy is, according to (2.10)

$$E = -\mathbf{m}_2 \cdot \mathbf{B}_1 \quad (2.12)$$

$$E = \frac{\mu_0}{4\pi} \left(\frac{(\mathbf{m}_1 \cdot \mathbf{m}_2)}{r^3} - \frac{3(\mathbf{m}_1 \cdot \mathbf{r})(\mathbf{m}_2 \cdot \mathbf{r})}{r^5} \right) \quad (2.13)$$

The size and sign of interaction depend on the separation and the orientation of the dipoles. In the following sections we focus to particular orientations of the external magnetic field.

Static external field in 2D

Let us consider the case where two superparamagnetic beads are constrained to 2D plane (enclosed in a thin cell). Let θ denote the angle between the connecting line of the beads and the direction of the external magnetic field \mathbf{B}_0 . According to (6.3) both induced magnetic dipoles are parallel to the direction of \mathbf{B}_0 and therefore $\mathbf{m}_1 \cdot \mathbf{m}_2 = m_1 m_2$. The pair interaction energy (2.13) simplifies to

$$E = \frac{\mu_0}{4\pi} \frac{(1 - 3 \cos^2 \theta)}{r^3} m_1 m_2. \quad (2.14)$$

In the particles are of the same type and assumption that magnetic dipole moment \mathbf{m} is proportional to external magnetic field B_0 , i.e. in linear regime (6.3), the interaction can be written as

$$E = \frac{\chi^2 V^2 B_0^2}{4\pi \mu_0} \frac{(1 - 3 \cos^2 \theta)}{r^3}. \quad (2.15)$$

If the magnetic field is perpendicular to the plane of particles ($\theta = 90^\circ$), the pair interaction energy reduces to

$$E = \frac{\chi^2 V^2 B_0^2}{4\pi \mu_0 r^3}. \quad (2.16)$$

If the external magnetic field lies in the plane of particles, the pair interaction depends on θ . If \mathbf{B}_0 is perpendicular to the connecting line between the particles, the pair interaction is repulsive as in (2.16). If \mathbf{B} points in the direction of line between the particles ($\theta = 0^\circ$), the interaction is attractive and **twice as strong** as the repulsive interaction at the same separation

$$E = -\frac{\chi^2 V^2 B_0^2}{2\pi \mu_0 r^3}. \quad (2.17)$$

The expression for arbitrary configuration of particles in static magnetic field is more complicated. If the first particle is in the center of coordinate system, the second particle reside at (x, y, z) and external magnetic field is described by polar and azimuthal angles $\mathbf{B}_0 = B_0(\cos \phi \sin \theta, \sin \phi \sin \theta, \cos \theta)$, then the pair interaction energy reads

$$E = -\frac{\chi^2 V B_0^2}{4\pi \mu_0 r^5} (3(x \cos \phi \sin \theta + y \sin \phi \sin \theta + z \cos \theta)^2 - (x^2 + y^2 + z^2)) \quad (2.18)$$

With static external magnetic field it is therefore possible to induce *isotropic* repulsive interaction and *anisotropic* attraction or repulsion.

Rotating magnetic field in 2D

Time variation of the magnetic field enables another important type of interaction - *isotropic* attraction. If the magnetic field rotates in sample plane, $\mathbf{B}(\mathbf{t})_0 = B_0(\cos \omega t, \sin \omega t, 0)$, the average interaction (2.18) for one revolution of the magnetic field reads

$$\bar{E} = \frac{1}{2\pi} \int_0^{2\pi} E(x, y = 0, z = 0, \varphi, \theta = 0) d\varphi \quad (2.19)$$

$$\bar{E} = -\frac{\chi^2 V B_0^2 x^2}{8\pi^2 \mu_0 x^5} \int_0^{2\pi} (3 \cos^2 \varphi - 1) d\varphi \quad (2.20)$$

$$\bar{E} = -\frac{\chi^2 V^2 B_0^2}{8\pi \mu_0 x^3}. \quad (2.21)$$

This is isotropic attractive interaction, **fourfold weaker** than the attraction between two particles that are aligned in the direction of the field (2.17) and **twice as weak** as the isotropic repulsion (2.16) in the case of static perpendicular magnetic field.

2.2.3 Calibration of the magnetic force

Calibration of the magnetic force was performed in water. We verified the functional dependence of magnetic force and measured the scaling factor using a following procedure. Two superparamagnetic beads in thin cell were brought together using optical tweezers, then the tweezers were turned off and a magnetic field, perpendicular to the plane of particles, was turned on. The beads were pushed apart by the dipolar repulsive force F_{MR} (2.16) which was opposed by the viscous drag force F_{visc} . The dependence of interparticle separation $x(t)$ can be calculated from

$$\begin{aligned} F_{visc} &= F_{MR} \\ \frac{\dot{x}}{2} &= \frac{AI^2}{x^\beta} \\ x(t) &= \left(x_0 + \frac{2(\beta+1)AI^2}{\gamma} t \right)^{\frac{1}{\beta+1}}. \end{aligned} \quad (2.22)$$

The factor 1/2 comes from the fact that for symmetric interaction the change in the separation x is twice the dislocation of one sphere. The drag coefficient γ is given by the Stokes-Einstein relation $D = k_B T / \gamma$, where diffusion coefficient D was obtained separately by analyzing the Brownian motion of a single particle [51] when magnetic field was turned off. This was necessary since γ was unknown due to wall proximity.

The experiment was repeated many times, the videos were analyzed off-line to obtain the bead trajectories. The coefficient β was found to be 4, which confirms the dipolar nature of interaction. The measurements showed that the repulsive force can be well described by $F_{MR} = AI^2/x^4$. The same force dependence was found also for attractive force $F_{MA} = \eta AI^2/x^4$, with the factor $\eta = (0.5/5.7)^2 = 0.0091(1 \pm 0.13)$ coming from the geometry of the coils. The coefficient A depends on bead type and can vary up to 50% from batch to batch.

2.3 Imaging

The 63x water immersion objective of the inverted microscope is used both for trapping and bright field imaging using a halogen lamp as a light source. The sample is imaged with a fast complementary metal-oxide-semiconductor (CMOS) camera (PixeLink, PL-A741, 1280x960 pixels, physical pixel size $6.7 \mu\text{m}$; 1 pixel represents 106 nm in sample space) that digitizes the image to 8 bit grayscale format and sends it to a PC through USB connection. Maximum frame rate of the camera is 25 fps for full frame images, whereas smaller regions of interest (ROI) can be recorded with higher frame rates, inversely proportional to the size of ROI, i.e. maximum frame for ROI of 256x256 pixels is 450 fps. The camera can be synchronized to optical tweezers using a beam steering controller as an external trigger.

We developed a special camera control and acquisition module for the optical tweezers software. The raw data from the camera is recorded to a hard disk in a custom format, where each frame is accompanied by a frame header that carries frame specific information, such as exact frame time and positions of optical traps.

Custom particle tracking software *PartTrack* was developed for off-line analysis of experimental videos. Particle recognition and tracking of videos where objects do not come into contact is based on standard digital video microscopy tracking algorithms [52]. In more complex situations convolution techniques are applied. Tracking procedures are described in Appendix C.

Tracking accuracy depends mainly on a particle size - larger size means better accuracy. A micrometer sized bead is imaged to roughly 70 square pixels. Test videos of such bead, fixed to a surface of a sample cell, revealed that the position accuracy is better than 10 nm. Typically, we used even larger beads, therefore their positions were determined with even better accuracy.

The software is able to automatically detect multiple particles in the first frame of a video according to user-defined criteria (such as particle size) and then follow them in subsequent frames. In order to successfully create a trajectory from the array of particle positions in each frame, certain requirements have to be met, most importantly the displacements of particles from frame to frame have to be smaller than the average separation between the particles.

Interparticle potentials of nematic colloids

Magneto-optical tweezers are used for precise measurements of liquid crystal-mediated forces between colloidal particles in thin samples of nematic liquid crystals (LC). The tangential anchoring of LC molecules on the surface of a $4.4\text{-}\mu\text{m}$ bead induces a defect with quadrupolar symmetry which results in a repulsion between two particles. We measure the spatial dependence of the interparticle force over four orders of magnitude and find that it decreases proportionally to $1/x^6$, where x is the interparticle separation. The velocity with which the particles are pushed apart by the repulsive LC-mediated force also follows the same separation dependence, which reveals that the effective drag coefficient is independent of separation. Precise force measurement enables us to study the confinement effect on the interaction potential. At small separations the interparticle potential follows the power-law dependence, whereas at large separations the potential decreases exponentially with the characteristic decay length proportional to the sample thickness. The observed crossover in the potential occurs at a particle separation that is comparable to the sample thickness and is a consequence of "potential screening" by the sample cell walls.

3.1 Introduction

Liquid crystals (LCs) are materials made of rod-like molecules that exhibit a phase of matter that has properties between those of a conventional liquid, and those of a solid crystal. For instance, a LC may flow like a liquid, but have the molecules in the liquid arranged and/or oriented in a crystal-like way. Depending on the temperature or molecular concentration the molecules can self-organize and form many different types of LC phases, which can be distinguished based on their different optical properties. The various phases (called mesophases) can be characterized by the type of ordering that is present. One can distinguish positional order (whether molecules are arranged in any sort of ordered lattice) and orientational order (whether molecules are mostly pointing in the same direction), and moreover order can be either short-range (only between molecules close to each other) or long-range (extending to larger, sometimes macroscopic, dimensions).

LCs can be divided into lyotropic and thermotropic LCs. Lyotropic LCs exhibit phase transitions as a function of concentration of the mesogen in a solvent as well as temperature whereas thermotropic LCs exhibit a phase transition into the LC phase as temperature is changed. If the temperature is raised above the phase transition temperature, thermal motion will destroy the delicate cooperative ordering of the LC phase, pushing the material into a conventional isotropic liquid phase characterized by random and isotropic molecular ordering and fluid-like flow behavior. Below the transition temperature such LC might inhabit one or more phases with significant anisotropic orientational structure and long-range orientational order while still having an ability to flow.

One of the most common LC phases is the *nematic* phase, where the molecules have no positional order, but they have long-range orientational order. Molecules can flow and their center of mass positions are randomly distributed as in a liquid, but on average they point in the same direction (within each domain). The average orientation of the molecules is referred to as director \vec{n} , with the orientations \vec{n} and $-\vec{n}$ being equivalent. Most nematic molecules are rod-like with flexible tails.

Interactions between colloidal particles in LC have recently attracted considerable attention. Especially in anisotropic liquids like nematic liquid crystals, a large number of phenomena, ranging from formation of linear chains [53, 54], hexagonal patterns at surfaces [55, 56], birefringent soft solids [57], nano-colloidal structures [58] to 2-D colloidal crystals [59, 60] have been observed. The underlying mechanism giving rise to these structures are particle-induced elastic deformations in the LC director field.

Colloidal particles interact with LC molecules through surface anchoring. The surfaces of particles and cell walls can be treated with surfactants that can induce either homeotropic (perpendicular), tilted or planar (tangential) anchoring of the LC molecules. When a particle is introduced into a non-disturbed LC, the ordered orientation of LC molecules near the particle surface breaks - a *defect* is generated. Such defects in nematic LC can be either lines or points.

The distortion of the director field depends on the size, shape and surface properties of a colloidal particle. The director field around a sphere exhibits quadrupolar symmetry for planar anchoring and, depending on the anchoring strength, dipolar or quadrupolar symmetry for homeotropic anchoring [3, 4]. The particles together with the surrounding perturbation and defects are often referred to as elastic dipoles or quadrupoles. The elastic dipole can be transformed into an elastic quadrupole by an external electric field or surface confinement [61, 62].

Colloidal particles in LC are subjected to strong and highly anisotropic long-range forces acting between them. On particle scale LC acts as an elastic medium - elastic force acting on the particle tries to minimize perturbation of the director field. Interactions in nematic colloids have been extensively investigated experimentally using combined optical microscopy and laser tweezers. Forces between two elastic dipoles were measured statically by determining the threshold power of optical tweezers, which was required to keep the beads at a given separation [5, 6, 7, 8]. A combination of static and dynamic measurements gave the angular dependence of the force between two elastic quadrupoles [7]. Dynamic measurements, where the trajectory of a released bead was observed, were used to study interactions between

elastic quadrupoles and dipoles [9, 10].

Optical tweezers are handy tool to manipulate the colloidal particles but when used in LC an important aspect has to be considered. Strong electric field of the trapping laser significantly alters surrounding director field [11] which renders results hard to interpret. The reorientational effects can be reduced by choosing low birefringent LC or lowering the laser power [7, 6] - in both cases strength of the optical trap is reduced as well. An alternative approach to completely avoid these effects is to use magnetic particles and magnetic field for their manipulation. First report of particle interaction measurement in nematic colloids with magnetic colloids was given by Poulin et al. [12]; they used ferrofluid droplets immersed in NLC. External magnetic field induced dipole moments which drove the droplets apart. Static magnetic field was also used to analyze forces between homeotropic particles [13].

We used combined magneto-optic tweezers to precisely measure quadrupolar interaction between colloidal particles in nematic LC over a wide range of separations, which enabled us to observe the effect of confinement. Static and dynamic measurement were performed to determine the effective drag coefficient of the colloidal beads. The temperature dependence of interaction was measured to obtain critical exponent of the quadrupolar force.

3.1.1 Formal description of interparticle interaction

The state of deformation of an uniaxial nematic phase at a fixed temperature is described by the vectorial order parameter, the director field $\mathbf{n}(\mathbf{r})$, which describes the average orientation of nematic molecules at a given position. Orientational fluctuations of the molecules around the director can be quantified by introducing the nematic degree of order $S = \langle P_2(\cos \theta) \rangle$, where $\langle \dots \rangle$ denotes the average over an ensemble of molecules, P_2 is the second Legendre polynomial, θ is the angle between the director and the orientation of a single molecule. The director \mathbf{n} and the nematic degree of order S can be joined in a single uniaxial tensorial order parameter

$$S_{\alpha\beta} = \frac{S}{2}(3n_\alpha n_\beta - \delta_{\alpha\beta}), \quad (3.1)$$

where indices α, β run over coordinates x, y and z .

Nematic materials act as effective elastic materials if their orientational ordering is subjected to spatial variations. A free energy density is constructed phenomenologically from the scalar invariants of the order parameter tensor to penalize the elastic distortions. For small distortions it can be rewritten in terms of the director field [2]

$$f_{FO} = \frac{1}{2}K_1(\nabla \cdot \mathbf{n})^2 + \frac{1}{2}K_2(\mathbf{n} \cdot (\nabla \times \mathbf{n}))^2 + \frac{1}{2}K_3(\mathbf{n} \times (\nabla \times \mathbf{n}))^2. \quad (3.2)$$

The free energy density (3.2) is referred to as the Frank-Oseen energy density with Frank elastic constants: splay K_1 , twist K_2 , and bend elastic modulus K_3 . The elastic constants have the dimension of a force with values around 10 pN; 5CB as a typical NLC has [63]: $K_1 = 0.64 \times 10^{-11}$ N, $K_2 = 0.3 \times 10^{-11}$ N and $K_3 = 1 \times 10^{-11}$ N.

A common approximation to simplify the Frank-Oseen energy density is to use one elastic constant approximation which sets $K_1 = K_2 = K_3 = K$.

The effect of surfaces can be modeled by Rapini-Papoular anchoring potential [64]. The surface free energy density is postulated as

$$f_s = \frac{1}{2}W(1 - (\mathbf{n} \cdot \mathbf{v})^2). \quad (3.3)$$

Here W is the surface anchoring strength and \mathbf{v} is the preferred orientation of the director at the surface. The convention of strong anchoring usually corresponds to values $W \geq 10^{-5} J/m^2$, for weak anchoring values are $W \leq 10^{-7} J/m^2$.

The long-range pair potential between spherical colloidal particles suspended in a uniform liquid crystal can be analytically calculated using in approximation of multipole expansion [65, 66] (for a review see [3]). It is assumed that the director field around the particle retains the dipolar or quadrupolar structure. The one-constant Frank elastic energy for one particle with anchoring contribution is

$$F = \int \frac{1}{2}K[(\nabla \cdot \mathbf{n})^2 + (\nabla \times \mathbf{n})^2]d^3r - \oint \frac{1}{2}W(\mathbf{n} \cdot \mathbf{v})^2dS. \quad (3.4)$$

Anchoring strength W is positive in the case of homeotropic anchoring, while planar anchoring corresponds to negative W . At small anchoring $WD/K \ll 1$, where D is the diameter of the particle, or sufficiently far away from other particles, the differential equation for the minimum of the Frank free energy can be linearized and solved for director field \mathbf{n} of the particle. The superposition principle can be used to obtain superimposed director field of two particles and consequently to calculate the total elastic free energy (3.4).

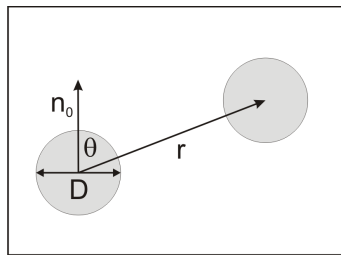


FIGURE 3.1: Schematic drawing of two colloidal beads with a diameter D immersed in nematic liquid crystal with the director \mathbf{n} .

The resulting pair interaction potential of two particles with quadrupolar structure [3] can be written as

$$U = \frac{16\pi K c_1 c_2}{r^5} \left(1 - 10 \cos^2 \theta + 105/9 \cos^4 \theta \right) \quad (3.5)$$

Here θ is the angle enclosed by the separation vector \mathbf{r} and undisturbed director \mathbf{n} (Fig. 3.1) and c_1 and c_2 are quadrupole moments¹ of the particles. If the particles

¹The magnitude of quadrupole moment is $c \propto WD^4/K$.

are identical and located in a plane, perpendicular to the director ($\theta = \pi/2$), the interaction energy reads

$$U = \frac{16\pi Kc^2}{x^5}, \quad (3.6)$$

where x is the center-to-center interparticle separation. The LC-mediated force between the particles can be obtained by differentiation of (3.6) and reads

$$F_{LC} = -\nabla U = \frac{80\pi Kc^2}{x^6}. \quad (3.7)$$

For the sake of simplicity we introduce the substitutions $C_U = \frac{16\pi Kc^2}{D^5}$ and $C_F = \frac{80\pi Kc^2}{D^6}$. The pair interaction energy can be then written as

$$U = \frac{C_U}{(x/D)^5}, \quad (3.8)$$

and the interparticle force

$$F_{LC} = \frac{C_F}{(x/D)^6}. \quad (3.9)$$

3.1.2 Effect of confinement

The energy (3.6) is calculated for interaction between particles in a bulk LC. In actual experiments LC was confined in a cell, whose walls affect the interparticle interaction. The walls limit the modes of the elastic deformation of LC and they can also directly interact with the particles via LC [67]. Therefore the confining walls may have an important effect on the particle interactions and many particle structures formed if the interparticle potential is attractive.

The effect of the confinement can be modeled with approach similar to classical electrostatics. The method of charge images has been successfully used in the field of LC to understand the interaction between defect and a flat wall [68, 69]. The interaction between two particles inside the confined cells can be interpreted as the interaction of one particle with an infinite array of the mirror images of the second particle.

Particles with tangential anchoring are analogous to electric quadrupoles and homeotropic confining surfaces to parallel conducting plates. The electrostatic potential of a quadrupole between two conducting plates can be written in the form of modified Bessel function $K_0(kx)$, which decays exponentially for large x [70]. The coefficient k is determined by the boundary conditions in the direction z , perpendicular to cell walls: the solutions are proportional to $\sin(kz)$ and equal to zero at the conducting plates. Using the analogy, assuming infinitely strong homeotropic anchoring on the cell walls and considering the symmetry of the director fields around the immersed particle, the coefficient $k = 2\pi/h$ is obtained, where h is the distance between the confining walls.

3.2 Experimental details

3.2.1 Liquid crystal

The nematic liquid crystal used in all experiments was 4-n-pentyl-4'-cyanobiphenyl, well known under its commercial name 5CB. Its molecular formula is $CH_3(CH_2)_4C_6H_4C_6H_4CN$, molecular weight 249.35, density 1.008g/ml (at 25°C) and nematic-isotropic transition temperature $T_{NI} = 35.5^\circ\text{C}$. It was purchased from Sigma-Aldrich (cat. no. 328510) and used as received without further purification.

Dried superparamagnetic spheres Dynal *Dynabeads* M-450 Epoxy Coated with a diameter of $D = 4.4 \mu\text{m}$ were suspended in the LC using a shaker and ultrasonic bath. The epoxy coated surface of the spheres induced tangential (planar) anchoring of the LC at the surface, which was confirmed by observation of beads embedded in a planar LC cell under polarizing microscope (Fig. 3.2a). Two point defects (boojums) at the poles of the sphere along the average director orientation \mathbf{n}_0 are clearly visible. We also observed formation of bead chains at an angle of approximately $\vartheta \approx 25 - 35^\circ$ with respect to the average director orientation (Fig. 3.2b). Both are consistent with the quadrupolar nature of the director configuration observed previously [71, 6].

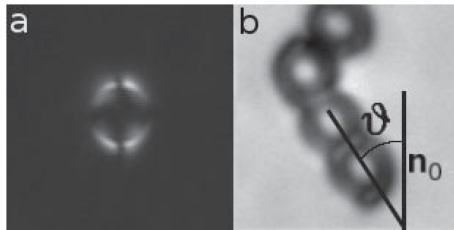


FIGURE 3.2: Superparamagnetic beads immersed in a thin planar cell with director orientation \mathbf{n}_0 . (a) Polarizing micrograph shows two boojums at the poles of the sphere. (b) Bead aggregate at an angle $\vartheta = 25 - 35^\circ$ with respect to director.

3.2.2 Cell preparation

Microscope slide and cover glass have been sonicated in deionized water with 2 wt% detergent for 20 min, rinsed under running water for 20 min, rinsed with deionized water and then blown with dry N_2 .

To induce homeotropic anchoring of LC molecules on the cell walls, the slide and cover glass were dipped in 0.5%wt solution of silane (Aldrich 435708) in water for a few seconds and then rinsed under running water for 10 minutes to remove excess silane. To achieve planar anchoring of liquid crystal on surfaces a Nylon coating and combing protocol was used: 0.25%wt Nylon 6/6 was dissolved in methanol at 50°C. The solution was spin-coated on the glass surface at 3500 rpm. The surface was then rubbed 10 times with a velvet cloth to obtain a planar homogeneous alignment.

Samples were made by sandwiching a droplet of the mixture of LC and beads between a slide and a cover slip, which ensured a homogeneous distribution of particles. The cell was glued using a UV-curing glue (Norland Optics). The thickness of the cell was controlled by the volume of the droplet ($V_{droplet} = \text{area of the cover}$

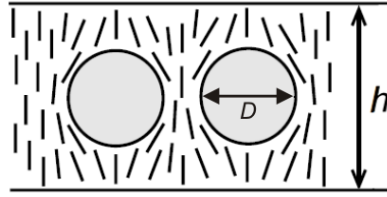


FIGURE 3.3: Side view of an experimental cell with thickness h and spheres with a diameter D . Director field configuration around two spheres inducing tangential anchoring in a homeotropic cell.

glass \times thickness). Experimental cell thicknesses were always less than twice the diameter of the spheres to prevent stacking of the beads on top of each other.

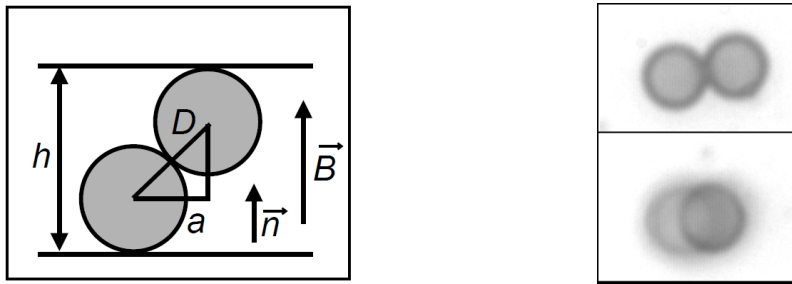


FIGURE 3.4: Cell thickness determination procedure. *Left*: Side view of a tilted pair of colloidal particles. *Right*: Top view of two beads in contact. Upper image: No magnetic field, the pair lies in the imaging plane. Lower image: Strong magnetic field perpendicular to the imaging plane reorients the pair.

The exact cell thickness h was determined after the cell was assembled. The samples always included some pairs of beads in contact which were then used as a probe to indirectly measure the thickness (Fig. 3.4). Such bead pair tries to align with field direction when the perpendicular magnetic field is applied. The cell thickness can be easily obtained from the projection of spheres' separation a as $h = D + \sqrt{D^2 - a^2}$.

3.2.3 Force calibration

Although the dependence of the magnetic force on the electric current I and particle separation x was theoretically known ($F_{MR} = \frac{AI^2}{x^4}$, see Sec. 2.2.3) the scaling coefficient A still had to be determined independently because of the slight variations of the magnetic susceptibilities of different beads. This was done by observing the motion of the same pair of beads as used in the actual force measurements.

First, the in-plane rotating magnetic field inducing attractive magnetic fields was used to brought the particles almost into contact. The field was then switched off and the particles drifted apart (Fig. 3.6, part A) due to the LC-mediated repulsive force. When Brownian motion prevailed, the magnetic field perpendicular to the plane of beads was switched on, which resulted in a repulsive magnetic force (Fig. 3.6, part B). The latter part of the trajectory can be well described if $x(t)$ dependence is

calculated from

$$F_{MR} = \frac{AI^2}{x^4} = \gamma \frac{\dot{x}}{2}, \quad (3.10)$$

where the inertial term is neglected. The factor $1/2$ comes from the fact that for symmetric interactions the change in the separation x is twice the displacement of one sphere. The coefficient γ in Eq. 3.10 is given by the Stokes-Einstein relation $\gamma = k_B T / D_c$, where k_B is the Boltzmann constant, T is the temperature, and D_c is the diffusion coefficient. The coefficient γ is obtained separately by analyzing the Brownian motion of a single particle [51]. From the measured value $\gamma = 4.2(1 \pm 0.03)$ pNs/ μm , calculated diffusion coefficient $D_c = 9.8 \times 10^{-4} \mu\text{m}^2/\text{s}$ is in a very good agreement with the diffusion coefficient obtained in [51]. From (3.10), the relation

$$x(t) = \left(\frac{10AI^2}{\gamma} (t - t_0) \right)^{1/5} \quad (3.11)$$

is obtained and fitted to experimental data (Fig. 3.6, part B). The accuracy of calibration factor obtained from the fit is approximately 10%.

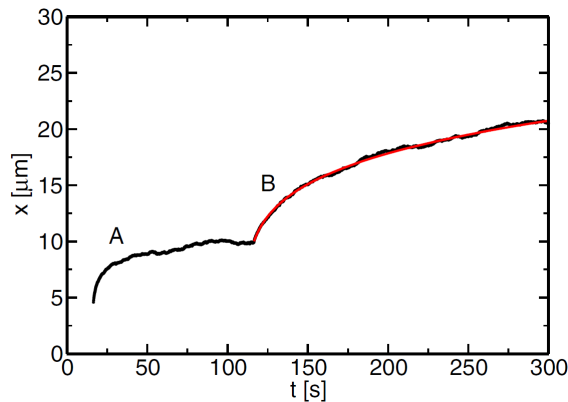


FIGURE 3.5: Interparticle separation as a function of time in force calibration procedure. When two particles are released, the LC-mediated force is pushing them apart (part A). After some time a strong repulsive magnetic field is turned on which drives the particles even further apart (part B). The motion can be well described by (3.11), shown in red.

3.3 Results and discussion

To understand the nature of the quadrupolar interparticle interactions in thin LC cells we carried out five different types of experiments:

1. *Motion of free beads*: beads were brought to various initial separations and then released. Trajectories of the motion were recorded.
2. *Static measurements of LC-mediated interaction*: magnetic tweezers were used to induce attractive magnetic force that was used to counterbalance repulsive LC-mediated force. Beads were at rest at different separations, depending on the magnitude of the magnetic force. The result was dependence of the LC repulsive force on interparticle separation.

3. *Dynamics measurements*: beads were brought almost into the contact and then released. The relationship between velocity and separation of beads was obtained.

4. *The effect of the confinement*: static interparticle interaction was measured in samples of different thicknesses. The long range decay of the interaction was obtained.

5. *The temperature dependence of the interaction*: static force measurements were performed in a temperature controlled sample.

3.3.1 Motion of free beads from different starting separations

Single colloidal particle immersed in LC host undergoes Brownian motion [51]. In the vicinity of other particles the motion of the bead is affected by LC-mediated interparticle interactions, which are repulsive in thin homeotropic cells. The effect of the repulsive interparticle force F_{LC} on particle motion was studied as follows. A suitable pair of beads with good planar surface alignment of LC (checked using crossed polarizers) was found and brought to a separation of about 10 microns with weak optical tweezers; the trap power in the sample was on the order of 10 mW. The optical tweezers were then turned off.

The rotating magnetic field inducing attractive magnetic force F_{MA} was applied to move beads to the initial separation x_0 . When the field was switched off, the beads immediately started to drift apart due to quadrupolar interparticle interaction mediated by the surrounding liquid crystal. We measured particle trajectories $x(t)$ for several different values of x_0 ranging from $4.6 \mu\text{m}$ to $5.9 \mu\text{m}$. As can be seen in Fig. 3.6 particle trajectories were independent of the initial separation x_0 . The overlapping is extremely good for small separation x , whereas at larger separations ($x > 6.5 \mu\text{m}$) the trajectories become strongly influenced by Brownian motion.

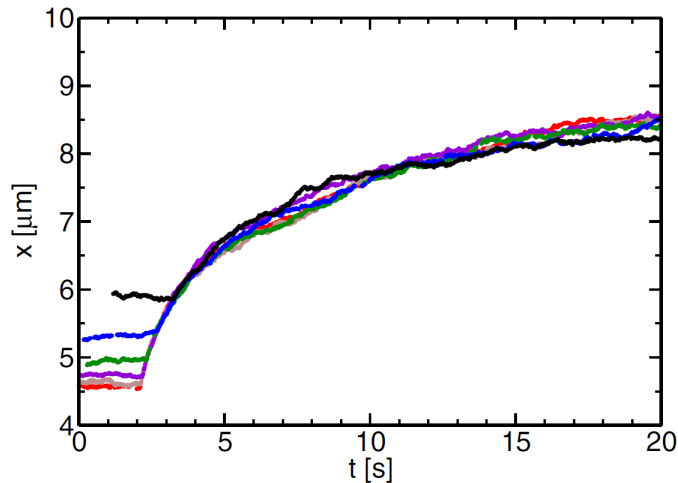


FIGURE 3.6: Interparticle separations x as a function of time t for different initial separations x_0 .

The overlapping of the trajectories indicates that the relaxation processes present in the nematic LC during the motion of the bead are fast enough to consider the

director configuration around the beads as quasistationary. Such adiabatic behavior is not surprising, as lowest relaxation times of the director field in several microns thick cells are of the order of 10 ms. This is much shorter than any characteristic time scale of the particle motion observed during measurements (for example, the characteristic time for a diffusion of the particle for its radius is approximately 10^3 s).

Another important conclusion is that the parameters of the particle motion do not depend on the velocity. This is true even for very small initial separations ($x_0 \approx 4.6 \mu\text{m}$). The motion of the particles is thus determined by the effective drag coefficient γ_{eff} , which includes the LC viscous drag, the impact of the cell walls, and the influence of LC distortions.

To obtain the effective drag coefficient $\gamma_{eff} = F_{LC}/v$ as a function of separation x , the interparticle force $F_{LC}(x)$ and the velocity of beads $v(x)$ had to be measured. In the first step, a set of static measurements was performed where the LC-mediated repulsive interparticle force F_{LC} was balanced with the attractive magnetic force F_{MA} . In the second step we did dynamic measurements where the LC repulsive force was balanced by the viscous drag force of beads drifting apart.

3.3.2 Static measurement of LC-mediated force

In the static type of measurements the LC-mediated force F_{LC} was balanced by the calibrated magnetic force F_{MA} (Fig. 3.7). There were no net motions of the beads, so all dynamic effects were excluded. Two suitable beads were found and the magnetic force was calibrated as described in Sec. 3.2.3. The beads were brought at a separation of around $10 \mu\text{m}$ using optical tweezers which were then turned off for the whole duration of the experiment. Sufficiently strong in-plane rotating magnetic field was applied which induced attractive interaction that brought beads almost² in contact (wall-to-wall separation was $0.2 \mu\text{m}$).

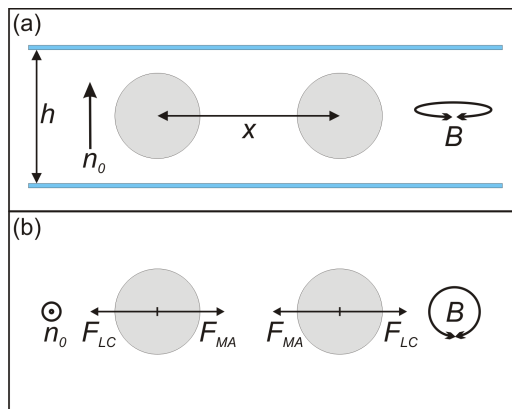


FIGURE 3.7: Experimental geometry: x is the interparticle distance, \mathbf{B} is the in-plane rotating magnetic field, \mathbf{n}_0 is the director. (a) Side view, h is the cell thickness. (b) Top view with forces acting on the beads. The LC-mediated force \mathbf{F}_{LC} is balanced by the attractive magnetic force \mathbf{F}_{MA} .

²If the magnetic field was too strong the beads came into the contact and permanently stucked together due to van der Waals interaction.

Electric current I through the coils (and thus the magnetic attractive force F_{MA}) was then reduced, so that the equilibrium interparticle distance increased. For each current setting we waited for couple of minutes for equilibration before the video recording of the beads started. For each interparticle separation 2000 frames at speed of 50 fps were captured. Typical chart of interparticle separation as a function of time at a given constant current through the coils is shown in Fig. 3.8. It can be clearly seen that the particles undergo Brownian motion around an average separation, which was in this case $5.71 \pm 0.04 \mu\text{m}$.

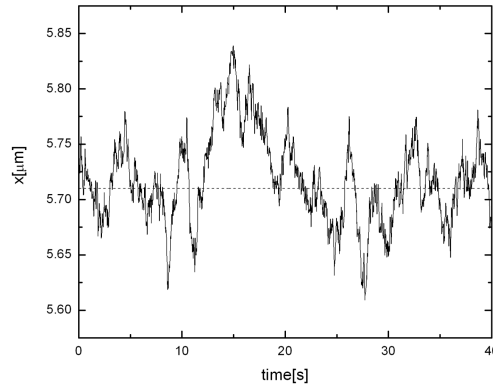


FIGURE 3.8: Interparticle distance as a function of time at some constant magnetic force. Dashed line indicates average separation.

For small magnetic attractive forces, where the bead separation x was as large as $10 \mu\text{m}$, Brownian motion prevailed. At that point, the electrical current through the coils (and therefore the F_{MA}) was increased again, and the whole cycle was repeated several times.

The experiment showed that the equilibrium positions of the particles are the same at a given current no matter whether the magnetic field was being increased or decreased. The absence of the hysteresis indicates that with varying particle separation the LC director configuration around the beads changes continuously and reversibly.

At given equilibrium bead separation the LC mediated colloidal force F_{LC} is exactly opposite to the magnetic attractive force F_{MA} . From the measured separations and known magnetic forces the dependence of the repulsive LC force F_{LC} on the interparticle separation can be obtained. The force F_{LC} as a function of normalized particle separation x/D is shown in Fig. 3.9. The fit of (3.9) to the experimental data yields $C_F = 4.69(1 \pm 0.18) \text{ pN}$.

3.3.3 Dynamic measurements

The goal of dynamic measurements was to obtain the velocity of particles drifting apart as a function of interparticle separation. The drift of beads was induced only by repulsive LC force. The measurements were actually made as a first part of force calibration procedure (Sec. 3.2.3) and then the same pair of beads was used

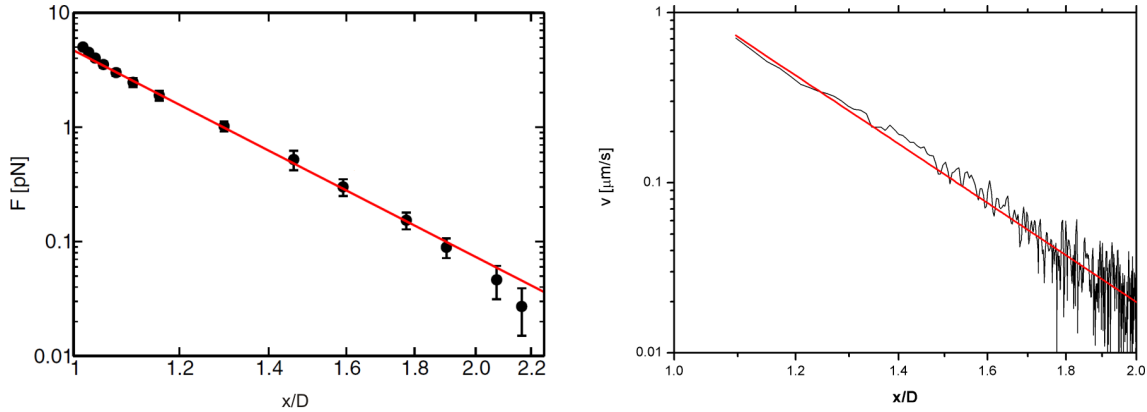


FIGURE 3.9: *Left*: Interparticle LC-mediated force as a function of interparticle separation in log-log scale. The solid red line is a fit of the power law dependence $1/(x/D)^6$ to measured data points. The deviations from the power law at small separations are expected, since (3.9) holds only for particles that are sufficiently separated. The deviations at large separations are due to the confinement effect. *Right*: Particle drift velocity as a function of normalized interparticle separation x/D in log-log scale. Particles are pushed apart only by repulsive LC-mediated force. The solid line is the best fit of $v(x) \propto 1/x^6$.

for static measurements. To recapitulate the dynamic measurements procedure, the beads were brought almost in contact using attractive magnetic field. The field was then turned off and the beads were pushed apart only by the LC-mediated repulsive force. The whole process was video recorded at 50 fps. The positions of the particles were obtained offline and used for separation and velocity determination. The LC-mediated repulsive force F_{LC} is balanced by opposing drag force γv :

$$F_{LC}(x) = \gamma v(x) = \gamma \frac{\dot{x}}{2} \quad (3.12)$$

If the force F_{LC} is the same as in static experiment ($F_{LC} \propto 1/x^6$, Eq. 3.9) then the velocity should be also dependent on separation as

$$v(x) \propto 1/x^6. \quad (3.13)$$

In Fig. 3.9 we present a typical particle drift velocity v as a function of interparticle distance x as calculated from temporal series of particle positions. Good matching between experimental data and fit with (3.13) indicates that both the interparticle force F_{LC} and the drift velocity follow the same dependence. The effective drag coefficient $\gamma_{eff} = F/v$ is therefore independent of the separation between the particles for $x > 4.9 \mu\text{m}$. The obtained value $\gamma_{eff} = 3.8(1 \pm 0.2) \text{ pNs}/\mu\text{m}$ is in agreement with the drag coefficient obtained from the analysis of single particle Brownian motion.

3.3.4 Effect of confinement

To measure the effect of the confining surfaces on the interparticle interaction, cells with different thicknesses were prepared. Here we present results from two typical

samples: sample A had a thickness of $h = 8.0(1 \pm 0.05) \mu\text{m}$, corresponding to approximately $1.8 \times D$ and sample B a thickness of $h = 6.5(1 \pm 0.05) \mu\text{m}$, equivalent to $1.5 \times D$. The measurements were made in the static mode. The force as a function of separation was then integrated in order to get the interparticle potential and the limiting value was set to zero for large interparticle separations. The obtained potential $U(x)$ is shown in Fig. 3.10 as a log-log plot. The circles and squares are the measured data for sample A and B, respectively.

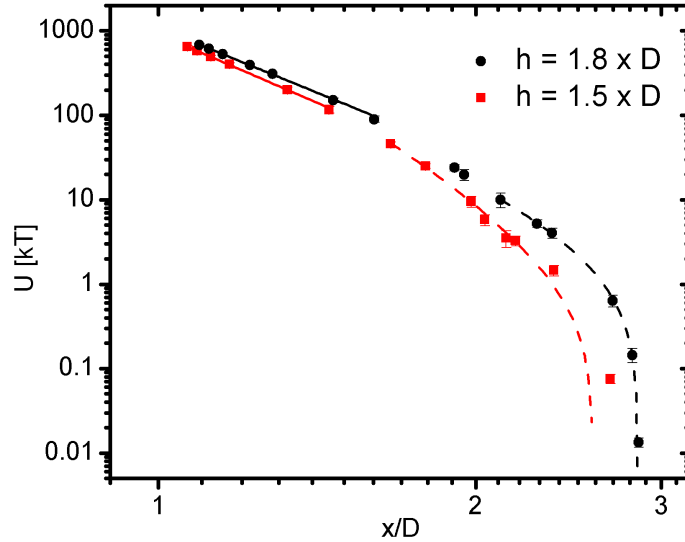


FIGURE 3.10: Logarithmic plot of the interparticle potential as a function of normalized bead separation x/D for two sample thicknesses, $h = 1.5 \times D$ (red) and $h = 1.8 \times D$ (black). The solid lines are fits of power-law functions at small separations, and dashed of exponential decay for larger separations.

In Fig. 3.10 it is clearly seen that the power-law dependence fits the measured data only for a limited range of interparticle separations. The power-law function $U(x) = C/(x/D)^\beta$ can thus be fitted only for $x \leq 0.9h$, yielding the coefficients $\beta = 5.1(1 \pm 0.05)$ and $\beta = 5.4(1 \pm 0.10)$ for samples A and B, respectively, which is consistent with theoretical prediction (3.6).

For particle separations comparable to the sample thickness, the influence of the confining walls becomes noticeable. When $x \geq 1.2h$, the interparticle potential can be successfully fitted by an exponentially decaying function,

$$U = c_2 \exp(-x/\lambda). \quad (3.14)$$

The obtained decay length is $\lambda = 1.41(1 \pm 0.10)\mu\text{m} = 0.18(1 \pm 0.15)h$ for sample A and $\lambda = 0.92(1 \pm 0.15)\mu\text{m} = 0.14(1 \pm 0.20)h$ for sample B. The decay length obtained from the electrostatic analogy (Sec. 3.1.2) for large x decays exponentially with decay length $\lambda = 0.16h$, which is in excellent agreement with the experiment.

The deviation from the power-law dependence of the interparticle potential is due to the confinement: when the separation between two particles becomes comparable to the sample thickness, the strong anchoring on the cell walls relatively reduces the effect of the beads on the director. The long range of the particle-induced deformation is thus suppressed (screened) and decays exponentially with cell thickness as a

typical length scale. Since the director deformations cause the interparticle forces, exponential decay is expected also in the force profile. Similar screening effects were extensively studied in the defect annihilation processes [72, 73].

3.3.5 Temperature dependence of interaction

Temperature dependence of the quadrupolar interaction was obtained using modified version of *static* measurements. We used servo mechanism to control the required magnetic force to hold the beads at the same separation at different temperatures. The measurement started approximately 7 K below the nematic-isotropic phase transition temperature, where two beads were brought to desired separation using optical tweezers which were then turned off. If no magnetic attractive force had been applied, the beads would have drifted apart due to repulsive LC force. Instead, magnetic attraction was controlled using closed feedback loop to keep the beads at the desired separation all the time. The error signal for servo mechanism (the deviation of interparticle distance from the desired separation) was obtained from image analysis of microscope image.

After few iterations of the feedback loop the electric current was roughly stabilized and real data acquisition began. The required current needed to keep the beads at desired separation was recorded for few minutes until enough data points were collected. The same process was then repeated at higher temperatures all the way up to the transition temperature T_{NI} .

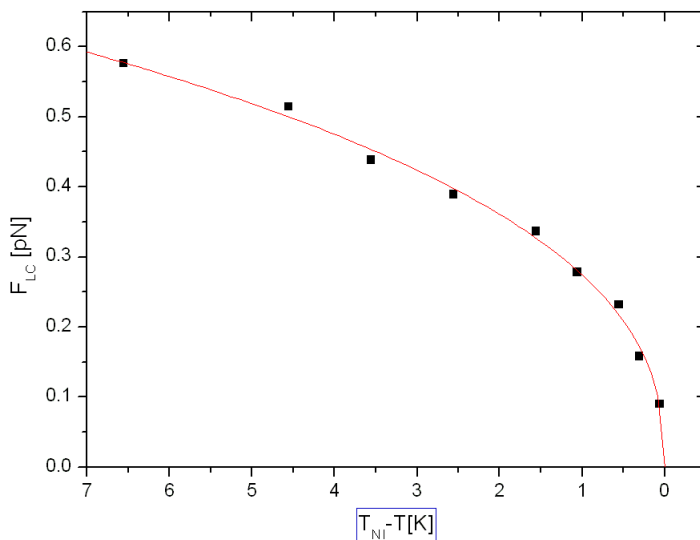


FIGURE 3.11: LC mediated force F_{LC} between two beads $6 \mu\text{m}$ apart as a function of reduced temperature $T_{NI} - T$. The solid line is the best fit of Eq. 3.15 to the data.

The recorded electric currents at each temperature were used to calculate average LC-mediated force F_{LC} . Typical relation between force F_{LC} and reduced temperature $T_{NI} - T$ for a $6 \mu\text{m}$ interparticle separation (wall-to-wall distance $1.6 \mu\text{m}$)

is shown in Fig. 3.11. The interparticle force is decreasing when the temperature is approaching the transition point. The measured data points can be fitted with power function

$$F = a(T_{NI} - T)^\beta \quad (3.15)$$

with the coefficients $a = 0.0275 \pm 0.005$ and $\beta = 0.40 \pm 0.01$.

The power law dependence of F_{LC} can be roughly explained using (3.6). If the constant quadrupole moments are assumed, then the strength of interaction depends solely on Frank elastic constant. For 5CB temperature dependence can be written in form $K(T) = a + b(T_{NI} - T)^{\beta_K}$ with $\beta_K = 0.50$ [74] which is reasonably close to the measured value of β . It has to be emphasized that (3.6) holds for quadrupolar particles in bulk LC and when the fluctuations of the director are small which is clearly not the case in our confined geometry when temperature is close to phase transition.

3.4 Conclusion and outlook

We have used magneto-optical tweezers as a tool to precisely measure the forces between microparticles in nematic liquid crystal 5CB. The particles were $4.4 \mu\text{m}$ superparamagnetic spheres with planar anchoring of LC in a thin homeotropic cell. Such particles interact as elastic quadrupoles. We performed static and dynamic measurements of the force over four orders of magnitude.

In static experiments the repulsive LC-mediated force was balanced by known attractive magnetic force. Image analysis was used to obtain equilibrium separations of the beads and from them the force vs. separation dependence was measured. The measured static LC-mediated force between particles follows $1/x^6$ dependence for wide range of interparticle separations x , starting from $x \approx 4.5 \mu\text{m}$ to $x \approx 10 \mu\text{m}$.

In the dynamic measurements the particles were first brought together with attractive magnetic field. The field was then turned off and the repulsive LC mediated force caused the particles to drift apart. From the trajectories of the particles the dependence of the average particle velocity v on the interparticle separation x was calculated.

Combining static and dynamics measurements, the effective drag coefficient $\gamma_{eff} = F_{LC}/v$ was determined and within experimental error found to be independent of the particle separation for $x > 4.9 \mu\text{m}$. This is surprising because of significant distortions in the director field around the particles, which could result in a separation dependent drag coefficient.

We have also experimentally confirmed that the interaction between colloidal particles in a confined NLC is different from that in a bulk. At particle separations, comparable to sample thickness, there is a crossover of the interparticle potential from power law to exponential decay. The decay length was found to be proportional to the sample thickness, causing a significant reduction of the potential. This occurs because the cell walls induce strong homeotropic alignment and when the separation between particles is comparable or larger than the sample thickness, the LC director field between the spheres is less disturbed and the spheres interact as if they were further apart. Such double-regime behavior and reduction of the long range of the

potential has to be considered in designing new colloidal structures, especially in samples, in which the thickness is comparable to the bead size.

The knowledge of the interparticle potential is crucial for the optimization of the assembly processes in colloidal crystals. The combined magneto-optical tweezers have proven to be successful tool for colloidal studies in liquid crystals, especially as both repulsive and attractive external force can be precisely generated without any measurable effect of the external fields on the director configuration.

Engineered potentials

We study two- and three dimensional systems of superparamagnetic colloidal particles interacting with various potentials that are induced by the external magnetic field. The static field in a 2D system induces a dipolar repulsion or attraction between the particles which results in a formation of open hexagonal lattice of particles in the former and the formation of colloidal chains in the later case. In a quasi-2D system the repulsive potential of the static field is softened which stabilizes many unusual mesophases of particles. More complex interparticle potentials can be induced by time modulation of the magnetic field. If the field precesses on a surface of a cone with the opening angle $\theta_p = 54.7^\circ$, the $1/r^3$ term of dipolar interaction vanishes. Local field effects give rise to isotropic $1/r^6$ attraction between the particles. The pair-wise non-additivity of the interaction stabilizes chains and hexagonal close-packed sheets in 3D.

4.1 Introduction

One of the fundamental problems of condensed matter physics is a relationship between interparticle interactions and collective structural behavior of many-body systems. The topic is studied theoretically and computationally using so called "forward" approach of statistical mechanics. The interparticle interactions in the system of interest are described with approximations, then numerical simulations and analytical methods are used to predict the details concerning structural, thermodynamic and kinetic properties of the system.

Self-assembly (SA) is the process in which a system components (molecules, polymers, colloids or other basic building blocks) spontaneously organize into a larger ordered and/or functional structures [14, 15]. The form of final macroscopic structure is governed by the microscopic interactions between the components. Examples of SA can be found everywhere, perhaps most spectacular in biology, including the formation of lipid bilayers to produce membranes and the protein folding. Starting at the molecular scale, SA is the fundament for crystallization of organic and inorganic molecules. At the nanoscale it is the foundation for various types of

molecular structures such as Langmuir-Blodgett films, self-assembled monolayers of amphiphilic fibres as well as superstructures built from nanoparticles. At the microscale SA is most present as a concept to build metamaterials (for example, colloidal particles can self-assemble into complex super-structures that could be potentially used as a photonic band-gap materials) and in the field of microfluidics (micromixers, microvalves).

Complementary insight into the subtle link between microscopic and macroscopic properties can be obtained by the *inverse* approach [75]. Using inverse statistical mechanical methods interparticle interactions that lead to a desired many-body structure of the system can be found. These interactions should be then somehow induced in colloidal or polymer systems to yield the desired structures at the nanoscopic and microscopic length scales. Optimized potentials would enable self-assembly of particle configurations with novel properties.

The relationship between the interparticle interactions and the resulting structures in atomic and molecular systems has been widely theoretically and numerically investigated, due to the small size of the constituents of those systems there are no experimental studies. With modern experimental techniques it is still impossible or very difficult to directly observe an atomic or molecular system and access the typical time scales. Even if direct observation is achievable, manipulation of the inter-atomic potentials is impossible.

Some 30 years ago colloidal systems [16] had been found to be suitable model for condensed matter systems. Statistical mechanical concepts known from the theory of liquids can be directly applied to an ensemble of colloidal particles to provide a framework for relating the microscopic properties of single particles to the macroscopic properties of the whole ensemble. The phase behavior of colloidal systems, such as freezing and melting of colloidal crystals, shows striking resemblance to that of atomic or molecular systems.

The colloidal systems overcome all difficulties that prevent direct study of atomic systems. Larger size and slower dynamics of colloidal particles ($a = 1 \text{ nm} - 1 \text{ }\mu\text{m}$; $\tau = 1 \text{ ms} - 1 \text{ s}$) allow the use of readily available experimental techniques, such as optical microscopy, confocal laser scanning microscopy, static and dynamic light scattering, small angle X-ray scattering and neutron scattering, to probe the colloidal suspensions. Typical time scales for processes within colloidal systems are long enough to allow the monitoring of real-time dynamics of the particles using optical microscopy. In addition, properties of colloidal systems can be manipulated: a change of a number density (simple addition of more particles into the system) can be enough to induce a phase transition. Changes of particle or solvent properties or application of an external field (such as electric or magnetic) alters the macroscopic behavior of the system.

The limitation of colloidal systems is the spherical shape of most kinds of available monodisperse colloidal particles which results in an *isotropic* interparticle potential. This is the reason why the most common ordered structures are the hexagonal lattice in two dimensions and the face-centered cubic lattice in three dimensions [17, 18].

There are two routes to more complex colloidal structures. It is clear that *anisotropic* pair potentials stabilize new kinds of structures that are not known in

systems with isotropic repulsion or attraction. Anisotropic interparticle interactions can be induced by surface treatment of particles [19], external fields [20] or liquid crystalline solvent [3]. Another, less obvious path to new types of ordered structures are *isotropic* interaction potentials with radial profile different from the usual power law dependence of common potentials.

A simple realization of such modified interaction potential is an isotropic interaction with radial profile, characterized by two length scales, e.g. a combination of hard-core and softer repulsive part. If the ratio between the ranges of the soft shoulder and the core is around 2, numerical simulations predict that such interparticle potential induces a variety of mesophases [21, 22, 23] between the fluid and the close packed crystal. In two dimensions simulations predict loose and dense hexagonal lattice, liquids of monomers, dimers and trimers, stripe and labyrinthine phases, honeycomb structure etc. Similar behavior has been predicted also in systems of paramagnetic particles limited to 2D plane, interacting with a combination of a dipolar repulsion (induced by perpendicular magnetic field) and a Lennard-Jones interaction [76]. For large shoulder/core ratios, the set of mesophases reduces to micellar, lamellar, and inverted micellar structure [24].

In this Chapter we present a study of a two- and three dimensional systems of micrometer sized superparamagnetic colloidal beads interacting with various types of potentials that were induced by the external magnetic field. The interparticle interaction is a combination of the excluded volume interaction (hard-core potential) and the magnetic interaction between the induced magnetic dipole moments of particles. The contribution of other characteristic colloidal interactions, such as electrostatic and van der Waals interaction, is negligible. We begin with the simplest configuration, a 2D system of particles in an external static magnetic field, which depending on its orientation induces a dipolar repulsion or attraction between the particles.

We then concentrate solely on the radially isotropic pair potentials, achieved by the magnetic field perpendicular to the sample plane. In two dimensional system such field induces $1/r^3$ dipolar repulsion that stabilizes the hexagonal lattice regardless of the surface filling fraction of particles. If a system is quasi two-dimensional (the particles have a limited degree of freedom to move in the vertical direction) the vertical static magnetic field induces isotropic pair potential, whose radial profile can be tailored by varying the sample cell thickness. Depending on the surface filling fraction of particles it stabilizes a lot of mesophases that have been theoretically predicted.

In the second part of the Chapter, the focus is on the complex isotropic potentials induced by the rotating magnetic field. Especially interesting potential arises when the magnetic field precesses on a cone with the "magic" opening angle $\theta_p = 54.7^\circ$, which causes that the $1/r^3$ term of the dipolar interaction vanishes. Due to the residual interactions between the particles the interaction potential is isotropically attractive with $1/r^6$ separation dependence. The Chapter is concluded with a demonstration of stable structures induced by this potential.

4.2 Experimental details

Particles used in the experiments were superparamagnetic spheres with diameter $\sigma = 1.05 \mu\text{m}$ (Dynabeads, MyOne Carboxy) suspended in the original Dynabeads solution. The solution efficiently prevented van der Waals interaction between the particles, so no aggregation was observed. Electrical charge on the beads was heavily screened with estimated screening length of a few nanometers.

The interaction between the particles was induced by the external magnetic field, which was generated by three orthogonal pairs of coils as described in Sec. 2.2.

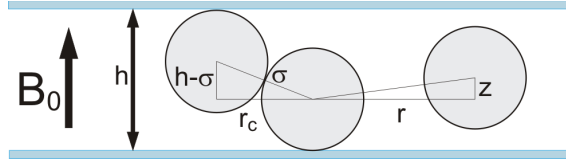


FIGURE 4.1: Side view of the experimental cell of thickness h with 3 colloidal beads of diameter σ . The external magnetic field \mathbf{B}_0 is transverse to the cell walls.

The colloidal suspension was introduced into the wedge shaped sample cell formed by $150 \mu\text{m}$ thick microscope cover glasses. When the thickness had to be precisely known, the cells were built from two $500 \mu\text{m}$ thick glasses in order to minimize bending of the cell walls. These cells were assembled under monochromatic light where the exact thickness map could be determined by the observation of fringes.

One of the crucial external parameters was the cell thickness: if it was just slightly more than the bead diameter, the particles were confined to one plane and the system was considered to be two-dimensional. Quasi 2D system was realized in a thicker part of the cell, where particles had also some limited freedom of movement in the transverse direction. The cells, more than two diameters thick, were considered as three dimensional systems.

Observation of 3D colloidal structures with a standard optical microscope is quite limited. As soon as the filling fraction is high enough that a layer of particles is formed at the bottom of a sample cell the light wavefront traveling from the focal plane to the microscope objective is disturbed which renders the imaging of the space above the layer difficult or impossible (if there are more than 2 layers). Therefore we were able to observe and accurately characterize the structures formed in cells with thickness less than 3 diameters of colloidal particles.

Typically the magnetic field, inducing desired interparticle interaction, was turned on and after relaxation time (a few seconds or minutes) when the system reached (quasi-)equilibrium the snapshots of the resulting mesophases were taken. When we were interested in the dynamics of structure formation, the videos at high frame rates (a few 100 fps) were recorded and then analyzed off-line.

Numerical calculation of the interaction energy

In order to understand the observed ordered mesophases of superparamagnetic particles in more details, a software for a numerical calculation of the system energy

in arbitrary external magnetic field was developed. If the effects of the local fields are taken into account, the energy of the system, in general, can not be expressed analytically (see Sec. 2.2.2) so numerical evaluation was unavoidable. The algorithm is described in Appendix A.

4.3 Static magnetic field in 2D system

The analysis of various ordered phases induced by different kinds of interparticle potentials starts with the simplest case: a static magnetic field in two dimensional system. According to the calculations in Sec. 2.2.2 the pair interaction can be either isotropically repulsive in the special case of the perpendicular field or anisotropic in any other case.

The behavior of the two dimensional system is governed by two external parameters - the strength of the magnetic interaction and the 2D filling fraction. One possible way of describing the interaction strength is with an interaction constant K defined as the magnetic energy of a pair of beads in the external field perpendicular to the pair. Using (2.16), the energy of such pair can be written as $E = \frac{\chi^2 V^2 B_0^2}{4\pi\mu_0 r^3} = K/r^3$ with

$$K = \frac{\pi\sigma^6\chi^2 B^2}{144\mu_0}. \quad (4.1)$$

Here σ is the bead diameter. It is also convenient to define similar dimensionless constant \tilde{K} (inverse "temperature" of the system) as a ratio between the energy of a pair of beads in contact divided by $k_B T$ [77]

$$\tilde{K} = \frac{K}{\sigma^3 k_B T}. \quad (4.2)$$

Typical magnetic fields in the experiments ranged from a few mT to a few tens of mT, giving \tilde{K} from a few tens to a few hundreds. At this point it has to be emphasized that our interest was not in the dynamical behavior of the system (crystal growth, melting, meshing...), but rather in the equilibrium or quasi-equilibrium structures formed by different types of interparticle potentials. As the typical \tilde{K} was high, the system reached (quasi)-equilibrium phase in matter of seconds after the interaction was turned on.

The surface filling fraction η is defined as a fraction of surface covered with beads

$$\eta = \pi\sigma^2 n/4, \quad (4.3)$$

with n being a numerical density of particles (number of particles/area). In a 2D system the maximum $\eta = \pi/2\sqrt{3} \approx 0.907$ is reached when the spheres are arranged in the hexagonal close-packed lattice.

4.3.1 Isotropic repulsion

If the magnetic field is directed perpendicular to the sample cell, the interaction between a pair of particles is isotropic dipolar repulsion (2.16). We performed two

different observations of the phase behavior of the system: at the constant filling fraction as a function of interaction strength and at the constant interaction across the broad density range. The characteristic micrographs of the former observation are presented in Fig. 4.2.

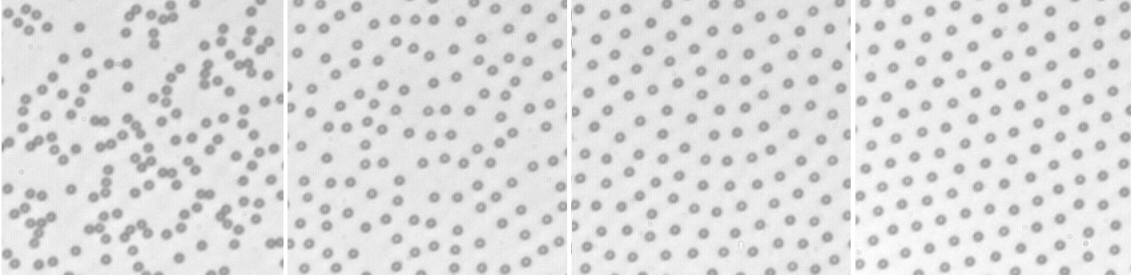


FIGURE 4.2: Micrographs of the typical phases in the 2D colloidal system with constant 2D filling fraction, induced by dipolar repulsion of different strengths. With no magnetic interaction, the system is hard-core liquid (left), which changes to open hexagonal lattice when the interaction is turned on. The inverse temperatures of the system from left to right micrograph are $\tilde{K} \approx 0, 10, 140, 2250$.

For low magnetic fields thermal motion dominates the magnetic energy and the colloidal particles are randomly distributed in the plane. The system shows continuous orientational and translational symmetry and appears as two dimensional fluid. As soon as the magnetic repulsion between the particles is large enough to dominate thermal motion some local order arises. At high interaction strengths, the particles arrange into hexagonal crystal which has discrete translational and six-fold orientational order.

Typical micrographs of the 2D system with constant interaction strength but increasing surface filling fraction are shown in Fig. 4.3. At low filling fractions, when the average pair interaction energies far below $k_B T$, the system is in the liquid phase. When the filling fraction is increasing the equilibrium structure changes to open hexagonal and then to hexagonal close-packed (HCP) lattice.

In the 2D system with the dipole-dipole repulsion the pair interaction energy can be written including filling fraction as $E = K/r^3 = \frac{K\eta^{3/2}}{(r\sqrt{\eta})^3} = \frac{K/a^3}{(r/a)^3}$, where the mean separation between the particles is $a = \sqrt{\frac{\pi\sigma^2}{2\eta\sqrt{3}}}$. If the distances are measured

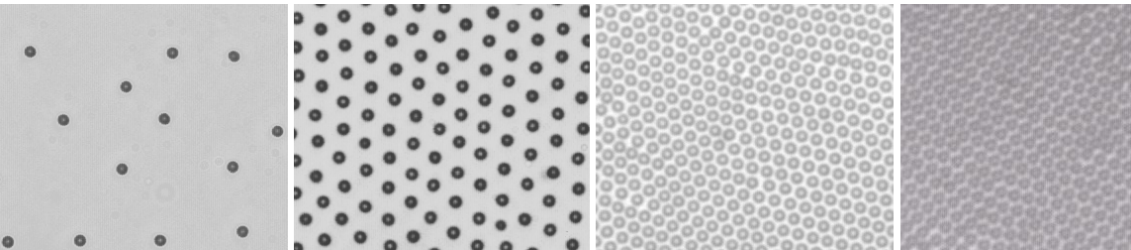


FIGURE 4.3: Micrographs of the typical phases in 2D colloidal system, induced by dipolar repulsion of constant strength ($\tilde{K} \approx 1000$). At low filling fractions (left) the particles are in liquid phase, which changes to open and close-packed hexagonal lattice when filling fraction is increased.

in units of the mean separation, the filling fraction merely rescales the temperature and only a single parameter is needed to explore the whole phase space [77, 78]. Differently, when the system is not two dimensional the filling fraction scaling is not present and two parameters are needed to describe it.

4.3.2 Anisotropic dipolar interaction

External static magnetic field in the particle plane gives rise to anisotropic interaction potential. The sign and the strength of the interaction depends on the relative position of the particles with respect to the field direction (2.15). In Fig. 4.4 we present the potential energy landscape of a single particle, induced by the magnetic field pointing in y -direction.

In order to calculate the energy landscape potential of a desired configuration a probe particle is introduced into the system and is moved across the plane of interest. The fixed particles are depicted with gray color (in this case, there is only one particle) whereas white color represents forbidden space for the centers of other particles due to the excluded volume. Different colors of other points in the image represent the total energy of the system if the probe particle is located in that particular point \mathbf{r} . The color scale in this and all other energy landscape images ranges from blue (lowest energy) through green and red towards black (highest energy).

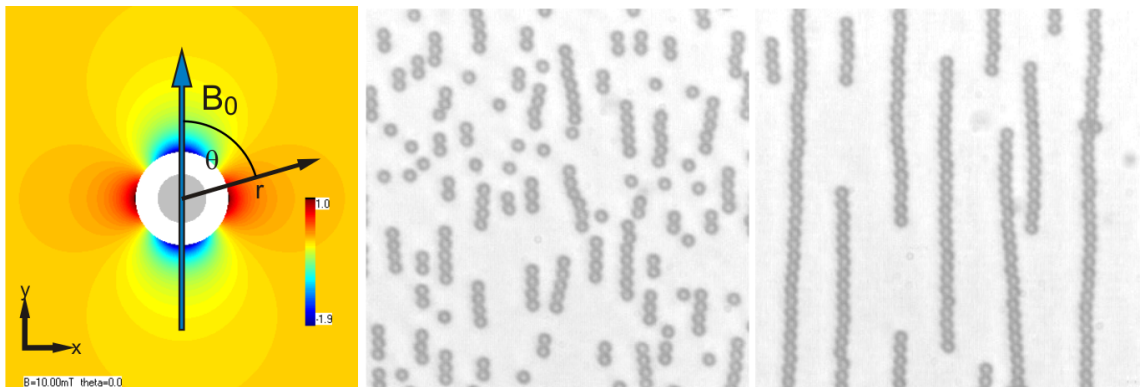


FIGURE 4.4: *Left:* The xy -plane energy landscape of a particle with external magnetic field \mathbf{B}_0 in the y -direction. The particle, indicated by gray color, is in the center of the image. White color around it represents the excluded volume (sphere with radius σ) for the probe particle. Different colors of other (x, y) points in the image represent reduced energy of the system $E/(K/\sigma^3)$ when the center of the probe particle \mathbf{r} is at (x, y) . The potential is symmetric with respect to the x -axis. Particles attract when $\theta < 54.7^\circ$ and repel when $54.7^\circ < \theta \leq 90^\circ$. *Right:* Two micrographs of the system with in-plane external magnetic field. When the field is turned on first small segments of chains are formed, which then merge into long single chains. At high filling fractions neighboring chains join into wider stripes (not shown).

The interparticle force is calculated as a gradient of the energy landscape. In this case, the particles are attracted together when the angle θ between vector \mathbf{r} to the location of the probe particle and the direction of the field is from $\theta = 0^\circ$ to 54.7° ,

and repelled away from each other when $\theta = 54.7^\circ$ to 90° . Between both regions, when $\cos^2 \theta = 1/3$, i.e. $\theta = 54.7^\circ$, the dipolar interaction between the particles vanishes.

If the external static magnetic field \mathbf{B}_0 lies out of the particle plane, it can be divided into two perpendicular components¹: the in-plane, which is either repulsive or attractive depending on the relative position of the particles, and the perpendicular component, which induces isotropic repulsion. The interparticle interaction is then a sum of both contributions.

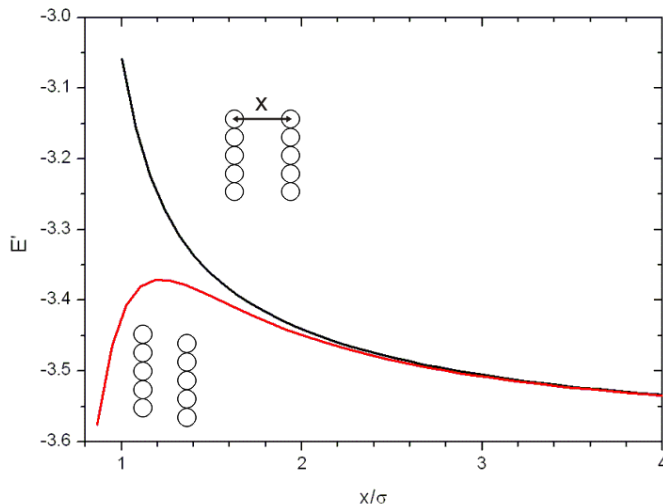


FIGURE 4.5: The reduced energy per particle for a system of two parallel chains in the field direction for different normalized separations x/σ . The black line represents the case when chains are not shifted in respect to each other (inline schematic) - the interchain interaction is always repulsive. The red line denotes the energy when one chain is shifted for $\sigma/2$ - the interchain interaction is repulsive at larger separations and attractive at short range. When a chain manages to cross the potential barrier (for example, if it is pushed by another chain), it gets locked to the other chain.

The stable structures in the case of the static in-plane magnetic field are chains of particles, oriented in the field direction. When the field is turned on at low filling fractions, single beads join into short chains (dimers, trimers...) which then merge into long single chains as shown in Fig. 4.4. The potential energy between two chains, parallel to field direction is presented in Fig. 4.5. It has a barrier: the interaction is repulsive at large separations and attractive if chains are close to each other and one chain is shifted in respect to the other for one radius of the bead.

The anisotropic nature of the dipole-dipole interaction and the resulting arrangement of particles have been investigated in different systems (colloids [79], dipolar fluids [80]...). In our work we studied various isotropic interaction potentials where the direction of the external magnetic field was not defining any preferred direction of the resulting structures. Although the interaction between the induced dipoles of the superparamagnetic beads is dipolar and therefore in general anisotropic, it

¹This holds for linear regime of magnetization, i.e. when then the induced magnetic moment of the particles is proportional to the external field, up to 10 mT for MyOne particles

is possible to achieve 2D and 3D isotropic potentials that stabilize richer set of structures than the simple $1/r^3$ dipolar repulsion.

We focused on two special configurations of the system that enable such interaction potentials. One was softened repulsive potential which was achieved by a combination of a static magnetic field and a confined sample geometry. The other, more complex potential, was obtained by rotating magnetic field. These potentials and their resulting mesophases are presented in the following sections.

4.4 Static magnetic field in quasi-2D system

The key feature of the system which softens the dipolar repulsion between the induced magnetic dipoles of particles is the cell thickness - if it is somewhat larger than the sphere diameter, the centers of two nearby spheres are not restricted to a plane perpendicular to the magnetic field. This makes their interaction at small separations less repulsive compared to spheres lying in the plane.

Resulting interaction potential can be written as

$$E(r, z) = K \frac{r^2 - 2z^2}{(r^2 + z^2)^{5/2}}, \quad (4.4)$$

with r and z being the horizontal and vertical components of the distance between the centers of the two particles (Fig. 4.1) and K the interaction constant (4.1). Typical magnetic fields in this experiment were around 10 mT, yielding $K \approx 250$, thus the induced pair forces were on the order of 0.1 pN at separations comparable to sphere diameter.

Geometrical constraint imposed by the particle diameter σ and the cell surface-to-surface separation h lead to the maximum vertical distance $\sigma - h$ between the centers of the particles and the minimum horizontal distance $r_c = \sqrt{h(2\sigma - h)}$ when the particles are at close contact. In the thin part of the wedge cell where $h \approx \sigma$ particles interact via the usual 2D dipolar repulsion $E = K/r^3$, while in the thicker parts of the cell ($h < 2\sigma$) the finite vertical distance z between the particle centers leads to the reduction of the repulsion or even attraction at small distances. The horizontal component of the force F_r between two beads is:

$$F_r(r, z) = -\partial E / \partial r = -\frac{3Kr}{(r^2 + z^2)^{7/2}} (4z^2 - r^2). \quad (4.5)$$

For the particles in contact ($z = h - \sigma, r = r_c$) this force is

$$F_r(r_c, h - \sigma) = -3Kr_c (5(h - \sigma)^2 - \sigma^2) / \sigma^7, \quad (4.6)$$

and becomes attractive at the critical thickness:

$$h_m = \sigma(1 + 1/\sqrt{5}) \approx 1.447\sigma, \quad (4.7)$$

The shape of the potential is the combination of a hard-core with range defined by the diameter of the colloidal beads and a soft-shoulder that originates in softened

dipolar repulsion (Fig. 4.6) in the parts of the cell where the thickness is large enough to significantly reduce the dipolar repulsion at small separations. At the same time the cell should not be thicker than h_m if the desired potential is to stay purely repulsive. With these two requirements met the potential is similar to that in numerical studies [22, 21, 23, 76] therefore a rich phase behavior for colloidal suspensions of varying densities was expected.

Experiment was performed in two steps. In the first step a dilute colloidal suspension was used to verify the interparticle potential shape on isolated colloidal pairs. In the second step a sample cell was filled with a dense colloidal suspension. A site within the cell was then identified where the interaction potential had desired properties. Afterwards a phase behavior of the system was recorded at different particle densities.

4.4.1 Measurement of interparticle potential

The interparticle potential was determined on an isolated pair of beads where one bead was attached to the lower surface of the sample cell. The second bead was used as a probe particle and was laterally confined by a weak optical trap. The light pressure of the trap pushed the probe particle against the upper wall of the cell so geometrically the situation corresponded to the one shown in Fig. 4.1. The probe particle was slowly periodically dragged back and forth on a $3 \mu\text{m}$ long linear path starting at $0.7 \mu\text{m}$ particle surface-to-surface separation. The measuring sequence was composed of a reference period during which the magnetic field was absent followed by a probe period with the magnetic field turned on. The trajectories of the probe were recorded for many repetitions of the measuring sequence and subsequently averaged. The average displacement of the probe particle from the trap center as a function of interparticle distance was then determined to obtain the dependence of the magnetic force on the interparticle distance. The stiffness of the laser trap confining the probe particle was determined by analyzing the Brownian motion of the probe particle during the reference periods. The procedure was repeated at a range of cell thicknesses and three representative force profiles are shown in Fig. 4.6.

If the sample cell is thicker than the diameter of the spheres ($h > \sigma$), the interaction is pure dipolar repulsion ($F \propto r^4$). At thicknesses close to the critical thickness ($h \approx h_m$), the in-plane interparticle force is always repulsive, but decreases to zero when particles get into the contact (at this cell thickness the in-plane hard-core diameter of the spheres is $0.89 \mu\text{m}$). At even higher thicknesses ($h \gg h_m$), the in-plane force is repulsive for large separations and attractive for small separations. This demonstrates that the system behaves as expected - by simple adjustment of geometrical constraints the interparticle potential can be varied from pure dipolar repulsion to softened repulsion or to a combination of attraction at small separations and weak repulsion at large separations (Fig. 4.6).

It is important to realize, that due to the limited but finite degree of freedom of the particles in the vertical direction the pair potential shown in Fig. 6.13 is not preserved in the case of many interacting particles. At low surface filling fractions ($\eta \leq 0.05$) when the average distance between the particles is large compared to

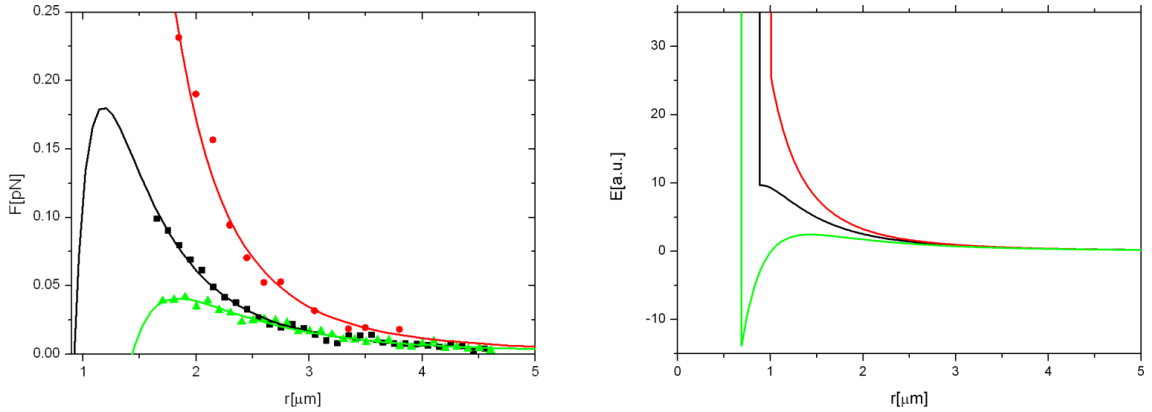


FIGURE 4.6: *Left:* Measured in-plane force profiles for 3 different cell thicknesses: r^{-4} repulsion in thin cell ($h \approx \sigma$; red circles), softened repulsion ($h \approx h_m$; black squares) and over-softened interaction in thick cell ($h > h_m$, green triangles) with the attractive part at small separations. Solid lines are fits of (4.5) for $h = \sigma$, $h = 1.46\sigma$, and $h = 1.72\sigma$, respectively. *Right:* Schematic drawing of the interaction potentials: dipolar repulsion ($h \approx \sigma$; red), softened repulsion ($h \approx h_m$; black) and over-softened interaction in thick cell ($h > h_m$, green).

the cell thickness, the interaction potential is well approximated by simple $1/r^3$ repulsion. At higher filling fractions ($\eta \geq 0.2$) it is energetically favorable for the particles to reside close to either the upper or the lower wall of the cell, i.e. the distribution of their heights is bimodal. In this situation particle pairs can be found in the following states: up/up, down/down and up/down state. In the first two states the particles "feel" a simple $1/r^3$ repulsion, while for the up/down state the interaction potential has a shape depicted in Fig. 4.6.

4.4.2 Phase behavior of a system with softened repulsion

Phase behavior of the system was studied across a broad density range. The cell was filled with a dense suspension of superparamagnetic spheres, and the measuring site with cell thickness of about h_m was located. As neither the cell thickness or the interaction potential couldn't be precisely measured due to the high density of the particles, the following protocol was used. In absence of the magnetic field, weak optical tweezers were used to herd the spheres at a given location into contact such that they formed cluster. Transverse magnetic field was then turned on which caused the cluster to disperse. In the thick part of the cell where the potential was attractive the cluster disintegration was partial, whereas in the thin part with purely repulsive interactions the cluster disintegrated completely. By scanning the cell the site with the desired thickness was identified.

In this region of the sample cell we increased the particle density η using the extended array of optical tweezers to locally heat the suspension. The heating induced a hydrodynamic flow which dragged a large number of particles (over 10^4) toward the trap, thereby increasing the local density almost to close packing. The tweezers were then turned off which stopped the flow, and the magnetic field was turned on.

The high density region underwent slow expansion such that the system could be observed at decreasingly smaller colloidal densities. A sizable change of the density took place on a time scale of about 10 s, which is much longer than the typical diffusion time² of particles (< 10 ms). The expansion was therefore slow enough to ensure quasi-equilibrium at all times, and the hydrodynamic interactions due to expansion $\approx 10^{-3}k_B T$ are negligible compared to the magnetic repulsion.

The main advantage of this protocol is that it allows one to study the states of a fixed ensemble of spheres at the same location in the cell (and thus at the same cell thickness) across a range of densities. This excludes any deviations in the sample that could affect its behavior in an uncontrolled way and ensures that the phase transitions are induced solely by density variation.

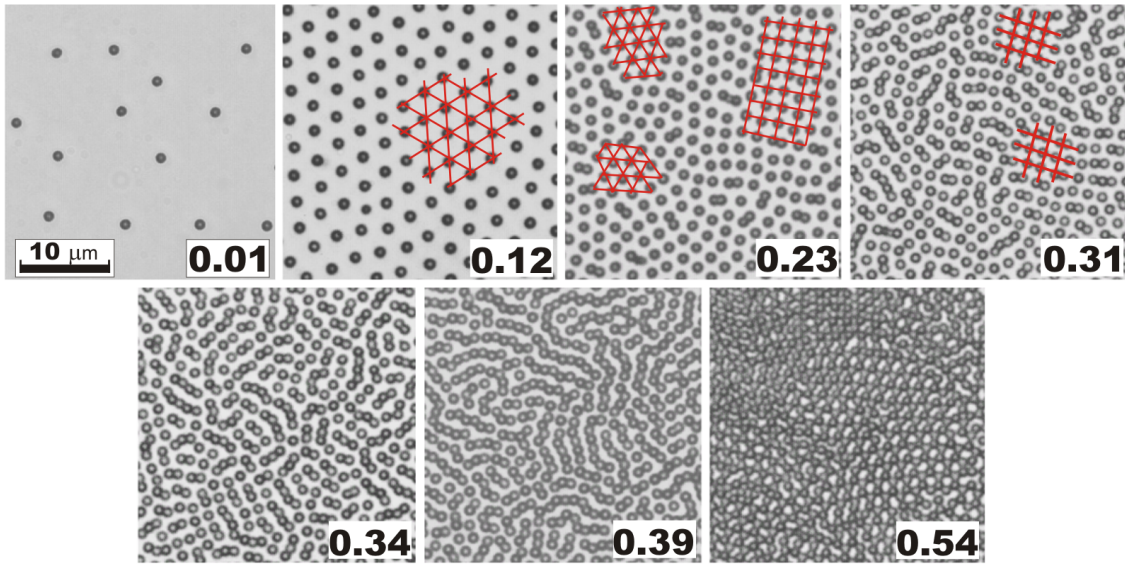


FIGURE 4.7: Micrographs of the representative mesophases induced by varying the surface filling fraction η (labeled). In some micrographs, patches of the underlying lattices are emphasized to guide the eye.

The micrographs of the most interesting phases observed at various surface filling fractions η are shown in Fig. 4.7. At very high filling fractions ($\eta \geq 0.5$) domains of honeycomb and dense square lattice were observed. At lower density ($\eta = 0.39$) dense lattice dispersed into stripe/labyrinthine structure formed predominantly by a single cluster of interlaced strings of touching spheres. Lower filling fraction ($\eta = 0.34$) resulted in a chain phase with locally aligned finite-length strings. At intermediate filling fractions ($\eta = 0.31$) there was a coexistence of expanded square lattice and chain phase, mainly composed of dimers and trimers. Coexisting expanded hexagonal and square lattice were observed at $\eta = 0.23$. When filling fraction was low enough, the system was in expanded hexagonal lattice ($\eta = 0.12$) and in liquid phase ($\eta = 0.01$).

² In equilibrium, a thermally excited particle in the potential well formed by its neighbors fluctuates around its mean position by about $d \approx (k_B T \sigma^5 f(\eta) 384K)^{1/2}$, where $f(\eta)$ is a numerical factor which equals 1 at close packing and ≈ 1000 at $\eta \approx 0.1$. The typical time needed to traverse this distance is $\tau \approx d^2/D$, where $D = k_B T / 3\pi\nu\sigma$ is the diffusion constant; ν is the viscosity. In our case, $\tau \approx 10 \mu\text{s}$ at $\eta = 0.5$ and $\tau \approx 10$ ms at $\eta = 0.1$.

The distribution of the heights of the particles can be analyzed to some extent. Close inspection of the micrographs reveals that some beads appear brighter than the others - it is because their position is slightly out of the focal plane of the image. At high filling fractions ($\eta = 0.1$ or more for $K \approx 250$, used in the experiment) the beads are either at $z = 0$ or $z = h$. The system therefore resembles an off-lattice two-state spin ensemble with dominant nearest-neighbor anti-ferromagnetic interaction. On the stripe, honeycomb and square lattice with 2, 3, and 4 regularly arranged nearest neighbors a simple ground state with alternating up-down positions of spheres exists, while on the hexagonal lattice the system is frustrated and no ground state with long range order is possible.

The experimentally observed mesophases are similar to those found in the numerical simulations. In [76] the structure and phase behavior of a 2D system with a hard-core and purely repulsive core-softened long-range interactions is studied using Monte Carlo simulations. The pair interactions are of the form, $E(r) = 4\epsilon[(\sigma/r)^{12} - (\sigma/r)^6] + \epsilon'(\sigma/r)^3$, with the energy parameter ϵ' chosen to give a stationary point of inflection in the pair potential. The simulation reveals a variety of interesting states: fluids with chainlike, striped, and 6 – 10 sided polygon structural motifs, low and high-density triangular crystalline phases and defective Kagome lattices. The states, found in simulation, are remarkably close to mesophases found in our experiment although the pair interaction is not the same. Even a much more idealized hard-core-soft-shoulder interaction also gives a similar phase sequence [21, 22]. This suggests that the mechanisms at work as well as the structures they produce are rather robust.

4.5 Static magnetic field in a 3D system

The previous Section describes the system of interacting superparamagnetic beads confined in the sample cell with the critical thickness $h_m \approx 1.447\sigma$, where the perpendicular external magnetic field induces softened repulsive radial interaction force between two particles. If the cell thickness is increased, the pair interaction force (4.5) remains repulsive at larger separations but becomes attractive at small separations as demonstrated in Fig. 4.6. In this Section we present the phase diagram of the system as a function of two parameters: filling fraction and the cell thickness.

4.5.1 Low filling fractions

When the filling fraction is low enough, stable structures are pairs of particles, which are aligned in the direction of the magnetic field \mathbf{B} if the thickness of the sample cell is more than two diameters ($h > 2\sigma$). Since the interaction between two such pairs is dipolar repulsion, pairs arrange into hexagonal grid as can be seen in Fig. 4.8(c). If the thickness of the cell is smaller but still above the critical thickness ($h_m < h < 2\sigma$), the pairs are tilted as in Fig. 4.8(a), (c). The polar angle θ between \mathbf{B} and the vector Σ connecting the centers of the particles depends on the ratio between the cell thickness and the diameter of beads, $\cos \theta = h/\sigma - 1$.

The azimuth angle ϕ between the x -axis of the system and the projection of Σ

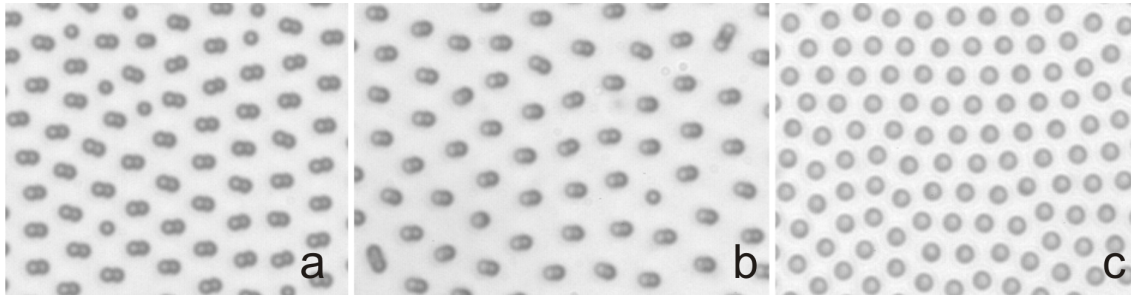


FIGURE 4.8: Representative micrographs of colloidal mesophases formed at low density at three different cell thicknesses. (a) Thickness is more than the critical thickness; pairs are stable despite the low filling fraction. (b) $h \approx 1.5\sigma$. (c) The cell is thick enough for pair formation in the field direction. The isotropic repulsion around each colloidal pair results in a hexagonal ordering of pairs. Note: beads in (c) look larger because two beads are stacked on each other.

to the xy -plane is random if there are no external forces that would make specific direction more energetically favorable. In the case of a dilute system this is true therefore time evolution of $\phi(t)$ is a random walk with diffusion constant determined by the friction of colloidal pairs. However, when the particle density is increased and pairs start to "feel" each other, the energy of a pair is not anymore degenerate in ϕ . In order to minimize the interaction energy with neighboring pairs, it is favorable for the pair to have the same ϕ as its neighbors. Such interaction gives rise to nematic structures, which can be seen in the micrographs (a) and (b) of Fig. 4.8.

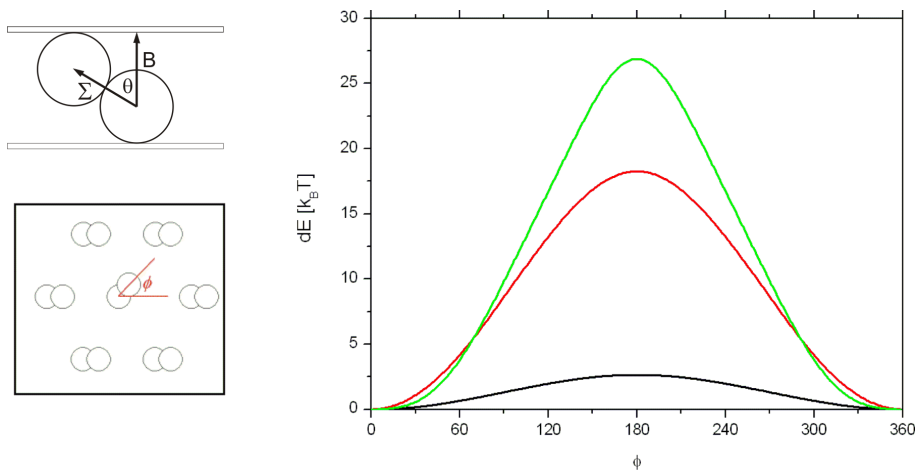


FIGURE 4.9: Nematic arrangement of colloidal pairs. *Top left*: Side view schematic of a tilted colloidal pair with polar angle θ . *Bottom left*: Top view schematic of a system of 7 tilted pairs in a hexagonal arrangement with lattice constant $a = 3\sigma$ used for numerical calculations. *Right*: Numerically calculated addition to the energy as a function of azimuth angle ϕ of the central pair for different pair polar angles $\theta = 50^\circ$ (green), 30° (red) and 10° (black) in the field $B_0 = 10$ mT.

It is evident that the interaction that tries to orient a colloidal pair in the direction of neighbors strongly depends on the pair polar angle. If the cell is thick enough to allow vertical pairs ($\theta = 0^\circ$), this interaction is zero, while on the other hand,

when the thickness is a bit more than critical thickness ($\theta_m = 63.45^\circ$), the interaction is the strongest. We have numerically calculated the addition to the magnetic energy of 7 tilted pairs in a hexagonal arrangement with the lattice constant $a = 3\sigma$ in the external magnetic field $B_0 = 10mT$ as a function of azimuth angle ϕ of the central pair. The results for different pair polar angles, presented in Fig. 4.9 support the observed formation of ordered pairs in Fig. 4.8.

4.5.2 High filling fractions

In a high filling fraction regime beads can't remain in isolated clusters, and chains of particles are formed. The chains consist of beads that are either in the contact with the upper or with the lower wall of the sample cell: if a starting bead is on the sample bottom ("down", d for short), then the second bead is pushed to the upper wall ("up", u). Third bead is then again d and so on till the last bead which is either u or d , depending on the number of particles in the chain. Schematic drawing of a tilted pair and a short chain is presented in Fig. 4.10.

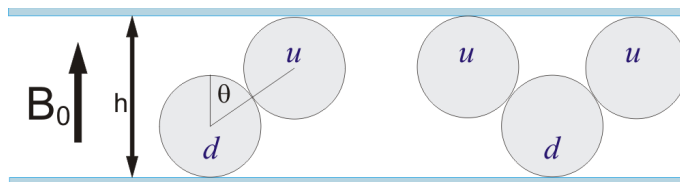


FIGURE 4.10: Schematic drawing of a tilted pair consisting of u and d particles and a short chain, made from u , d and u particles in a cell with $h_m < h < 2\sigma$. The angle θ is the pair tilt angle with respect to the direction of magnetic field \mathbf{B}_0

The creation of chains is a rapid process. When the magnetic field is turned on, particles join into dimers or trimers in a few tenths of a second, then these clusters merge into longer chains within couple of seconds. Three representative images of the system at high filling fractions are shown in Fig. 4.11. The leftmost is the micrograph of the region where thickness h is just slightly more than critical thickness h_m , the polar angle is approximately $\theta \approx 50^\circ$. The stable structures under these conditions are long single chains; their interchanging $u-d$ composition can be spotted by close inspection. The chains can form a network with junctions where three chains are connected together. The middle image shows a thicker part of the cell where the polar angle is $\theta \approx 35^\circ$ and the equilibrium structure are isolated single chains. Their $udud\dots$ configuration is even more pronounced and due to the optical artifacts they appear thicker. If the polar angle is even lower, chains disintegrate into colloidal pairs. In the right micrograph of Fig. 4.11 the cell is a bit thicker than two bead diameters. The isotropic repulsion around each colloidal pair results in a hexagonal ordering of pairs. In the lower right part of the micrograph two "defects" are emphasized, where three colloidal pairs are bound together by a single particle in the middle. Such formations enable increased filling fractions.

To understand the process of chain creation we have numerically calculated the energies of different configurations of basic building blocks as a function of their separation. In Fig. 4.12 we show a comparison of energy per particle as a function



FIGURE 4.11: Representative micrographs of colloidal mesophases formed at high density at three different cell thicknesses. *Left*: $\theta \approx 50^\circ$, stable structures are long single chains. Precise inspection reveals that every second bead in a chain is slightly out of focus. *Middle*: $\theta \approx 35^\circ$, stable mesophase is the same type of chains, but with less intersections. *Right*: $\theta \approx 0^\circ, h \geq 2\sigma$. The isotropic repulsion around each colloidal pair results in a hexagonal ordering of pairs. Red circle marks two "defects", where three colloidal pairs are bound together by a single bead.

of separation for two different configurations which consist of either two ud tilted pairs or ud tilted pair and a single u particle. The calculation was performed for two different cell thicknesses h giving the pair tilt angles $\theta = 30^\circ$ and $\theta = 50^\circ$.

As observed in the experiments, there is a repulsion between tilted pairs if θ is small. If θ is larger, there is still repulsion at large separations, but at small separations attraction prevails. Two pairs in the contact are bound in a potential well, whose depth depends on a pair tilt angle θ - higher θ induces deeper well. In the case of an ud pair and an isolated u particle there is also a potential barrier, but once the particle is over the barrier, it is strongly bound in udu configuration. This is the mechanism that stabilizes chains

In the experiment we never observed chain merging, which indicates interchain repulsion. In order to get the magnitude of this interaction, the energy of two parallel chains composed of up-down interchanging colloidal particles as a function of their separation was numerically calculated. Fig. 4.13 shows the energy per particle $E_{particle}$ of such system as a function of the normalized separation d/σ between the axes of two chains for two different lengths of chain and for two different polar angles θ . Regardless of the chain length and the polar angle the interchain interaction is always strongly repulsive. The calculated energies can be accurately fitted with power-law $E_{particle} = A_0 + A_1(d/\sigma)^\beta$, giving exponents β ranging from -1.37 (100 particles, $\theta = 30^\circ$) to -1.80 (10 particles, $\theta = 50^\circ$), which is interesting since the dipolar energy between two particles scales as $1/d^3$.

We have also performed the calculations of the energy of the same system, but with one chain shifted for a half of a basic unit ($\sigma \sin \theta$) in the long axis direction. One would expect that two chains in contact, one with configuration of beads $udud\dots$ and the other with shifted configuration $dudu\dots$, have lower energy than in the unshifted case, but it turns out that the energy difference is negligible. This interchain interaction is different from the interaction between two chains parallel to the field direction (Fig. 4.5), where a shift of one chain changes the interaction from repulsive to attractive.

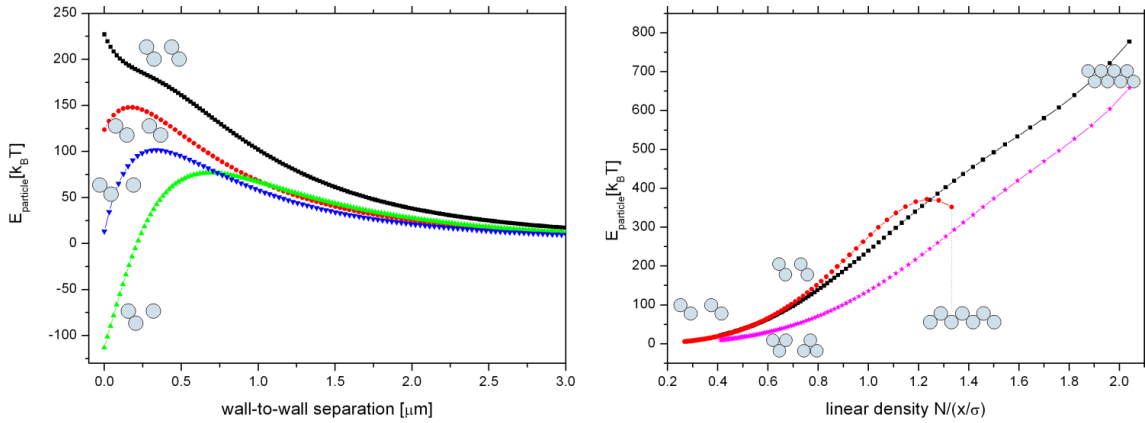


FIGURE 4.12: Calculated energy per particle for different configurations (side views as insets) at $B_0 = 10$ mT. *Left*: Energy as a function of surface-to-surface separation x . When a tilted pair of beads in ud configuration is approached by a single u particle, there is a potential barrier of $70k_B T$ for polar angle $\theta = 30^\circ$ (green triangles) or $90k_B T$ for $\theta = 50^\circ$ (inverted blue triangles). If a tilted pair approaches to another tilted pair the potential shape on depends on θ . Low θ induces repulsive potential (example $\theta = 30^\circ$, black squares), while at high θ there is a potential barrier (example $\theta = 50^\circ$, red circles). *Right*: Energy as a function of linear density of particles, i.e. the number of particles per particle diameter. Black squares and red circles indicate energy for tilted pairs at polar angles 30° and 50° , respectively. Magenta stars indicate energy of perfect triplets at $\theta = 30^\circ$.

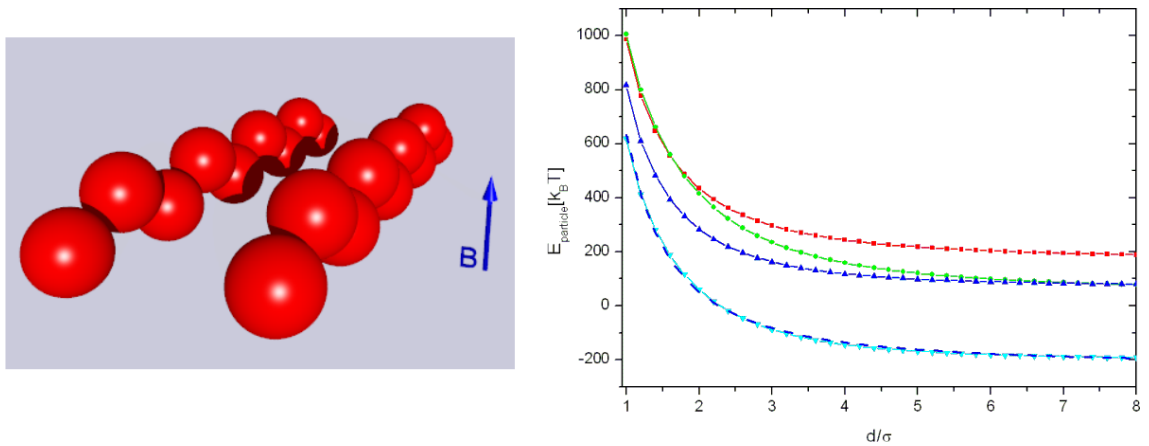


FIGURE 4.13: Numerically calculated energy per particle for a system of two parallel chains (left image) as a function of their normalized separation D/σ . The upper two curves show the energy for chains of 100 beads for two tilt angles, $\theta = 30^\circ$ (red squares) and $\theta = 50^\circ$ (green circles). The lower two curves show energy for short chains, made of 10 beads, also for $\theta = 30^\circ$ (blue triangles) and $\theta = 50^\circ$ (light blue inverted triangles). The fit of power-law function to the data of the lowest curve (dashed) yields $\beta = -1.65$.

The results of numerical calculations are in agreement with the experimentally observed mesophases. The calculations explain the formation and behavior of colloidal pairs at low and colloidal chains at high filling fractions.

4.6 Rotating magnetic field in 2D system

The rotation of the external magnetic field enables new type of interaction potentials. As explained in Sec. 2.2.2 the rotating field induces attractive effective interaction between dipolar particles and exerts a torque on the particle aggregates. The phenomenon has been studied (in systems of magnetic holes [81], droplets [82], magnetorheological fluids [83]...) and used for self-assembly and rotation of colloidal micropumps [84, 85]. Common feature to the mentioned experiments is the rotation of the field in one direction only which caused the structures to rotate. The stationary rotation frequency is reached when the magnetic torque is balanced by the viscous torque. In contrast, our magnetic tweezers enable bidirectional rotation of the field, therefore the self-assembled structures do not rotate and the viscous forces do not affect their shapes.

4.6.1 Inplane rotation of field

If the magnetic field rotates in the particle plane the average dipolar pair interaction is isotropic attraction as calculated in (2.17). Superparamagnetic particles exposed to such magnetic field merge into clusters of close packed hexagonal arrangement. If the field direction is changed, it is energetically favorable for clusters to follow the field. In case of a rotating magnetic field also the clusters rotate. If the frequency of field rotation is low enough (friction torque of the cluster is smaller than the magnetic torque), the clusters can follow the field direction consequently their frequency of rotation is the same as the field frequency. If the field rotation frequency is higher, then in each turn of the field the colloidal cluster rotates just for a part of the full turn (phase-slip regime). The cluster rotation frequency is therefore smaller than the field rotation frequency. In order to prevent the rotation of the colloidal clusters,

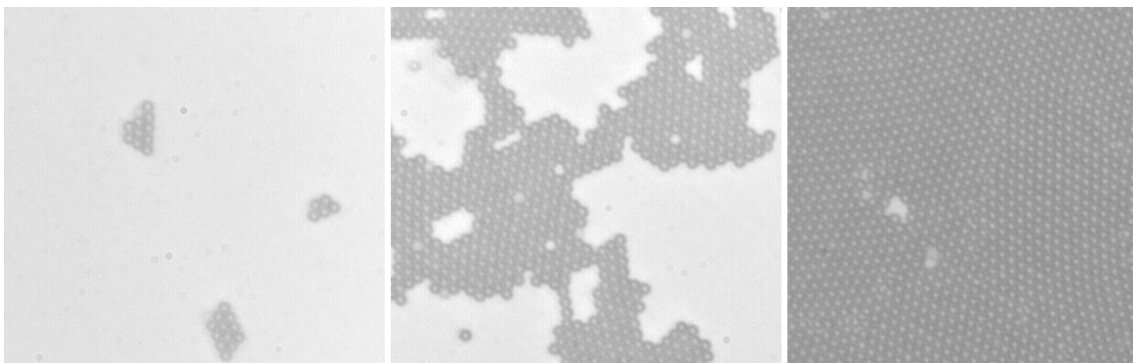


FIGURE 4.14: Micrographs of 2D system with isotropic attraction at three different filling fractions. The resulting structure is always hexagonal close packed lattice with possible defects.

the in-plane field was rotated back and forth for 360° . If the effective frequency of field rotation is too small then the clusters "shiver" back and forth, thus as high as possible frequency is preferred. In the experiment the frequency was 400 Hz which was high enough to efficiently suppress the effects of field rotation for fields of a few mT used in experiment.

Typical resulting structures of in-plane rotation of the magnetic field for different initial filling fractions of colloidal particles are shown in Fig. 4.14. The images were taken 3 minutes after the field of 4 mT was turned on. As expected, the basic arrangement of beads is a HCP lattice. The 2D crystals, especially in the systems with intermediate filling fractions, have lots of voids (defects) which indicates that they are far from equilibrium. Even if the field is turned on for a long period of time, particles do not arrange into one perfect defect-free HCP cluster due to kinetically arrested particles, i.e. the particles with the too high energy barrier towards more favorable configurations.

4.6.2 Rotation of tilted magnetic field

We have already shown that the magnetic field perpendicular to the plane of the particles induces dipolar repulsion and that the rotating in-plane field induces dipolar attraction. Now let us consider a combination of both fields. The combined field $\mathbf{B}_0 = B_0(\sin \theta_p \cos \phi, \sin \theta_p \sin \phi, \cos \theta_p)$ precesses on a cone (Fig.4.15) whose opening angle θ_p depends on the relative magnitude of rotating in-plane $B_{xy} = \sqrt{B_x^2 + B_y^2}$ and vertical B_z components

$$\tan \theta_p = \frac{\sqrt{B_x^2 + B_y^2}}{B_z}. \quad (4.8)$$

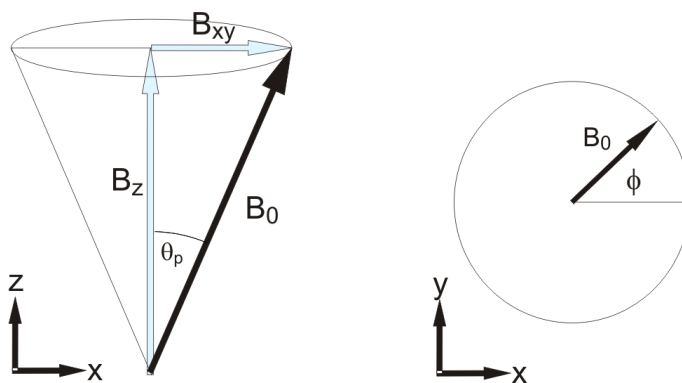


FIGURE 4.15: The combined external magnetic field $\mathbf{B}_0 = \mathbf{B}_z + \mathbf{B}_{xy}$ field precesses on a cone with opening angle θ_p as can be seen in a side-view (left). Top-view (right) reveals the azimuthal angle ϕ between the in-plane field component and x -axis.

If two particles are in such precessing field, it is natural to expect that the effective interaction in linear magnetization regime is a sum of dipolar repulsion and dipolar attraction. Micrographs of the typical mesophases that grow in a low filling fraction system under different opening angles θ are shown in Fig. 4.16. If the opening angle of the cone θ_p is small, the repulsion prevails and the colloidal

beads arrange in a hexagonal lattice. On the other hand, very large opening angles close to 90° make the beads attract each other, so the resulting arrangement is HCP. Interesting effects arise in the intermediate region of the opening angles, where magnitudes of the repulsive and the attractive interactions are of similar magnitude. Similar experiment have been recently performed [86], but their use of the rotating magnetic field resulted in symmetrical rotating clusters, formed by the combined effects of magnetic and viscous forces.

When the opening angle θ_p is increasing, the repulsive force is decreasing which consequently dissolves the initial hexagonal lattice as can be seen in Fig. 4.16 where $\theta_p = 46^\circ$. The interparticle repulsion is still strong enough to prevent beads to come into contact. Surprising effect happens at $\theta_p = 50^\circ$ - colloidal particles join into chains, which suggests the presence of an attractive force. Theoretically calculated repulsion induced by the vertical component of the field (2.16) is at this θ_p larger than the attraction induced by the rotating component of the magnetic field (2.21), therefore particle aggregation is not expected. Experimentally observed stable single chains indicate that the attractive force acts only at chain ends, whereas in the direction perpendicular to the chain there is a repulsion, otherwise 2D crystallites would be formed. The regions around chains are clear of any beads due to this repulsion.

Just a slight increase of the cone opening angle to $\theta_p = 52^\circ$ changes the behavior of the system - colloidal chains interconnect into a network. In each junction exactly three chains are joined together, preferably at an angle of 120° . The angle and empty space between neighboring parallel chains imply the interchain repulsion perpendicular to chain direction.

At around $\theta_p = 58^\circ$ the in-plane component of the magnetic field induces the attractive force that is stronger than other interparticle forces. The remaining single beads are adsorbed to the chains; since there is no repulsion between chains anymore, they start to merge. This is a gradual process, because the attractive force in the chain direction (which also prevents chain bending), is stronger than the attraction between two neighboring chains. Since chains are cross-linked, they can't instantaneously rearrange into energetically more favorable configuration of a HCP lattice. In fact, although there is an attraction among all components of the system, it never reaches the equilibrium configuration because the potential barriers towards energetically more favorable configuration are too high.

The colloidal mesophases in a 2D system with higher filling fraction, induced by the precessing magnetic field, are shown in Fig. 4.17. At $\theta_p = 35^\circ$ the dipolar repulsive force is still strong enough to stabilize expanded hexagonal lattice, whereas at $\theta_p = 39^\circ$ the onset of chains can be seen. Chains are clearly visible at $\theta_p = 42^\circ$, although the majority of beads is still free. Higher opening angle, $\theta_p = 46^\circ$, induces cross-linking of the chains. Due to the high filling fraction, the density of chain junctions is higher and average length of chain segments is shorter compared to the system with the lower filling fraction.

Almost all particles become part of the network at $\theta_p = 50^\circ$. There are only rare occasions of single beads, pushed to the middle of network pockets as a result of repulsive force perpendicular to the chain direction. At $\theta_p = 56^\circ$ the dipolar attraction prevails, the remaining single particles are drawn into the network and

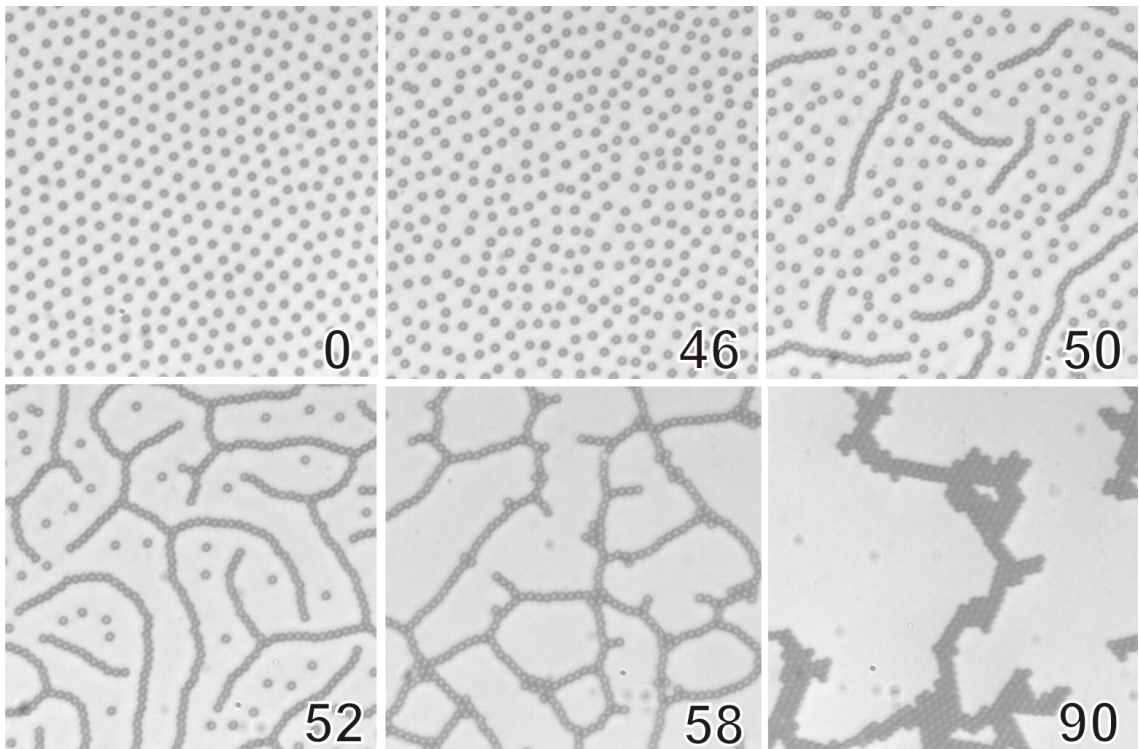


FIGURE 4.16: Experimental snapshots of a low filling fraction 2D system with magnetic field precessing on a cone, labeled by the corresponding opening angle of the cone θ_p .

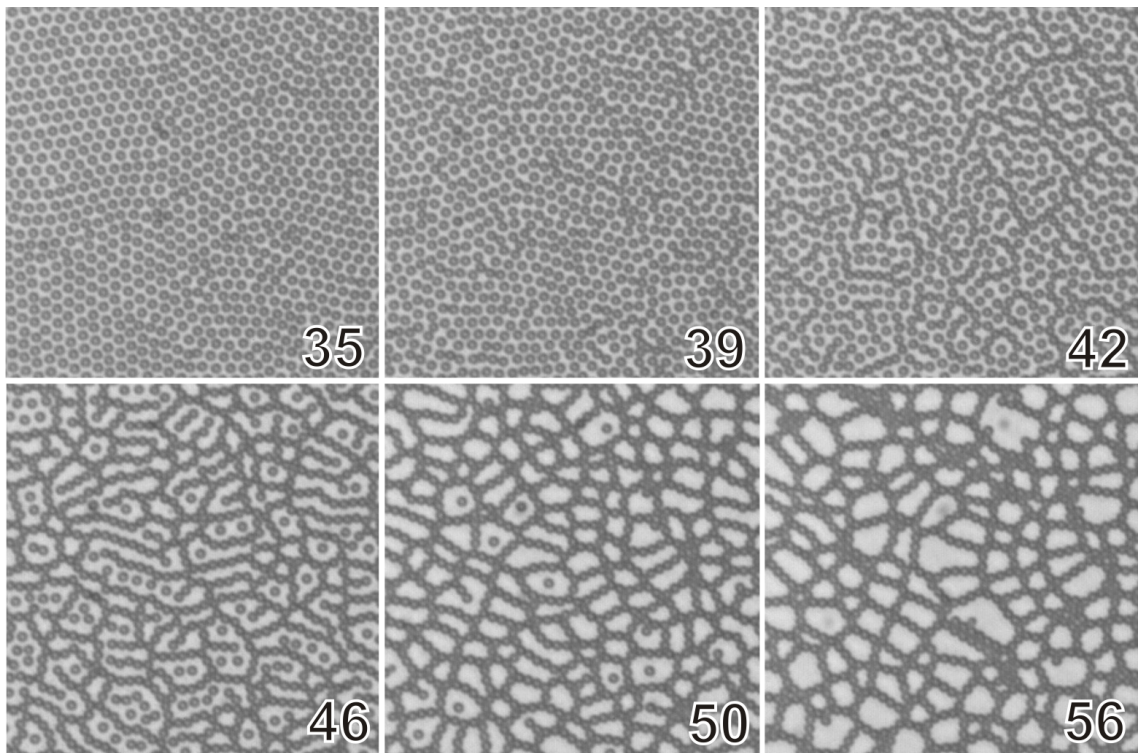


FIGURE 4.17: Experimental snapshots of a high filling fraction 2D system with precessing magnetic fields, labeled by the corresponding opening angle θ_p .

the process of the network coarsening begins. Some chains in the micrograph have already torn up and merged with neighboring chains to form 2D crystallites which have lower energy.

Qualitatively the same mesophases are found in both systems, either with low or high filling fraction. At small cone opening angle θ_p the stable phase is the expanded hexagonal lattice, which dissolves as θ_p increases. At some θ_p the particles start joining into chains, which attract other particles at ends but repel them sideways. When θ_p is high enough, isolated chains interconnect into a network of single chains. Even higher opening angle makes the dipolar attraction the dominant force so the structure collapses into a HCP crystal.

There is a quantitative difference between both systems: if micrographs of both systems at $\theta_p = 46^\circ$ are compared, one can see that in the dilute system, the particles are still well separated, whereas in the dense system, not only the chains have already been formed but they are already interconnected. Higher filling fraction results in smaller average interparticle separation, which means that even the subtle changes of interaction (created by tiny variation of θ_p) can induce different equilibrium structure. To explain the observed formation of new structures, we have

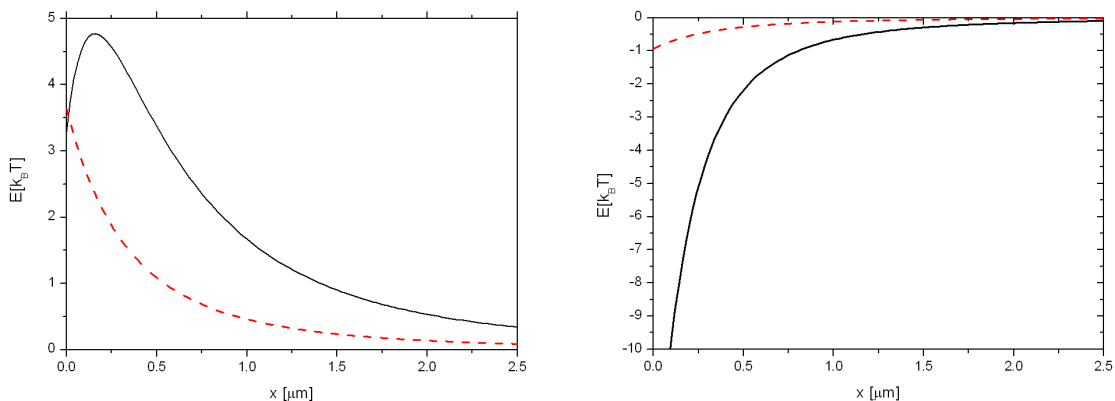


FIGURE 4.18: The energy of a pair of particles as a function of surface-to-surface separation x at $\theta_p = 50^\circ$ (left chart) and $\theta_p = 56^\circ$ (right chart). Comparison of exact energy calculation (black) with dipole-dipole potential where the effect of the local field is neglected (dashed red).

numerically calculated the energies of a few basic configurations. When the magnetic field with θ_p that prefers the creation of chains is turned on, isolated beads first merge into shorter chains (typically pairs), which then join into longer chains; consequently we have first analyzed the formation of particle pairs. In Fig. 4.18 we compare the energy E of two particles as a function of their surface-to-surface separation x when the opening angle of field cone is $\theta_p = 50^\circ$. At this angle the dipolar interaction between two dipoles of fixed magnitude that follow the direction of the rotating field is repulsive. The exact calculation of energy where the effects of local fields are taken into account reveal an important difference - at large separations the behavior of $E(x)$ is the same, whereas at small separations there is a potential barrier. When a particle is pushed over a potential barrier by thermal fluctuation or by another particle, a stable pair is formed.

The attraction (and the resulting formation of pairs) at low θ_p , where $1/r^3$ dipolar interaction should be repulsive, is a clear confirmation of the local field effect, explained in Fig. 4.19. The local magnetic field created by the induced dipole of the first particle *reduces* the induced dipole of the second particle ("demagnetization") when the direction of the external field is perpendicular to the pair - the pair interaction is less repulsive. When the external field is in the direction of the pair, the local magnetic field created by the first particle *increases* the induced dipole of the second particle ("magnetization") and makes the pair interaction more attractive. Averaging over one cycle of the magnetic field precession brings an overall attraction that causes the potential well at small interparticle separations.

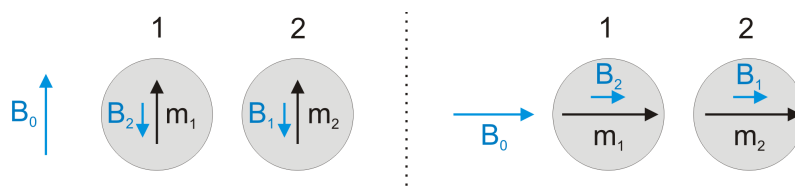


FIGURE 4.19: Schematics of the local field effect. B_1 and B_2 are the local magnetic fields of particle 1 and 2, respectively. *Left*: When the external magnetic field B_0 is perpendicular to the pair, the induced dipoles m_1 and m_2 are smaller ("demagnetization"). *Right*: When the external magnetic field B_0 is in the pair direction, the induced dipoles m_1 and m_2 are larger ("magnetization").

4.6.3 Measurement of interparticle potential

The interparticle potential was measured using optical tweezers. We first found a bead that was attached to the surface of the sample cell and another free bead that was used as a force probe. The rest of the measuring procedure was exactly the same as described in Sec. 4.4.1. Two representative force profiles are shown in Fig. 4.20.

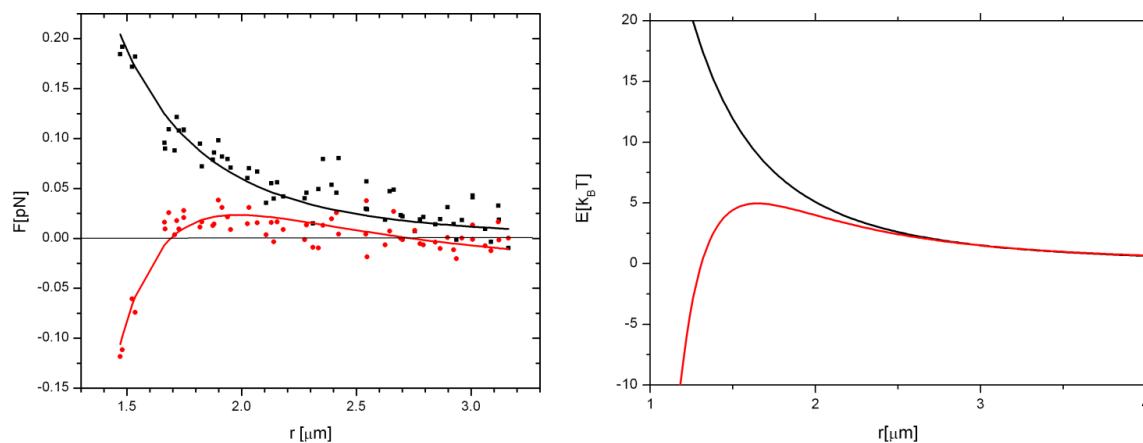


FIGURE 4.20: *Left*: Measured interparticle force profile for two cone opening angles: $\theta = 0$, $B_0=2$ mT (black squares) and $\theta = 53^\circ$, $B_0=10$ mT (red circles). *Right*: Corresponding calculated pair potentials.

Although the measured data points are highly scattered two distinct profile shapes can be clearly seen. Vertical magnetic field ($\theta = 0$, $B_0 = 2$ mT) induces

$1/r^4$ repulsive force between two particles. The force induced by the precessing magnetic field with cone opening angle $\theta = 53^\circ$ ($B_0 = 10$ mT) is attractive at small separations due to the effect of the local fields. We have to stress that the magnitude of the magnetic field, used in the measurement at $\theta = 53^\circ$ had to be 5 times larger to obtain comparable forces at separations of interest because the dipolar repulsion and attraction almost cancel each other at this θ . The force profile measurement demonstrates that the system behaves as expected - by the adjustment of the field cone opening angle θ the shape of the interparticle potential can be varied from pure dipolar repulsion at $\theta = 0$ through more complexly shaped at intermediate θ to pure dipolar attraction at $\theta = 90^\circ$.

4.6.4 Many-body effect

After a pair of beads is formed, the potential around it is not isotropic anymore. Fig. 4.21, where we present the energy landscape of a pair of particles in contact, is a key to understanding the observed formation of chains. Anisotropic nature of the interaction between the pair and a probe particle can be clearly observed on the xy energy landscape. If the probe particle is approached to the pair in the direction of its long axis (x -direction), the total energy of the system is a few $k_B T$ lower than the energy when the probe is far away. On the other hand, if the probe approaches the pair from the direction of short axis (y -direction), the total energy is a few $k_B T$ higher.

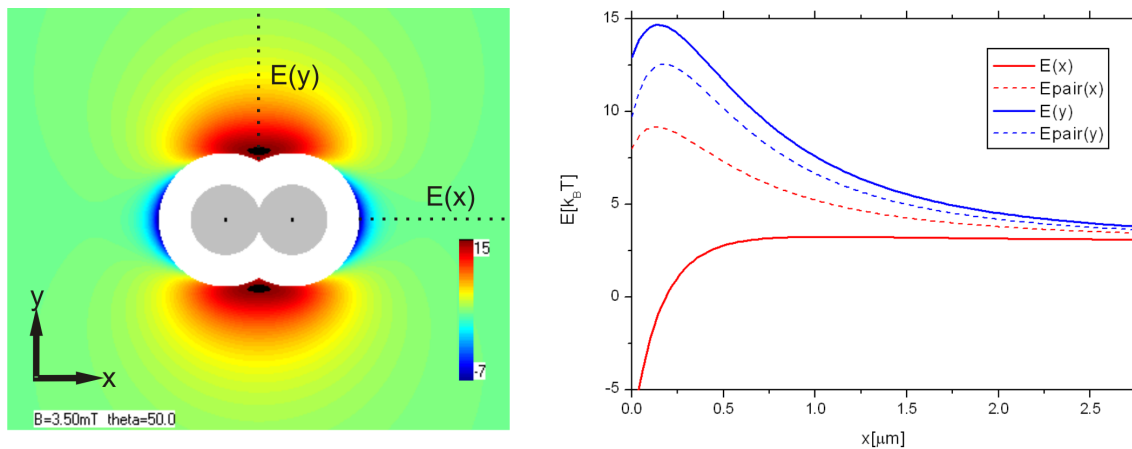


FIGURE 4.21: Calculated energy for 3 particles in xy -plane. *Left*: The energy landscape around a pair of particles at $\theta_p = 50^\circ$ and $B_0 = 3.5$ mT. *Right*: System energy vs. surface-to-surface separation when the probe particle is approaching the pair in two special directions (dashed in the left image): in the direction of the long axis of the pair ($E(x)$, blue) and in the direction of the short axis ($E(y)$, red). Dashed curves represent energies for the same two cases but calculated as a sum of 3 pair energies.

The anisotropy of the energy landscape around a pair is altered by the effect of many-body interactions. The interaction between a pair of particles at $\theta_p = 50^\circ$, shown in Fig. 4.18, is repulsive at surface-to-surface separations larger than $0.25 \mu\text{m}$ and attractive at smaller separations. If the energy of the system of 3 interacting particles was just a sum of three individual pair energies, it would be impossible to

obtain the attraction in the direction of a pair. The energy profiles, calculated as a sum of pair energies, are presented in Fig. 4.21 with dashed lines. If another particle is approaching from the direction of short axis, the energy profile $E(y)$, obtained as a sum of 3 pair energies, is similar to the exact many-body energy calculation. This certainly isn't valid if the third particle is coming from the direction of the pair ($E(x)$). The exact many body calculation reveals attractive potential whereas sum of pair energies results in a repulsive potential.

To explain the formation of single chains, the force on a single particle approaching to a pair has to be considered. If the particle is somewhere near the long axis of the pair it is immediately drawn to the pair and a linear structure is formed. On the other hand, if the particle is in the region near the short axis, it is either repelled away or pulled to the either end of the pair, so the resulting structure is again linear.

4.6.5 Assembly of colloidal superstructures

When the magnetic field with $\theta_p \approx 50^\circ$ is turned on in the low filling fraction system the resulting self-assembled structures are single chains of beads (Fig. 4.16), oriented isotropically in all directions. Chain growth is similar to the polymerization, a process where monomer molecules form polymer chains. The growth of colloidal chains decreases both the energy of the system and the filling fraction of beads (monomers). The growing stops when there are no free beads in the vicinity of chain ends.

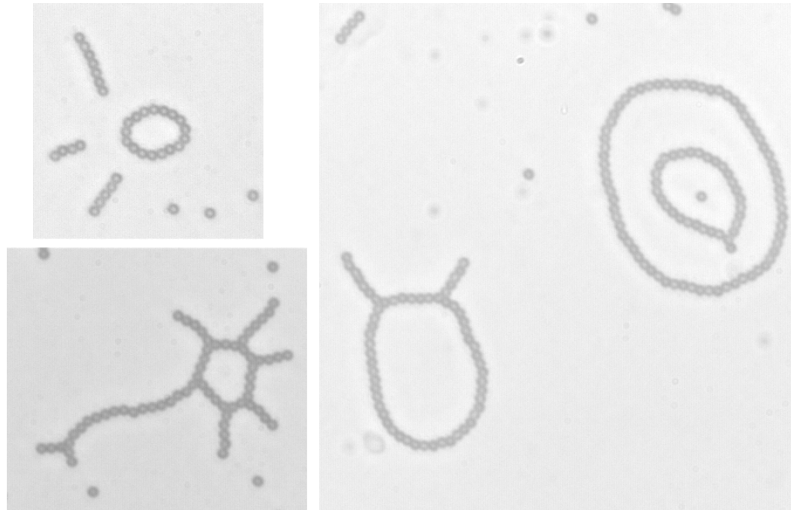


FIGURE 4.22: Colloidal superstructures assembled using optical tweezers. The attraction between two beads in the direction of chains stabilize 2D structures. The repulsion perpendicular to chains prevents them to collapse into a 2D HCP crystal. ($\theta_p = 53^\circ$, $B_0 = 3.5mT$)

Chains are stable structures at external magnetic field of a few mT . Beads at chain ends are in the potential well of more than $5k_B T$ and are therefore "permanently" bound to the rest of the chain. This enables the formation of more complex structures composed from colloidal chains. We used optical tweezers to manipulate them into desired structures; some of them can be seen in Fig. 4.22. Either be single

beads, chains, rings, decorated rings, structures within structures, they are freely fluctuating and undergoing Brownian motion.

The simplest structure formed from a chain is a ring, which is obtained when a chain is bent and its ends joined together. The bending costs energy due to the repulsion perpendicular to the chain direction. The bending energy depends on ring diameter: smaller rings have greater bending energy and therefore higher tension. In Fig. 4.23 we present micrographs of the artificially assembled colloidal rings of different sizes. The smallest ring of the left image has ruptured and opened into a straight chain, seen in the right image.

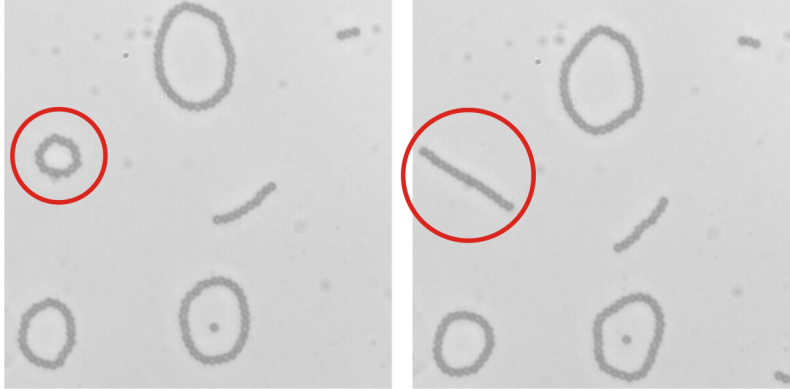


FIGURE 4.23: Colloidal rings repel each other. The rings are in general stable, except rings with small diameters which are less stable due to high bending energy. The smallest ring in the left micrograph has ruptured and transformed into a chain. ($\theta_p = 53^\circ$, $B_0 = 3.5mT$)

The repulsion perpendicular to the chain direction gives rise to an interesting phenomena - repulsion between the structures made of colloidal chains. If two rings are brought together using optical tweezers a weak repulsion can be observed - rings slowly drift away from each other. In an enclosed sample with a high number of rings a crystallization would occur - the rings would arrange into an ordered lattice. If a ring is created within another ring (as in Fig. 4.22), the two rings never touch despite their undulations around equilibrium circular shape.

4.7 Residual interaction induced at magic angle rotation

When the opening angle of the field cone equals the magic angle $\theta_m = \arccos(1/\sqrt{3}) \approx 54.7^\circ$ the $1/r^3$ term of dipolar interaction vanishes. The effective interaction between two particles averaged over one cycle of magnetic field rotation is analytically calculated in Appendix A. At magic opening angle $\theta_p = \theta_m$, the lowest non-zero correction to the energy of a pair of induced dipoles in the external magnetic fields reads

$$\bar{E} = -\frac{\chi^3 V^3 B_0^2}{16\pi^2 \mu_0} \frac{1}{r^6}. \quad (4.9)$$

Due to fully 3D isotropic nature of the interaction (6.16) which is completely independent of the direction of the major axis of the cone of the external magnetic

field, colloidal systems in this section are not divided anymore into 2D, quasi-2D and 3D systems. Instead, the focus is on the interactions and structures induced by the magic angle field rotation in a 3D system.

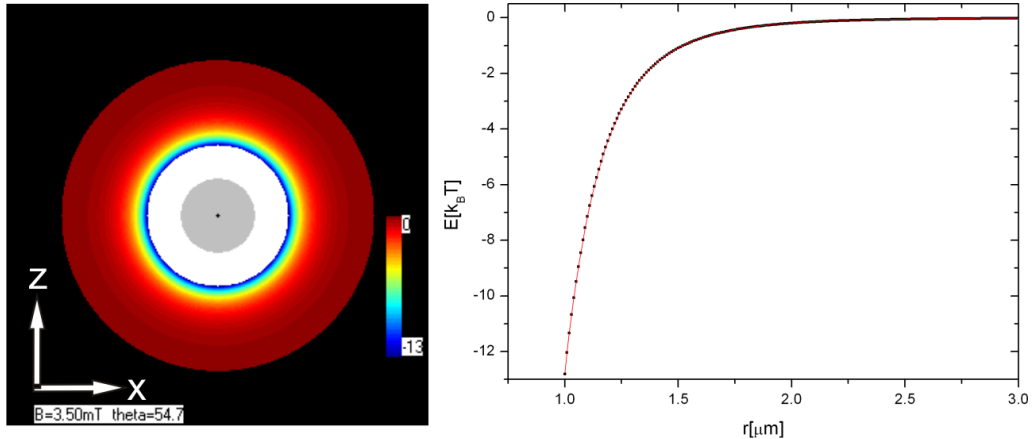


FIGURE 4.24: *Left:* Calculated energy landscape around a single particle at magic angle and $B_0 = 3.5$ mT. The potential is spherically symmetric, shown is the xz -plane. *Right:* Calculated pair energy as a function of the interparticle separation. Red curve is fit of the calculated data with the power-law function with the exponent $\beta = 6.087$.

In Fig. 4.24 we present numerically calculated energy of a pair of particles when $\theta_p = \theta_m$. Although the axis of the cone of the field precession is in the z -direction, the energy potential around a single particle is isotropic. The chart in Fig. 4.24 shows the energy of two beads as a function of their center-to-center separation. The calculated data can be fit with power-law dependence³, $E(r) = Ar^{-\beta}$, yielding $\beta = 6.087 \pm 0.002$, which confirms the analytical calculation of the effective interaction (6.16).

Due to the isotropic $1/r^6$ energy potential around a bead another bead from the vicinity is attracted and a colloidal pair is formed. Its initial orientation is determined by the positions of the constitutive beads, but later the orientation is random, governed only by thermal fluctuations. In Fig. 4.25 micrographs of self-assembled structures formed in a dilute colloidal system are presented. The colloidal pairs are pointing in all directions, both in xy and xz plane, which is a clear evidence of the isotropic nature of the pair interaction.

The energy landscape around a pair of beads, presented in Fig. 4.26, is not isotropic. A third bead is attracted to the pair if approached from the direction of the long axis - the resulting linear configuration of 3 beads has approximately $30k_B T$ lower energy compared to the case when the third bead is far away from the pair. If the third bead approaches from the side, it reaches a tiny potential barrier (less than $k_B T$). The particle is then drawn to either end of the pair and the resulting structure of 3 particles is linear.

If the approaching particle manages to overcome the potential barrier, a triangular configuration of particles is formed. This configuration is stable (it has around

³The slight deviation from $\beta = 6.00$ is due to the higher order terms that are neglected in the analytical calculation.

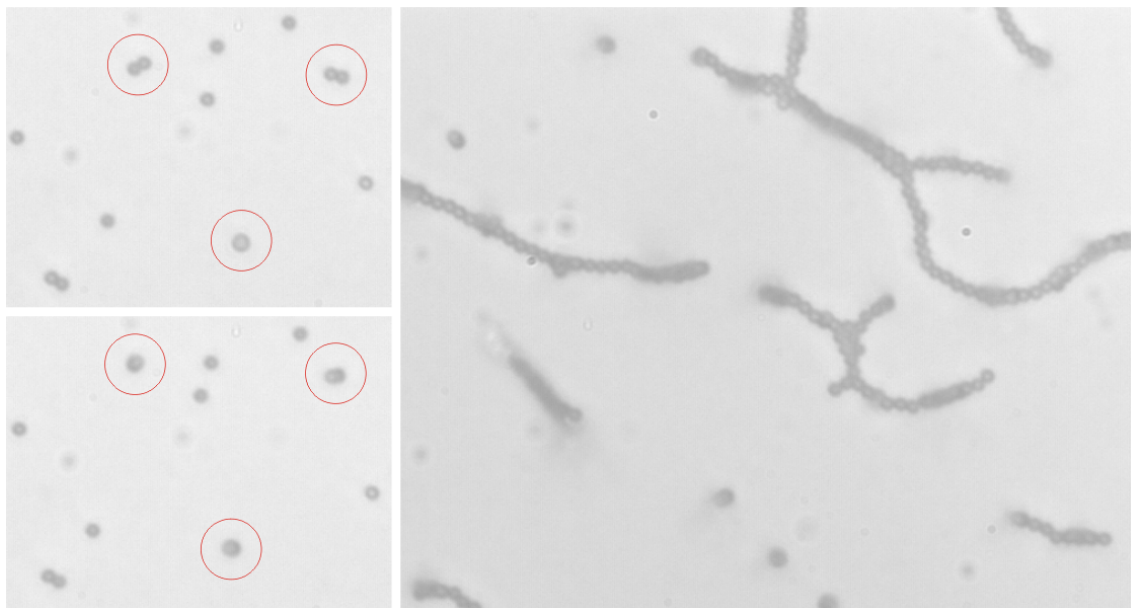


FIGURE 4.25: Micrographs of the self-assembled colloidal chains formed by magic angle rotating magnetic field $B_0 = 3.5$ mT. *Left*: Two consecutive snapshots of the low-filling fraction system, the lower one taken 1 s after the upper one. Colloidal pairs (circled) are stable regardless of their orientation. *Right*: Larger structures, predominantly single chains, which are at some locations joined by additional beads and form double chains.

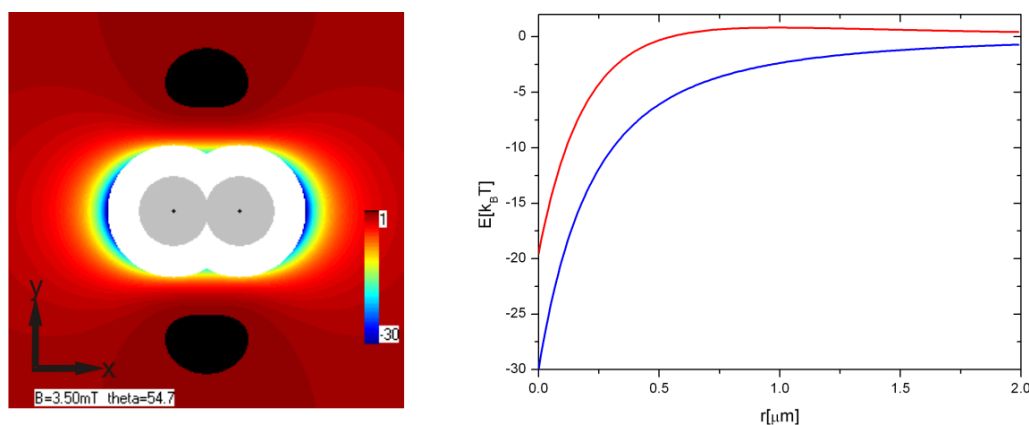


FIGURE 4.26: Calculated energy for 3 particles at magic angle and $B_0 = 3.5$ mT. *Left*: The energy landscape around a pair. *Right*: Calculated total energy as a function of surface-to-surface separation between the pair and a third particle. The force is always attractive if the third particle is on long axis (x -direction) of the pair (blue). If it is on short axis (y -direction), the force is attractive at small and slightly repulsive at larger separations (red).

$20k_B T$ lower energy than if the third bead is far away), but nonetheless the linear configuration of particles is formed in more than 95% cases due to the potential barrier which directs the third particle to either end of the pair.

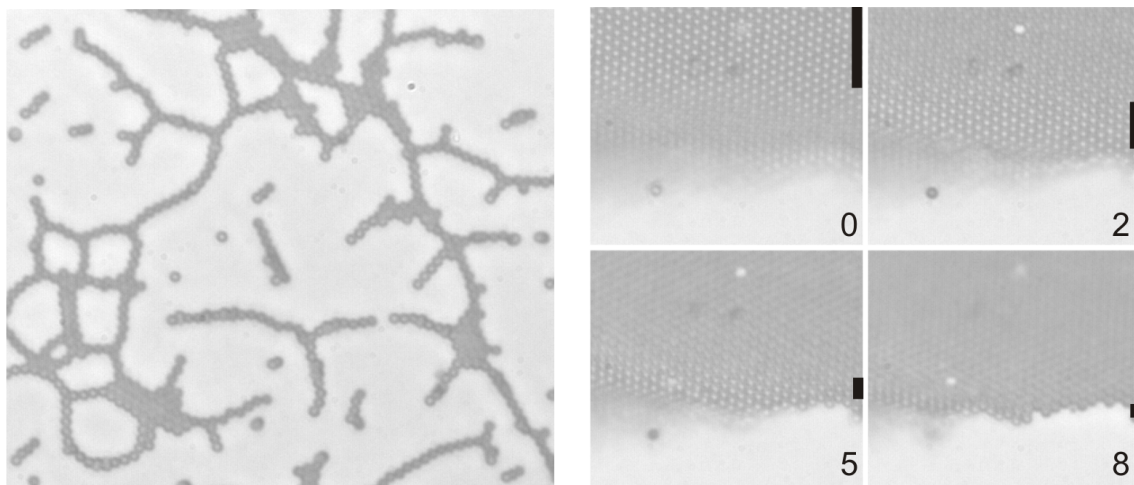


FIGURE 4.27: Micrographs of HCP colloidal sheets ($\theta_p = \theta_m$, $B_0 = 3.5$ mT). *Left:* Where the local filling fraction of particles is high, chains merge into 2D structures. *Right:* Micrographs of a self-assembled sheet taken at different microscope focal planes. The number in each image is the height in μm of the focus with respect to the cell bottom. Black stipes indicate the focused region of the image.

When double chains are formed and there are available single beads or free chains in the vicinity, the formation of triple chains begins. Free beads or chains are always adsorbed into the plane of the first two chains. The growth goes on until there are no available building blocks anymore. The resulting structures are 2D HCP sheets as demonstrated in Fig. 4.27.

Sheets are stable regardless of their orientation in space. In fact, it is possible to bend them (using optical tweezers) without disrupting their stability. This is demonstrated in Fig. 4.27, where we show 4 micrographs of a sheet, taken at four different focal planes. They confirm that the sheet is bent upwards and stable.

Due to sedimentation colloidal sheets settle to the bottom of the sample cell as shown in the left micrograph of Fig. 4.28. Slight decrease of the field cone opening angle eliminates the isotropic nature of the interaction - vertically aligned sheets become more energetically favorable. Smaller clusters reorient in a matter of seconds, while the edge regions of larger sheets start bending upwards. The process finishes when sheets reorient into vertical position and form tube-like structures.

To understand the assembly of chains from single beads and the formation of sheets from single chains, we have numerically calculated the energies involved in the process. The model, used for calculations presented in Fig. 4.29, assumes that the equally separated beads join into chain by the reduction of their separation. The results of the per-particle energy calculation as a function of separation are in agreement with the experimental observations - chains are energetically more favorable structure than separated particles. The calculation has been performed for two chain lengths: the shortest possible chain of 2 particles and an "infinitely" long chain, modeled by 200 particles. In the case of the short chain, the resulting

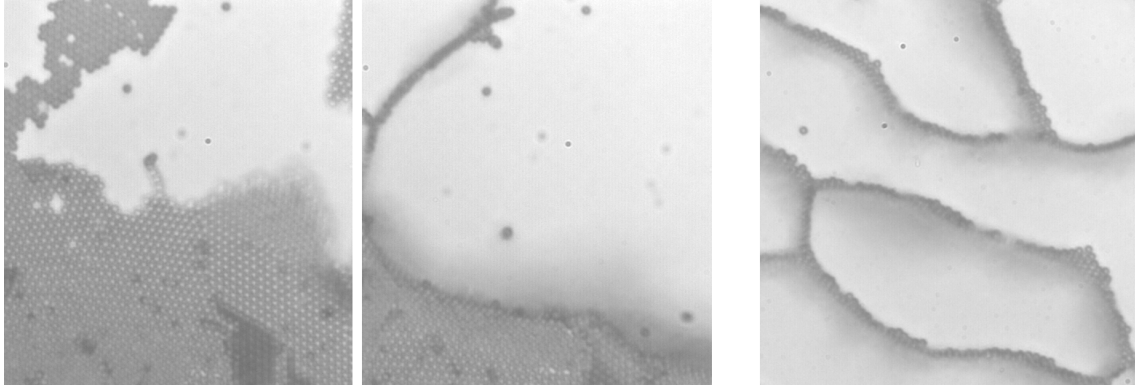


FIGURE 4.28: The effect of decreased field opening angle on colloidal sheets. *Left*: initial state $\theta_p = \theta_m$, the sheets have settled to the bottom of the cell due to gravity. *Middle*: After the tiny decrease of θ_p the favorable configuration are vertically aligned sheets. Smaller separated clusters of sheets undergo complete reorientation, while larger sheets start bending upwards. *Right*: The equilibrium formation is the network of vertically aligned sheets (tube-like).

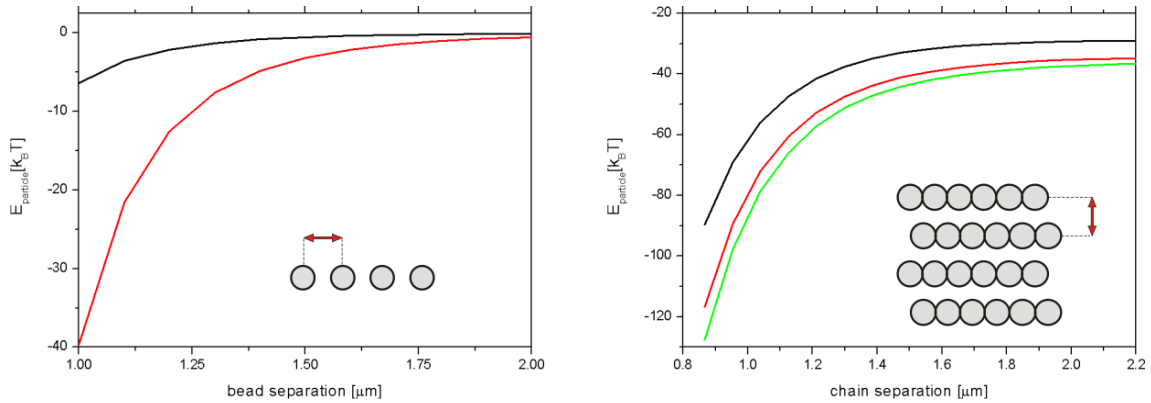


FIGURE 4.29: Calculated energy per particle in the assembly of colloidal structures as a function of separation. *Left*: Assembly of N single beads into a linear chain. Energy per particle for $N = 2$ (black) and $N = 200$ beads (red). *Right*: Assembly of N colloidal chains of N beads into 2D HCP sheets. Energy for $N = 10$ (black), $N = 20$ (red) and $N = 30$ (green).

energy vs. separation dependence is of course the $1/r^6$ pair potential. Particles in the longer chain are bound approximately 7 times stronger than a pair of particles in contact. The functional form of per-particle energy as a function of separation follows $1/r^{6.3}$ dependence.

The formation of 2D HCP sheets from single chains is energetically favorable process. Right chart of Fig. 4.29 presents the energy per particle of N chains, each made of N beads, as a function of chain separation. In order to characterize the finite size effects the calculation has been performed for $N = 10, 20$ and 30 . The energy vs. chain separation dependence can be fitted with a power-law with the critical coefficient $\beta = 4.2$.

To explain the sheet stability we calculated the energy landscape around an axially symmetric HCP planar sheet composed of 19 particles: one in the center

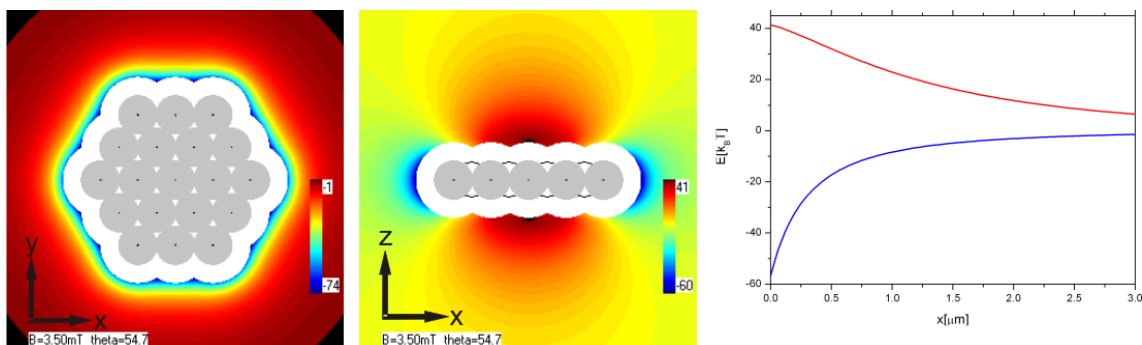


FIGURE 4.30: Planar sheet of 19 particles, arranged in HCP configuration. $\theta_p = \theta_m, B_0 = 3.5$ mT. *Left*: The xy energy landscape around a sheet. *Middle*: The xz energy landscape around the sheet. *Right*: Calculated addition to the total energy as a function of surface-to-surface separation between the sheet and a probe particle. If the probe particle is in plane of the sheet, the potential is attractive (blue). If the probe is on the plane normal, the potential is repulsive (red).

of the coordinate system, 6 around it in the first layer and additional 12 in the second layer (Fig. 4.30). If the probe particle is located in the sheet plane (xy) the interaction is attractive. If it is above or below the sheet in the normal plane (xz) that includes the sheet center, the potential is repulsive. In the right chart we plotted the energy as a function of surface-to-surface separation between the sheet and a probe particle on the two special lines. This calculation explains why the HCP sheets are stable structures - if there are any free particles near the sheet plane, they are drawn into the sheet, while on the contrary particles above or below the sheet are repelled away.

A spherically isotropic $1/r^6$ attractive potential around a single bead promotes the formation of pairs. The pair potential has the cylindrical symmetry - attraction in the direction of long axis and repulsion in the perpendicular direction. Such potential stabilizes chains, 1D structures. The potential around a sheet of particles is attractive in sheet plane and repulsive in perpendicular direction, therefore it stabilizes sheets, 2D structures. A logical question is whether 3D structures are stable as well.

To answer this question we have analyzed the energy of a single particle approaching a planar sheet from the transverse direction. Left chart of Fig. 4.31 shows the energy vs. surface-to-surface separation dependence for different sheet sizes. If sheet is made of one bead only, the interaction is familiar pair attraction. If 6 beads are added around the central bead (sheet has diameter of 3σ), the interaction changes to repulsive. Adding another layer of beads (sheet diameter is now 5σ) makes the interaction even more repulsive. Interesting transition occurs when 3 more layers of beads are added around the sheet: the interaction between the single particle and the sheet is still repulsive, but at very small separations there is a minute potential well - the particle is weakly bound to the sheet. If the sheet diameter is increased, then the potential well becomes even larger. A single particle is therefore stable if it is pushed into a contact with a large sheet of particles.

To check the stability of 3D structures we have calculated the energy of 2D HCP sheets merging into a 3D HCP crystal. Right chart of Fig. 4.31 displays per-particle

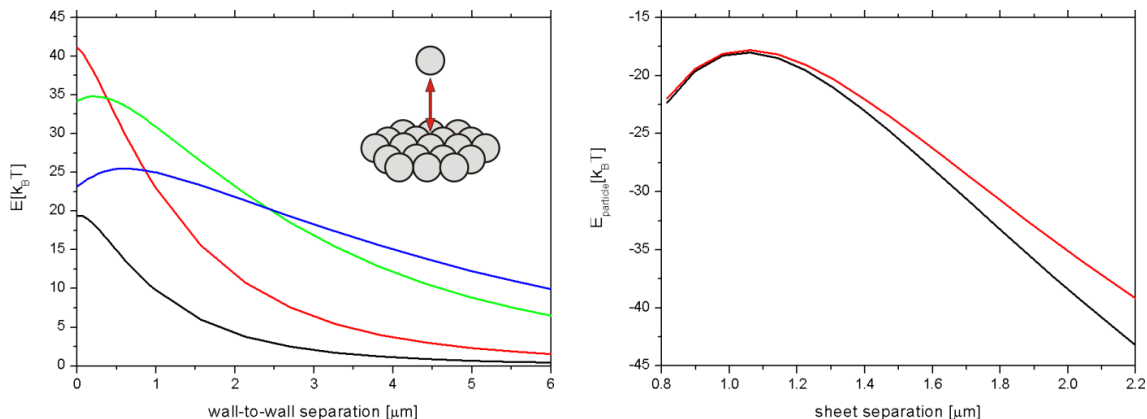


FIGURE 4.31: *Left*: Calculated energy for a single bead approaching to 2D hexagonal close-packed crystal as a function of separation. Different colors denote different diameters (sizes) of sheets: black - 3σ (7 beads), red - 5σ (19 beads, inline schematic), green - 11σ (92 beads) and blue - 17σ (218 beads). *Right*: Joining of N HCP sheets of $N \times N$ beads into 3D crystal. The energy per particle as a function of sheet separation for $N = 10$ (red) and $N = 20$ (black).

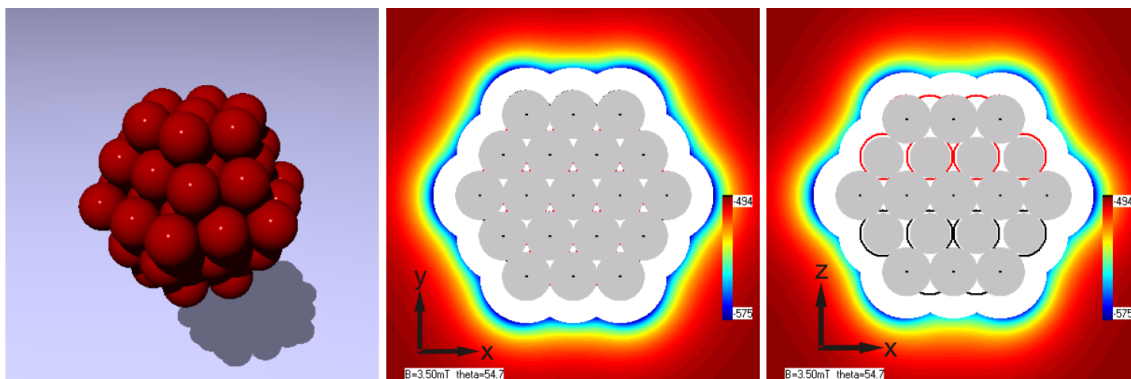


FIGURE 4.32: Hexagonal close-packed crystallite formed of 57 beads. *Left*: The crystallite is made of 5 HCP layers consisting of 7, 12, 19 (central), 12 and 7 particles. *Middle*: The xy energy landscape. *Right*: The xz energy landscape.

energy as a function of sheet separation for two sizes of crystals. Similar to the case, when a single bead approaches to HCP sheet, the energy dependence includes a potential barrier: HCP sheets have to be pushed together, but once a 3D crystal is formed, it remains stable.

Our final calculation, the potential landscape around a small crystallite, composed of 57 beads, is presented in Fig. 4.32. As expected, the potential around globular 3D crystallite is isotropically attractive.

4.8 Conclusion and outlook

We performed an experimental study of the relationship between the interparticle interactions and the structure formation in a system of micrometer-sized superparamagnetic colloidal particles. The interaction was induced by the external mag-

netic field and controlled by the spatial constraints. The focus was on two types of isotropic interaction potentials: core-softened repulsion in 2D and isotropic $1/r^6$ attraction in 3D.

In a system with the core-softened repulsive interaction several self assembled mesophases were formed depending on the surface filling fraction. We observed the square, hexagonal and honeycomb lattices as well as the labyrinthine structure. This was the first experimental validation of theoretical predictions pertaining to similar pair interactions [21, 22, 76]. The observed two-dimensional structures could have also applicative value as they could be used as templates to promote the growth of colloidal crystals [87, 88].

More complex interparticle potentials were realized by the precession of the magnetic field on a surface of a cone. The variation of the cone opening angle θ_p was used to precisely tune the ratio between dipolar repulsion and attraction. At the opening angle, equal to the magic angle $\theta_m \approx 54.7^\circ$, the $1/r^3$ term of dipolar interaction vanishes. The dominant term in the pair potential was found to be $1/r^6$ isotropic attraction which arises due to the effect of the local magnetic fields. Another striking feature of the system is the many-body effect.

Isotropic $1/r^6$ attraction between the particles and the pair-wise non-additivity of the interaction promote the formation of colloidal pairs from single particles, the growth of longer chains out of particle pairs and larger hexagonal close-packed sheets from small planar clusters and finally the growth of 3D crystals from small crystallites.

In principle the interaction can be made even more complex by the addition of other external fields. A simple upgrade of the system would be charged beads and consequently additional $1/r^3$ electrostatic interparticle repulsion. More complex examples include the use of anisotropic solvent (liquid crystals) or different background potentials, such as patterned substrates or light induced potentials.

As demonstrated, the magic angle system could be used to study the interactions between superstructures, manually assembled with optical tweezers or produced in microfluidic circuitry. The crystallization and coalescence of vesicles or more complicated structures could be examined in a system of (decorated) colloidal rings.

In conclusion, the magneto-optical tweezers turned out to be the versatile tool to tailor complex interparticle interactions and study the induced condensed phases.

Viscoelastic properties of bacterial networks

In the last two decades a number of rheological techniques has been developed to measure the material properties of soft matter systems on microscopic scales. These microrheological (MR) techniques can be divided into two broad classes, *passive* and *active*, and both classes are further divided according to number of probe particles used to *one-particle* and *two-particle* MR. Typically, the MR techniques are demonstrated in homogeneous materials, such as polymer solutions or gels, whereas its use in complex biological materials is far more complex. In this Chapter we present a comparison of 3 MR methods, which were used to measure the viscoelastic modulus of the extracellular matrix of bacteria *Vibrio* sp. We employed optical tweezers for micromanipulation of $3.22\ \mu\text{m}$ silica probe particles and high resolution video tracking to perform passive one-particle MR and active one- and two-particle MR. The methods were first tested on water and then used to monitor the temporal evolution of mechanical properties of the growing extracellular matrix. The stiffness of the matrix was found to be very small, less than $2 \times 10^{-6}\ \text{N/m}$, whereas its viscosity changes with time and reaches a maximum of approximately $\eta \approx 3.3 \times 10^{-3}\ \text{Pas}$.

5.1 Introduction

Many material properties of soft matter systems originate from their complex structures and dynamics with multiple characteristic length- and time-scales. An important and consequently frequently studied material property is the shear modulus. Contrary to ordinary solids, the shear modulus of soft materials usually exhibits significant frequency dependence. Such materials are viscoelastic - they exhibit both a viscous and an elastic response to applied stress. *Rheology*, the experimental and theoretical study of viscoelasticity is of fundamental and practical significance. The measurement of bulk viscoelastic properties has been traditionally performed with mechanical rheometers that probe macroscopic milliliter samples by applying a small amplitude oscillatory shear strain $\gamma(t) = \gamma_0 \sin(\omega t)$ and measuring the resultant shear stress. The upper frequency that can be probed using commercial rheometers is limited to few tens of Hz due to the inertial effects of probe plates.

The material structure is not significantly deformed and remains in equilibrium if the shear strain amplitude γ_0 is small. In this case, the time-dependent stress $\sigma(t)$ is linearly proportional to the strain,

$$\sigma(t) = \gamma_0[G'(\omega) \sin(\omega t) + G''(\omega) \cos(\omega t)]. \quad (5.1)$$

Here $G'(\omega)$ is the response in-phase with the applied strain and is called the *elastic* or *storage modulus*, a measure of the storage of elastic energy by the sample. $G''(\omega)$ is the response out of phase with the applied strain, and in phase with the strain rate, and is called the *viscous* or *loss modulus*, a measure of viscous dissipation of energy. The frequency dependent complex shear modulus (or viscoelastic modulus) [89] is defined as

$$G(\omega) = G'(\omega) + iG''(\omega). \quad (5.2)$$

In the last two decades a number of techniques has been developed to probe the material properties of soft matter systems ranging from polymer solutions to the interior of living cells on microscopic scales. These techniques are called *microrheology* (for a review see [90, 91, 92]), as they can be used to locally measure viscoelastic parameters. Microrheology has several advantages compared to traditional bulk rheometry. Only small quantities of samples are needed for microrheologic measurements (typically 1 μ l is enough), which is very convenient for biological systems. Another advantage is the possibility to study inhomogeneous environments, for instance cell interiors. Also the upper range of accessible frequencies is higher, up to 10^5 Hz. This enables new insights into the microscopic basis of viscoelasticity in these systems.

There are two broad classes of microrheological techniques: *active* and *passive*. Passive MR techniques rely on fluctuations of probe particles due to thermal noise. Typically chemically inert spherical beads with a diameter between few tens of nanometers to several micrometers are embedded in the material, their free diffusion is observed either with dynamic light scattering [25], laser tracking [26] or videomicrocopy [27] and then a linear shear modulus is calculated.

Active MR techniques involve the active manipulation of small probes. The earliest experimental realization of active MR was based on the manipulation of magnetic beads with an external magnetic field [28] almost a century ago. Nowadays micromechanical tools such as micropipettes [29] and atomic force microscopes [30] are used to directly strain materials, while optical tweezers [31] or magnetic bead microrheometers [32, 33, 34] are used to actively manipulate microparticles embedded in materials. These measurements are analogous to conventional mechanical rheological techniques in which an external stress is applied to a sample, and the resultant strain is measured to obtain the shear moduli. In this case, micron-sized probes locally deform the material and probe the *local* viscoelastic response. Active measurements allow the possibility of applying large stresses to stiff materials in order to obtain detectable strains. They can also be used to measure non-linear behavior if sufficiently large forces are applied to strain the material beyond the linear regime.

5.1.1 Passive microrheology

In passive MR measurements the rheological properties are obtained from Brownian motion of probe particles that are embedded into a material before the measurement. Particles are tracked either with videomicroscopy (hence also the name "particle-tracking MR") or laser tracking (photodiode detection of laser light scattered from a probe particle). Resolution of the position detection limits the range of materials, because they must be sufficiently soft in order for particles to move detectably with only $k_B T$ of available energy.

To understand how the thermal motion of embedded micron-sized particles is used to probe the frequency dependent rheology of the surrounding viscoelastic material, it is useful to first consider the motion of spherical tracers in a purely viscous fluid and then generalize to account for elasticity. Micron-sized beads in a purely viscous medium undergo Brownian motion. The dynamics of particle motions is revealed in the position correlation function, also known as the mean square displacement (MSD), defined as:

$$\langle \mathbf{r}^2(\tau) \rangle = \langle |\mathbf{r}(t + \tau) - \mathbf{r}(t)|^2 \rangle \quad (5.3)$$

where \mathbf{r} is the d -dimensional particle position, τ is the lag time and the brackets indicate an average over the interval of the measurement. The time-average assumes the fluid is always in thermal equilibrium and the material properties do not evolve in time. The diffusion coefficient D of the Brownian particle in d -dimensional space is obtained from the Einstein-Smoluchowsky diffusion equation,

$$\langle \mathbf{r}^2(\tau) \rangle = 2dD\tau. \quad (5.4)$$

The viscosity η of the fluid can be obtained using the Stokes-Einstein relation

$$D = \frac{k_B T}{6\pi\eta a}, \quad (5.5)$$

once the MSD is known. Here k_B is the Boltzmann constant, T is the temperature and a is the radius of beads.

On the other hand, motion of the particles in an elastic medium is constrained therefore the MSD reaches an average plateau value $\langle r_p^2 \rangle$ that is set by the elastic modulus of the material. By equating the thermal energy $k_B T$ of each bead with its elastic energy $\frac{1}{2}k_m \langle r_p^2 \rangle$, the effective spring constant k_m of the surrounding medium can be obtained. The elastic modulus G' is related to the spring constant by a factor of characteristic length (set by bead radius a). Using such an energy balance argument, the relation between the elastic modulus and the MSD reads

$$G' \sim \frac{k_B T}{\langle r_p^2 \rangle a}. \quad (5.6)$$

Maximum passively accessible elastic modulus depends on both the size of the embedded probe and on the ability to resolve small particle displacements of order of r_p . The resolution of a particle position detection typically ranges from 1 to 10 nm,

thus allowing measurements (with micron-sized probes) of samples with an elastic modulus up to 50-5000 Pa. This range is relatively small compared to that accessible by active MR, but is sufficient to study many interesting complex materials.

Viscoelastic properties of soft matter exhibit frequency and length scale dependent response and are therefore characterized by the frequency dependent complex shear modulus G . For such materials, thermally driven motion of embedded probes reflects both the viscous and elastic contributions. Unlike a purely viscous fluid where the MSDs evolve linearly with time (5.4), or elastic material where maximum MSDs are limited, the MSDs of tracers in a complex material scale differently with the lag time τ :

$$\langle \mathbf{r}^2(\tau) \rangle \sim \tau^\alpha, \quad (5.7)$$

where α is the diffusive exponent. Depending on the material, the particles may exhibit subdiffusive ($0 < \alpha < 1$) or superdiffusive motion ($\alpha > 1$) or even become locally constrained at long times ($\alpha = 0$).

The relationship between ensemble-averaged mean squared displacement of tracer particles in a viscoelastic medium and its complex elastic modulus can be described by generalized Stokes-Einstein equation (GSE), proposed by Mason and Weitz [93]. It is obtained from a combination of Laplace transform of generalized Langevin equation and the equipartition theorem. When thermally driven embedded probe particles are large compared to all structural length scales, the GSE for d -dimensions reads

$$\tilde{G}(s) = \frac{d k_B T}{3\pi a s \langle \tilde{r}^2(s) \rangle}, \quad (5.8)$$

where s is the Laplace frequency, $\langle \tilde{r}^2(s) \rangle$ and $\tilde{G}(s)$ are the Laplace transforms of $\langle r^2(t) \rangle$ and $G(t)$. The linear frequency dependent viscoelastic response is therefore directly obtained from the MSD of thermal tracers. To compare with bulk rheology measurements, $\tilde{G}(s)$ is transformed into the Fourier domain ($s \rightarrow i\omega$) to get complex shear modulus $G(\omega)$ which is the same quantity as measured with a conventional mechanical rheometer.

Passive particle-tracking MR, i.e. the measurement of a viscoelastic modulus from the motion of embedded probe particles has a few drawbacks. Freely diffusing particles often exit from the field of view, most often they diffuse out of a focal plane of the microscope. The results are affected by the size of probe particles [94], since GSER is valid only for particles larger than all characteristic length scales of a material under investigation. To overcome these problems, large particles have to be used, but they tend to sink to the bottom of a sample cell and render the measurement impossible. In heterogenous materials high concentration of probes have to be added to ensure that all regions of interest contain tracers, but might affect the rheological properties of the material.

5.1.2 Optical tweezers microrheology

The drawbacks of the passive particle tracking MR can be avoided by the use of optical tweezers. A probe particle is held inside a detection zone by optical trap,

therefore only the selected volume of material is investigated (especially convenient for heterogenous samples, such as living matter) and its motion can be tracked for a long time since the probe can't escape from the field of view. Positions can be monitored using laser-particle tracking (quadrant photodiode detection using back-focal-plane interferometry) which covers up to five-decades in frequency range. Even if video-tracking is being used, only a small region of interest around the probe particle has to be recorded, which enables high frame rates (up to 1000 Hz with standard commercially available CMOS cameras).

Optical tweezers can be also employed for active MR, which is required when thermal fluctuations can't induce measurable level of deformation or when the high-deformation response is studied. In one-particle active MR measurement, the probe particle is trapped in an optical trap with oscillating position [31, 35]. From the probe's trajectory the amplitude and the phase lag of its response are extracted and used to calculate complex viscoelastic modulus of the investigated media.

Two-particle active MR involves two optical traps [36]. One particle is trapped in a harmonically oscillating stiff trap and is thus actively deforming the surrounding medium, while a second particle is trapped in a weak stationary trap and is used to monitor the deformation of the medium at a desired location (Fig. 5.1).

5.1.3 One-particle passive MR

Motion of an optically trapped bead with radius a in a purely viscous medium is described by the Langevin equation,

$$kx(t) + \beta\dot{x}(t) = f_R(t), \quad (5.9)$$

where k is the trap stiffness, β the viscous drag coefficient and f_R is the random thermal force acting on the bead. In the Newtonian limit, where viscosity η is time independent for all time scales, the drag coefficient is given by $\beta = 6\pi\eta r$. In complex fluids the viscoelastic response can be time-dependent and is therefore described by the complex shear modulus $G(\omega)$. In linear regime it is possible to relate the Fourier transform of trapped bead's motion $x(\omega)$ to the Fourier transform of the thermal force $f_R(\omega)$ [95, 96] by

$$x(\omega) = \alpha(\omega) \cdot f_R(\omega), \quad (5.10)$$

where $\alpha(\omega) = \alpha'(\omega) + i\alpha''(\omega)$ is the complex compliance. If a trapped bead is in thermal equilibrium with the environment, the fluctuation-dissipation theorem can be used to obtain the imaginary part of the compliance from the experimentally measured power spectrum density of bead motion $S(\omega)$:

$$\alpha''(\omega) = \frac{\omega S(\omega)}{4k_B T}. \quad (5.11)$$

The real part of the compliance is calculated using the Kramers-Kronig dispersion relation

$$\alpha'(\omega) = \frac{2}{\pi} \int_0^\infty \cos(\omega t) \int_0^\infty \alpha''(\omega') \sin(\omega' t) d\omega' dt. \quad (5.12)$$

This requires the knowledge of $\alpha''(\omega)$ over whole frequency range. If laser-particle tracking is used, the frequency range spans to about 10^5 Hz, but nonetheless care

must be taken in interpreting $\alpha'(\omega)$ because the cosine and sine transforms of finite samples can lead to discontinuities or nonsensical data corresponding to the lowest and highest frequencies studied [97].

Once the compliance is known the complex shear modulus can be expressed using generalized Stokes-Einstein relation

$$G(\omega) = \frac{1}{6\pi a \alpha(\omega)}, \quad (5.13)$$

which holds for an incompressible medium without inertia. Expression is valid only if bead radius a is larger than the mesh size of the network.

5.1.4 One-particle active MR

Optical tweezers can be used to drive the probe particle and thereby actively deform the media. The local mechanical properties are calculated from the spatio/temporal response of the embedded probe. The equation of motion for the spherical probe with radius a , neglecting the inertial term and thermal fluctuations, is

$$[k + k_m]x(t) + 6\pi\eta a\dot{x}(t) = kA \sin(\omega t), \quad (5.14)$$

where η is the solvent viscosity and $k_m = 24\pi G' a(1 - \nu)/(5 - 6\nu)$ is the local stiffness of a material with shear modulus G' and Poisson ratio ν , k is the trap stiffness and A and ω are the amplitude and angular frequency of the trap movement [31, 98]. The response of the bead to oscillating force is

$$x(t) = D(\omega) \sin[\omega t - \delta(\omega)], \quad (5.15)$$

with the ratio of amplitudes is

$$d(\omega) = \frac{D(\omega)}{A} = \frac{k}{\sqrt{(k + k_m)^2 + (6\pi a \eta \omega)^2}}, \quad (5.16)$$

and the phase lag

$$\delta(\omega) = \arctan \frac{6\pi a \eta \omega}{k + k_m}. \quad (5.17)$$

The viscoelastic moduli are calculated as

$$\begin{aligned} G'(\omega) &= \frac{k_m(\omega)}{6\pi a} = \frac{k}{6\pi a} \left[\frac{\cos \delta(\omega)}{d(\omega)} - 1 \right], \\ G''(\omega) &= \omega \eta(\omega) = -\frac{k}{6\pi a} \left[\frac{\sin \delta(\omega)}{d(\omega)} \right]. \end{aligned} \quad (5.18)$$

Moduli in 6.23 are scaled by the trap stiffness k , which depends on the refractive index contrast between the trapped particle and suspending medium. If the refractive index of a suspending medium changes (e.g. some sugar is added into water), the stiffness of a trap is changed, which has to be taken into account when calculating the moduli.

In one-particle MR measurements tracers probe viscoelasticity on length scales comparable to their size. In materials heterogeneous on those scales, tracer motion depends on both the local and the bulk rheology in a complex way [99]. Varying probe diameter gives qualitatively different information about network mechanics. When embedded probe particles are larger than all structural length scales of the material, one-particle MR results in a true complex elastic modulus. By contrast, when the embedded particles are approximately equal to or smaller than the structural length scales of the material, particles move within small, mechanically distinct microenvironments and thus their dynamics are no longer directly related to the bulk viscoelastic response [100] but rather to the viscosity of the solvent.

Improper size of the probes is not the only possible reason for artifacts in one-particle MR results. Chemical interactions between the probes and a surrounding medium have also strong influence on MR analysis [101], e.g. either probes can adsorb molecules of the medium or a depletion layer is created.

5.1.5 Two-particle active MR

These limitations are not present in two-particle microrheology, in which the correlated motion of pairs of particles is analyzed to measure the deformation of a network [102]. Two-particle microrheology is insensitive to local heterogeneities since it probes the response on a length scale defined by the separation between probe particles. It is also less dependent on the coupling between the probe and the medium [101].

In two-particle active MR a complex viscoelastic modulus of the sample is determined from the response of a *probe* particle to an oscillating force applied to *drive* particle (Fig. 5.1). Let $(x^{(1)}, y^{(1)})$ denotes the position of the drive particle, $(x^{(2)}, y^{(2)})$ the position of the probe particle and the coordinate system be chosen such that x -axis is parallel (\parallel) and y -axis perpendicular (\perp) to the line connecting the particle centers. In an isotropic homogeneous medium the full linear response is defined by the complex compliance in the direction of beads $\alpha_{\parallel}(\omega)$ and in the perpendicular direction $\alpha_{\perp}(\omega)$. In Fourier space, the response of the probe particle (2) to arbitrary force F , applied to drive particle (1), is in absence of any optical traps written as [103, 104]

$$\begin{aligned} x^{(2)}(\omega) &= \alpha_{\parallel}(\omega) F_x^{(1)}(\omega) \\ y^{(2)}(\omega) &= \alpha_{\perp}(\omega) F_y^{(1)}(\omega) \end{aligned} \quad (5.19)$$

In active two-particle optical tweezers MR, both particles are held in optical traps. The trapping potential affects the response of the probe bead, therefore the measured response functions A_{\parallel} and A_{\perp} differ from the true rheological responses α_{\parallel} and α_{\perp} of the material. The displacements of the probe particle to the force acting on the drive particle is

$$\begin{aligned} x^{(2)}(\omega) &= A_{\parallel}(\omega) F_x^{(1)}(\omega) \\ y^{(2)}(\omega) &= A_{\perp}(\omega) F_y^{(1)}(\omega). \end{aligned} \quad (5.20)$$

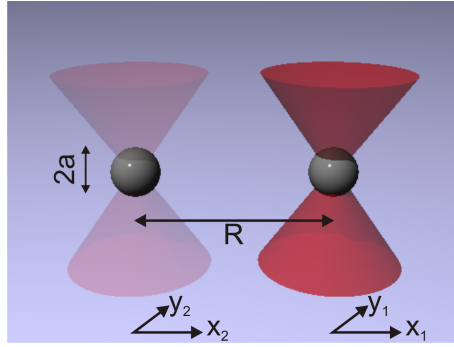


FIGURE 5.1: Schematic of two-particle MR experiment. A pair of silica spheres with radius a is trapped by a pair of optical traps at a separation R .

The same displacements can be also expressed directly in terms of single particle compliance α (5.10), the mutual response functions α_{\parallel} and α_{\perp} (5.19), the trapping forces $-k^{(i)}r^{(i)}$ and the other forces $F^{(i)}$, applied to particles, as

$$\begin{aligned} x^{(2)}(\omega) &= \alpha^{(2)}[F_x^{(2)} - k^{(2)}x^{(2)}] + \alpha_{\parallel}[F_x^{(1)} - k^{(1)}x^{(1)}] \\ y^{(2)}(\omega) &= \alpha^{(2)}[F_y^{(2)} - k^{(2)}y^{(2)}] + \alpha_{\perp}[F_y^{(1)} - k^{(1)}y^{(1)}]. \end{aligned} \quad (5.21)$$

The drive particle is confined in an optical trap with oscillating position $x_0(t) = A \sin(\omega t)$ which results in a net force $k^{(1)}[x_0(t) - x^{(1)}]$ acting on the drive particle. The apparent force on the first particle in (5.21) is therefore $F_x^{(1)} = k^{(1)}x_0(t)$. The equations (6.24) and (5.21) can be combined to express the apparent response functions A_{\parallel} and A_{\perp} of the second particle as

$$\begin{aligned} A_{\parallel} &= \frac{\alpha_{\parallel}}{(1 + k^{(1)}\alpha^{(1)})(1 + k^{(2)}\alpha^{(2)}) - k^{(1)}k^{(2)}\alpha_{\parallel}^2} \\ A_{\perp} &= \frac{\alpha_{\perp}}{(1 + k^{(1)}\alpha^{(1)})(1 + k^{(2)}\alpha^{(2)}) - k^{(1)}k^{(2)}\alpha_{\perp}^2}. \end{aligned} \quad (5.22)$$

The mutual response functions α_{\parallel} and α_{\perp} of an incompressible continuum with shear modulus $G(\omega)$ are given by the generalized Oseen tensor [99]

$$\begin{aligned} \alpha_{\parallel} &= \frac{1}{4\pi R G(\omega)} \\ \alpha_{\perp} &= \frac{1}{8\pi R G(\omega)}, \end{aligned} \quad (5.23)$$

where R is the distance between the particles. Single particle complex compliances (in the case of particles with same radius) are

$$\alpha^{(1)} = \alpha^{(2)} = \frac{1}{6\pi a G(\omega)}, \quad (5.24)$$

where a is the particle radius. The expression for viscoelastic modulus,

$$G(\omega) = G'(\omega) + iG''(\omega) = \frac{k_m}{6\pi a} - i\omega\eta, \quad (5.25)$$

is used in (5.23) and (5.24) which are then inserted into (5.22) to obtain expressions for A_{\parallel} and A_{\perp} in terms of medium viscosity η and stiffness k_m . In a two-particle active MR experiment the frequency dependence of A_{\parallel} and A_{\perp} is measured then (5.22) is fitted to extract η and k_m .

5.1.6 Rheology of bacterial networks

Bacteria are unicellular microorganisms with typical size of a micrometer, existing in many different shapes, from spheres to rods and spirals. Single cell organisms generally exhibit two different modes of behavior - the first is known as a free floating, where single cells independently float or swim in liquid medium, whereas the second mode is a formation of biofilms where cells are closely packed and firmly attached to each other. Biofilms are produced by excretion of protective and adhesive matrix; their common properties are attachment to surrounding surfaces, structural diversity, complex interactions and extra cellular matrix of polymer substances. The advantages of such environment is enhanced protection of the interior of the community from the unfavorable environment. Due to their role in microbial infections the mechanical properties of biofilms have been widely studied both on macroscale with classical rheometers [105] and on a microscale: with microindentation device [106], AFM, magnetic tweezers, optical tweezers and by observation of Brownian motion of embedded particles.

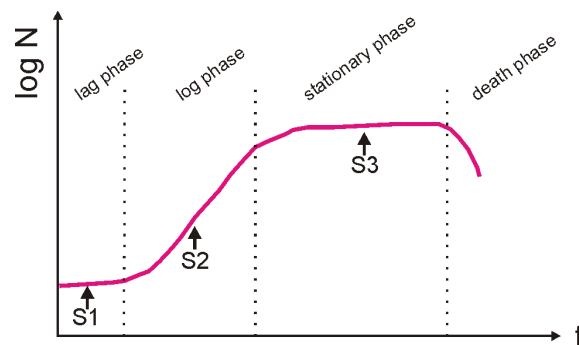


FIGURE 5.2: Bacterial growth curve: logarithm of number of bacteria as a function of time. Arrows indicate at which points samples S1, S2 and S3 were taken for MR measurement.

In this Chapter rather than to a formed biofilm of close packed cells we focused to an earlier stage in a development of multi-cellular environment - we were monitoring the rheology of growing population of bacterial cells. When a bacterium is added to nutritious environment, it divides into daughter cells in a process called binary fission. The division repeats again and again and the number of bacteria increases. Its time dependence is described by a growth curve (Fig. 5.2), which can be divided into four phases. In initial, *lag phase* the growth is slow, because the bacteria need some time to accommodate to the food and nutrients in their new habitat, but as soon as the metabolic machinery of bacteria is adapted the growth comes into *log phase* where their number is exponentially growing. As more and more bacteria are competing for dwindling nutrients, booming growth stops and the number of

bacteria stabilizes; this is called *stationary phase*. The last is a *death phase*, when bacteria begin to die due to accumulated toxins and depletion of food.

We measured the microrheology of a bacterial solution consisting of a growth medium, bacterial cells and the extracellular matrix (ECM), which is composed of an interlocking mesh of fibrous proteins and long unbranched polysaccharides. Components of the ECM are produced intracellularly by bacterial cells, and secreted into the ECM via exocytosis [107]. Once secreted they aggregate with the existing matrix, so the matrix is getting denser through the time.

The bacterial culture was growing in optimal conditions, described below in Sec. 5.2.1. At desired time intervals 2 ml samples were taken from the center of the growth flask and their optical density was measured to determine their position in the growth curve. The samples were then prepared for MR measurements as described in the following Section.

5.2 Experimental details

We have used plain silica beads of radius $a = 1.61 \mu\text{m}$ (Bangs Labs, SS05N) as probe particles for MR. Since their index of refraction ($n_B = 1.43$) is close to that of water ($n = 1.33$) silica beads can be optically trapped in three dimensions but on the other hand their contrast is low, therefore beads with relatively large diameter had to be used for accurate detection of their positions in bacterial solutions. Typically, $1 \mu\text{l}$ of the beads, diluted in water to concentration $10^{-4}/\mu\text{m}^3$, was added to $500 \mu\text{l}$ of bacterial solution. After mixing, approximately $20 \mu\text{l}$ of solution was pipetted into a sample chamber, made of two coverslips of different sizes. Silicon grease was holding the coverslips separated at a distance of approximately $100 \mu\text{m}$ and was used to completely seal the chamber after filling. The measurements were performed at room temperature, with no special control over the chamber temperature.

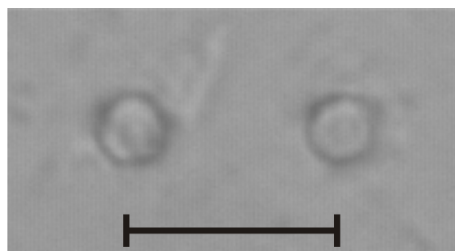


FIGURE 5.3: Micrograph of two trapped $3.22 \mu\text{m}$ silica beads in the bacterial solution. The scale bar is $10 \mu\text{m}$ long.

The laser power in all MR experiments was held constant at 300 mW, which resulted in about 30 mW of total power in the sample. Two simultaneous optical traps, each with one trapped particle (Fig. 5.1), were used for all types of MR experiments. A passive and active one- and two-particle MR measurements of one sample consisted of following steps. First, two probe beads were found at the bottom of the sample chamber and trapped in two traps that were $10 \mu\text{m}$ apart (Fig. 5.3).

Beads were then raised to 30 μm above the chamber bottom to avoid the influence of confining walls on the measurement.

For measurements of passive MR the traps were held at fixed positions. The particle fluctuations were recorded at three different traps stiffnesses: 20%, 50% and 100% of full stiffness. For active MR measurements, the left trap was held at fixed position at 20% of full stiffness and was used only to weakly trap the *probe* bead. The right trap's stiffness was set to maximum and was used to harmonically oscillate the right bead (*drive* bead), either in the direction of the line connecting the beads

$$x_T(t) = A_0 \sin(2\pi ft) \quad (5.26)$$

or in the perpendicular direction $y_T(t) = A_0 \sin(2\pi ft)$ with a constant amplitude $A_0 = 1 \mu\text{m}$. The measurements were performed for different oscillation frequencies f : 0.1, 0.2, 0.5, 1, 2, 5, 10, 20 and 50 Hz. The whole active MR measurement procedure was then repeated with the stiffness of the drive trap set to 50%.

5.2.1 Preparation of bacteria

We were measuring the viscoelastic properties of a solution in which bacterial strain *Vibrio* sp. DSM 14379 [108] was growing. This strain is a bacterium isolate from Škocjanski zatok, Slovenia, belonging to family Vibrionaceae, class Gamma Proteobacteria, phylum Proteobacteria. *Vibrio* is a Gram negative bacteria possessing a curved rod shape and is typically found in marine environments [109]. They do not form spores and are facultative anaerobes.

Bacteria were grown aerobically in a minimal medium (M9) overnight in the dark on a rotatory shaker at 200 rpm at 28°C. An inoculum (1% v/v) was transferred to a freshly prepared medium. The growth curve was determined by optical density (OD) at 650 nm (Iskra Photometer MA9510). Samples for MR measurements were taken during the lag (sample 1, 3h old, OD=0.019), log (sample 2, 9h old, OD=0.79), and stationary phase (sample 3, 26h old, OD=1.75). Another sample, "mesh-only", was prepared from the sample 3 with removal of bacteria by spinning.

5.3 Results and discussion

5.3.1 One-particle passive MR

All MR methods have been tested in water as a control and then used in complex bacterial environment. For one-particle passive MR measurement the trajectories $(x(t), y(t))$ of optically trapped probe beads were recorded. In Fig. 5.4 we present power spectral density $S(\omega)$ of probe fluctuations in water; the probe was trapped in an optical trap with stiffness $k = 2.1 \times 10^{-6}$ N/m. Measured data points in $S(\omega)$ were fitted with (2.5), yielding corner frequency $f_c = 10.3$ Hz and viscous drag coefficient $\gamma = 3.3 \times 10^{-8}$ Ns/m.

The power spectral density is directly related to the imaginary part of compliance $\alpha''(\omega)$. In our experimental setup we used video-particle tracking with the acquisition rate of 200 frames per second which limited the highest frequency of the measured

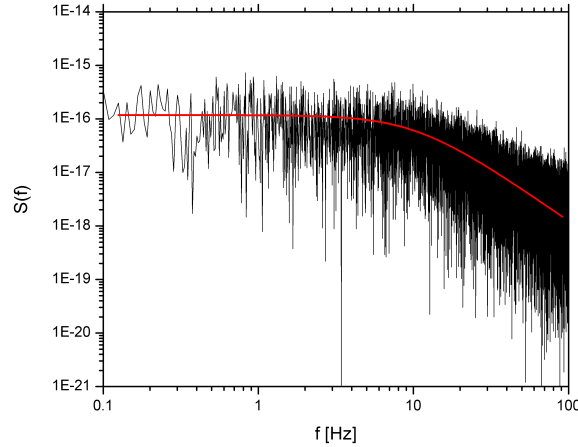


FIGURE 5.4: Power spectral density of fluctuations of a trapped $3.22 \mu\text{m}$ silica bead in water. Trap stiffness was $k = 2.0 \times 10^{-6} \text{N/m}$. Red line is fit of (2.5) with $\gamma = 3.3 \times 10^{-8} \text{Ns/m}$ and $f_c = 10.3 \text{ Hz}$.

power spectrum $S(\omega)$ and consequently $\alpha''(\omega)$ to 100 Hz, therefore (5.12) couldn't be evaluated numerically. Since the functional dependence of the spectral density is known (2.5), we used analytical expression for $S(\omega)$ for the evaluation of the real part of the compliance $\alpha'(\omega)$.

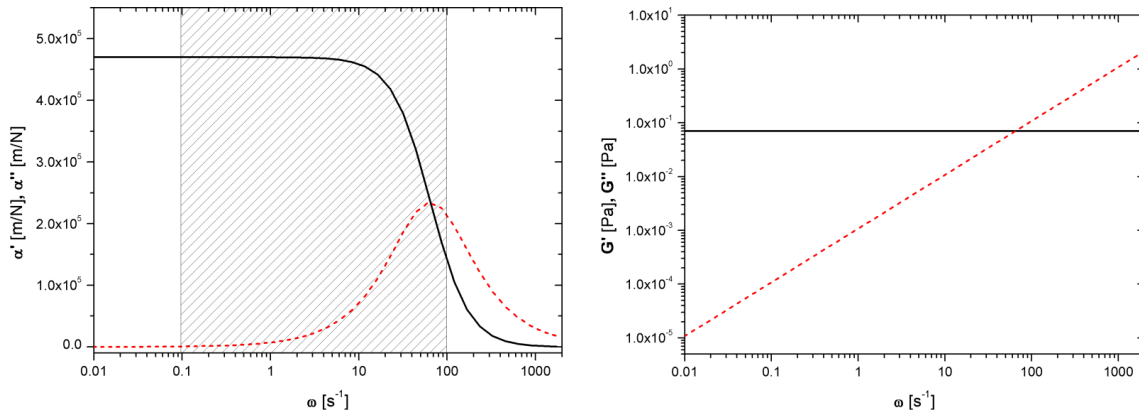


FIGURE 5.5: Compliance and shear modulus in water, calculated from the analytical expression for $S(\omega)$ of a trapped particle. *Left*: Real (black) and imaginary part (dashed red) of the complex compliance α of a weakly trapped probe particle as a function of angular frequency ω . The compliance was calculated using (5.11) and (5.12) from PSD in Fig. 5.4. Dashed region indicates the frequency range accessible by the video-particle tracking. *Right*: Real (black) and imaginary part (dashed red) of the complex shear modulus $G(\omega)$.

In Fig. 5.5 we show the real $\alpha'(\omega)$ and the imaginary part $\alpha''(\omega)$ of the calculated compliance of the probe particle in water. The obtained value, $\alpha'(0) = 4.7 \times 10^5 \text{ m/N}$, is in a good agreement with the theoretical prediction $\alpha' = 1/k = 4.8 \times 10^5 \text{ m/N}$. Using (5.13) a complex viscoelastic modulus $G(\omega)$ is calculated from the

complex compliance $\alpha(\omega)$. In right chart of Fig. 5.5 the storage (elastic) and loss (viscous) modulus of water are presented. The non-zero storage modulus $G'(\omega) = k/6\pi a = 0.07$ Pa is due to the stiffness of the optical trap. The loss modulus of a Newtonian liquid is proportional to the angular frequency, $G''(\omega) = -\eta\omega$. The measured viscosity of water $\eta = 10.8 \times 10^{-4}$ Pas is in a good agreement with true viscosity¹, which is $\eta = 9.3 \times 10^{-4}$ Pas at temperature of 23°C.

Another possibility to obtain a viscoelastic modulus with a passive one-particle MR is by the use of the generalized Stokes-Einstein equation. The complex shear modulus in the measured range of frequencies can be calculated directly from the MSD of trapped particles using GSER (6.20).

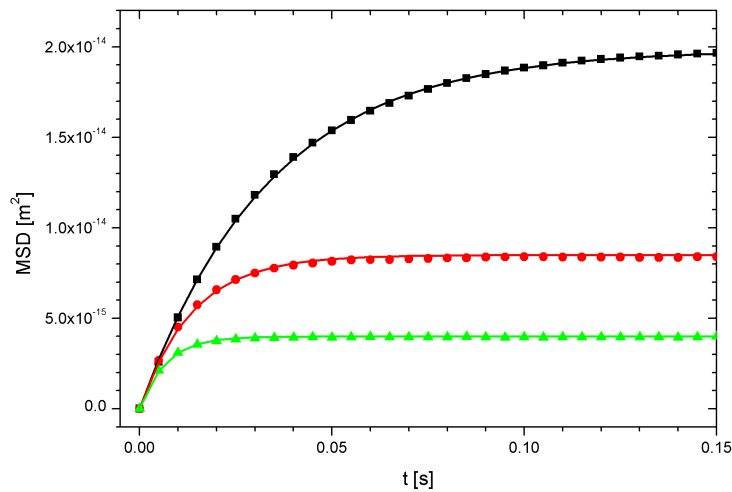


FIGURE 5.6: Mean square displacement (MSD) of a trapped bead in water as a function of lag time, shown for three traps with different stiffness: weak ($k = 0.81 \times 10^{-6}$ N/m, black squares), medium ($k = 2.0 \times 10^{-6}$ N/m, red circles) and strong trap ($k = 4.0 \times 10^{-6}$ N/m, green triangles). The data points are fitted with Eq. (5.27).

To avoid potential numerical artifacts due to the Laplace transforms in (6.20), we used analytical expressions for MSDs of probe particles. Mean square displacement of a trapped particle in viscous media can be described by

$$\langle r^2(t) \rangle = r_p^2(1 - e^{-t/\tau}), \quad (5.27)$$

where r_p is a plateau value of MSD and τ is position autocorrelation decay time. In Fig. 5.6 we show the MSDs of a $3.22 \mu\text{m}$ probe bead in water, confined in weak ($k = 0.81 \times 10^{-6}$ N/m), medium ($k = 2.0 \times 10^{-6}$ N/m) and strong ($k = 4.0 \times 10^{-6}$ N/m) optical trap. The measured MSDs can be fitted with (5.27), yielding τ of 0.034 s, 0.014 s and 0.0067 s, respectively. If (6.20) is combined with (5.27), the complex shear modulus reads

$$G(\omega) = \frac{2k_B T(1 + i\omega\tau)}{3\pi a r_p^2}. \quad (5.28)$$

¹The temperature of samples was not controlled. An estimate is $23 \pm 3^\circ\text{C}$. The viscosity of water is $\eta = 10.0 \times 10^{-4}$ Pas at $T = 20^\circ\text{C}$ and $\eta = 8.9 \times 10^{-4}$ Pas at $T = 25^\circ\text{C}$

The non-zero real component of the shear modulus is a result of trap confinement $G'_0 = 2k_B T / 3\pi a r_p^2 = k / 6\pi\alpha$, while the imaginary component reveals $G''(\omega) = -2k_B T \omega \tau / 3\pi a r_p^2 = -\omega\eta$ the viscosity of the medium. The resulting viscosities obtained with traps of different stiffnesses were $\eta = 9.1 \times 10^{-4}$ Pas, 8.7×10^{-4} Pas and 9.1×10^{-4} Pas, respectively. The values, obtained with this procedure, are even closer to the true value of water viscosity.

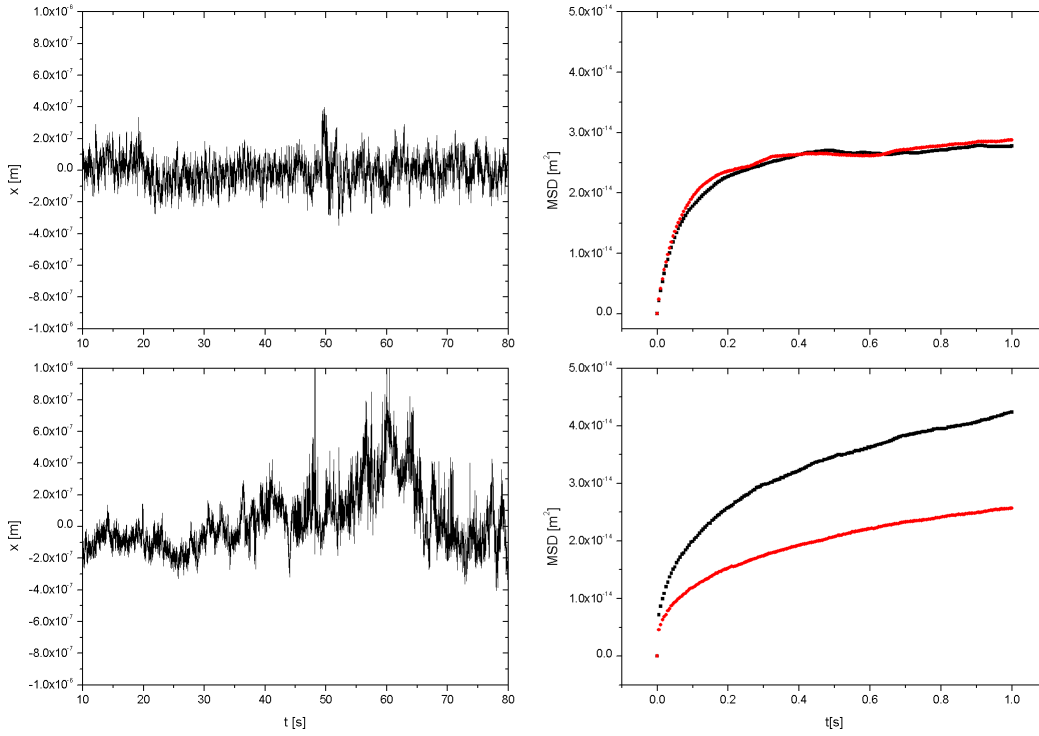


FIGURE 5.7: Comparison of trajectory $x(t)$ and resulting MSD of a trapped bead in mature bacterial solution for two trap stiffnesses. The upper row shows a typical $x(t)$ and $\text{MSD}(t)$ in a weak trap (MSDs for two different $3.22 \mu\text{m}$ beads are shown for comparison), whereas the lower row shows the same results, obtained in five times stiffer trap. The trajectory $x(t)$ of a bead in the stiff trap has artifacts caused by surrounding bacteria and debris that is pulled into the trap.

The same procedure was used to determine the viscosity of bacterial samples. In Fig. 5.7 we present probe particle's trajectories and the resulting MSDs during measurement of the sample 3, which contained dense extracellular matrix and a lot of bacterial cells. The results obtained with a weak optical trap are correct: the trajectory $x(t)$ reveals Brownian nature of position fluctuations, the MSDs of two different particles are overlapping and reach the plateau value in 0.2 s. In contrast, the trajectory of the probe confined in a strong optical trap reveals sudden rapid changes of a probe position. As a result, MSDs of different probe particles do not overlap and do not reach a meaningful plateau value. The reason for this artifacts could be surrounding bacteria that were pulled into the strong optical trap. The accumulated bacteria worsened the particle tracking precision and made the

three dimensional trapping weaker. The average position of the probe bead was not anymore in the center of the trap, but rather the average position of the bead and bacteria together were in the trap center. Effectively the average position of the bead was slowly diffusing around the trap center which resulted in "false" trajectories and overestimated MSDs. To avoid the accumulation of bacteria around the probe particle the stiffness of the trap had to be kept as low as possible.

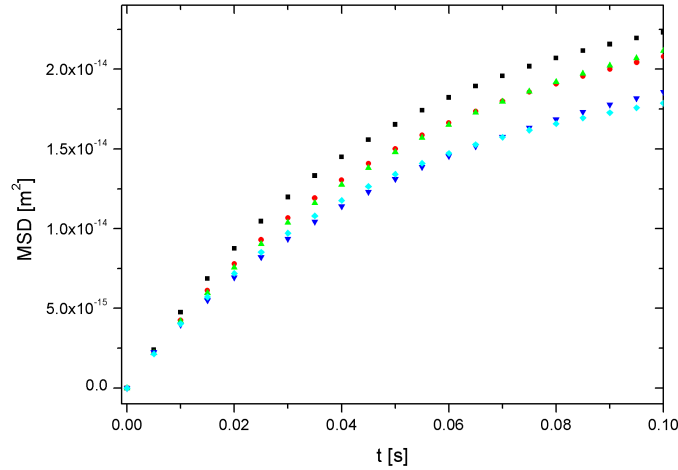


FIGURE 5.8: MSD as a function of lag time t for aging bacterial network. Growth medium (black squares), sample 1 (red circles), sample 2 (green triangles), sample 3 (blue inverted triangles), sample 3 without bacteria (cyan diamonds). MSD data was fitted with (5.27), then (5.28) was used to yield viscosities $\eta_M = 10.0 \times 10^{-4}$ Pas, $\eta_{S1} = 12.4 \times 10^{-4}$ Pas, $\eta_{S2} = 14.4 \times 10^{-4}$ Pas, $\eta_{S3} = 16.0 \times 10^{-4}$ Pas and $\eta_{S3'} = 13.8 \times 10^{-4}$ Pas.

The MSD of a weakly trapped bead in bacterial networks of different age are presented in Fig. 5.8. As a control we measured the rheology of the growth medium, which has similar viscosity as water and therefore the fastest relaxation towards plateau value in MSD. The measured MSDs in different bacterial samples were fitted with (5.27) to extract their relaxation times τ and plateau values r_p . These values were used in (5.28) to yield the viscosity of the growth medium ($\eta_M = 10.0 \times 10^{-4}$ Pas), samples 1, 2, 3 ($\eta_{S1} = 12.4 \times 10^{-4}$ Pas, $\eta_{S2} = 14.4 \times 10^{-4}$ Pas, $\eta_{S3} = 16.0 \times 10^{-4}$ Pas) and "mesh-only" sample ($\eta_{S3'} = 13.8 \times 10^{-4}$ Pas).

5.3.2 One-particle active MR

In one-particle active MR experiment the optical trap was sinusoidally oscillated with a fixed amplitude $A = 1 \mu\text{m}$ and frequency f while the video of a trapped probe bead was recorded. The measurement was repeated at frequencies ranging from $f = 0.1$ Hz to 50 Hz. Once when the bead trajectory $x(t)$ was recovered from the video, the amplitude $D(\omega)$ of bead oscillation was determined from the power spectral density $S_x(\omega)$. The phase lag δ of the bead with respect to the optical trap was obtained by fitting of sinusoidal response $x_B(t) = D(\omega) \sin(\omega t - \delta(\omega))$ to the bead trajectory. The phase lag δ and the ratio D/A for one-particle active MR in water

are shown in Fig. 5.9. The responses $D(\omega)/A$ and $\delta(\omega)$ of the probe particle to the oscillating trap movement are in a good agreement with the theoretical predictions, given by (5.16) and (5.17). Their fits to the measured data points yielded viscosity of water between $\eta = 8.8 \times 10^{-4}$ and $\eta = 9.6 \times 10^{-4}$ Pas.

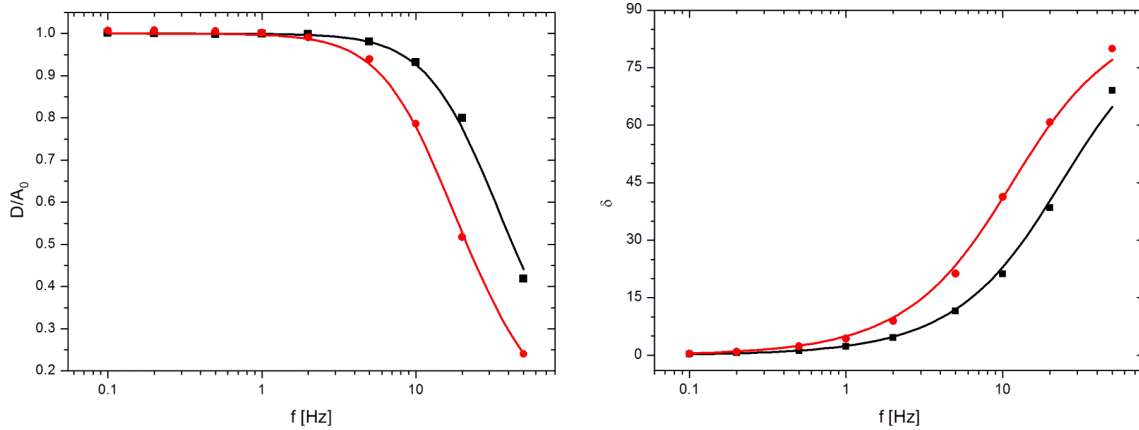


FIGURE 5.9: One-particle active MR in water. *Left:* The ratio between bead amplitude and trap amplitude D_0/A as a function of trap oscillation frequency f . Black points represent the measurements with stiff trap ($k = 4.0 \times 10^{-6}$ N/m), red points are obtained with weaker trap ($k = 2.1 \times 10^{-6}$ N/m). The data points are fitted with (5.16) with η as a free parameter, yielding $\eta = 8.8 \times 10^{-4}$ Pas and $\eta = 8.9 \times 10^{-4}$ Pas, respectively. *Right:* Phase lag δ of the probe bead with respect to the optical trap as a function of frequency. The data points are fitted with (5.17), yielding $\eta = 8.8 \times 10^{-4}$ Pas and $\eta = 9.6 \times 10^{-4}$ Pas, respectively.

The complex viscoelastic modulus $G(\omega)$ can be calculated from the measured $D(\omega)$ and $\delta(\omega)$ using equations (6.23). In right chart of Fig. 5.10 we show a comparison between apparent storage moduli of water $G'(\omega)$, measured with optical traps of different stiffnesses. The non-zero values of G' are solely due to the elastic confinement of a probe particle in the optical trap. To account for the trap stiffness the constant $G'_T = 6\pi ak$ has to be subtracted to get the real storage modulus of the medium. These results, which are presented in right chart of the same figure, reveal that the method accurately determines zero value of elastic modulus at low frequencies, whereas at high frequencies ($\omega > 100/s$) there is an error offset of -0.02 Pa. A possible cause for this error could be a large amplitude of the optical trap oscillation. At high frequencies the trapped bead couldn't follow the trap, its amplitude was approximately $0.4 \mu\text{m}$. The displacement of the bead from the center of the optical trap was in some parts of the oscillation cycle larger than 300 nm (the range of parabolic trapping potential). The equation (5.14) in such case does not hold anymore which explains the observed deviation of G' from zero.

The measured loss modulus $G''(\omega)$ of water is shown in Fig. 5.11. Two data series obtained with optical traps of different stiffnesses collapse onto a linear function $G''(\omega) = \eta\omega$ with $\eta = 9.1 \times 10^{-4}$ Pas, which is remarkably close to the real viscosity of water $\eta = 9.3 \times 10^{-4}$.

One-particle active MR was then employed to monitor the viscoelastic properties

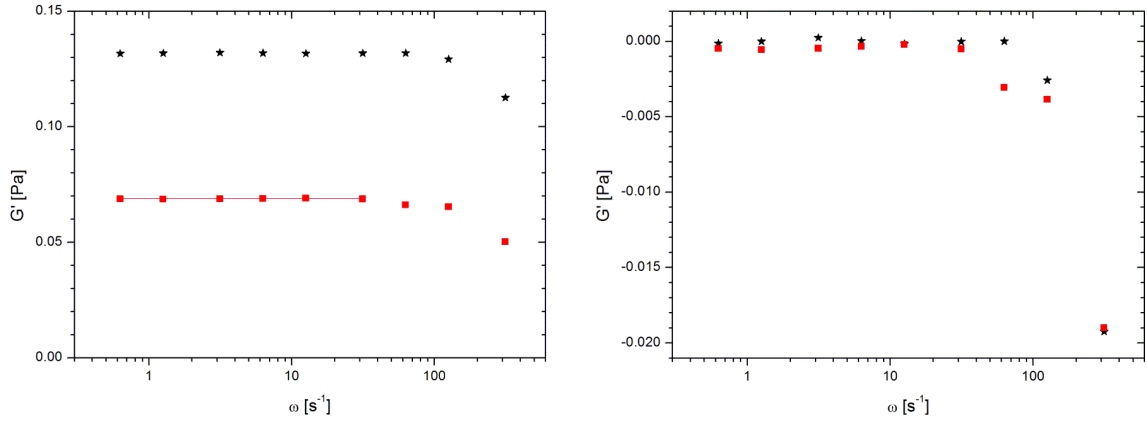


FIGURE 5.10: One-particle active MR in water. *Left:* Apparent storage modulus G' in water as a function of angular frequency. Black stars represent the measurements with a strong trap ($k = 4.0 \times 10^{-6}$ N/m), whereas red squares are obtained with weak trap ($k = 2.1 \times 10^{-6}$ N/m). The constant $G' = 0.069$ Pa (red line) is consistent with trap stiffness $k = G'/(6\pi a) = 2.1 \times 10^{-6}$ N/m. *Right:* True storage modulus $G'(\omega)$ of water.

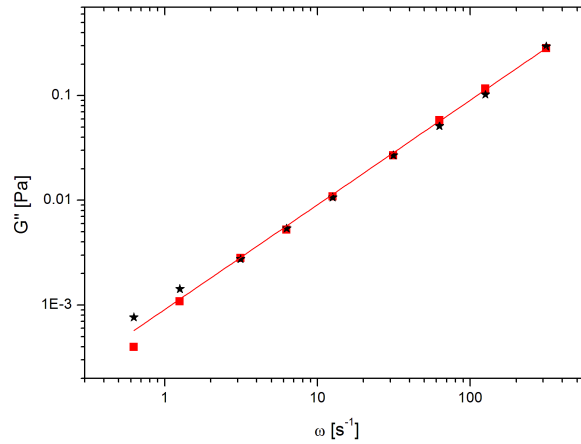


FIGURE 5.11: Absolute value of the loss modulus G'' of water as a function of angular frequency ω , measured with one-particle active MR. Black stars represent the measurements with stiff trap ($k = 4.0 \times 10^{-6}$ N/m), whereas red squares are obtained with weak trap of ($k = 2.1 \times 10^{-6}$ N/m). The data points obtained with weaker trap are fitted with linear function yielding $\eta = 9.1 \times 10^{-4}$ Pas.

of the growing bacterial suspension. Fig. 5.12, where frequency dependent loss modulus of aging suspension is presented, is one of the central results of this Chapter. The measured values of $G''(\omega)$ of different samples were fitted with linear function to extract their viscosities. The viscosity of the growth medium $\eta_M = 12.4 \pm 0.1 \times 10^{-4}$ Pas was a bit higher than that of water, which is a reasonable result, since the medium contains some salts and 0.4% glucose. Viscosities of samples 1, 2 and 3 were found to be $\eta_{S1} = 14.1 \pm 0.1 \times 10^{-4}$ Pas, $\eta_{S2} = 20.1 \pm 0.3 \times 10^{-4}$ Pas and $\eta_{S3} = 35.4 \pm 1.2 \times 10^{-4}$ Pas, respectively, whereas viscosity of sample 3 without bacteria was $\eta_{S3'} = 24.5 \pm 0.4 \times 10^{-4}$ Pas.

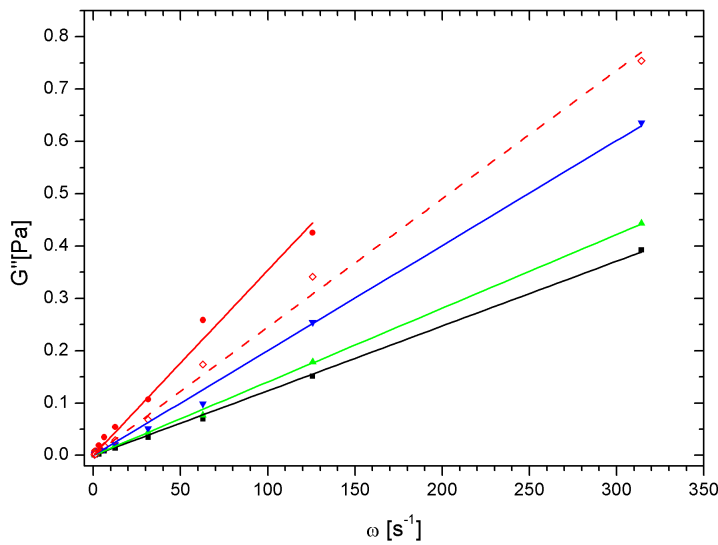


FIGURE 5.12: Absolute value of the loss modulus G'' of growing bacterial suspension as a function of angular frequency, measured with one-particle active MR. Measured values are fitted with imaginary part of (5.25), yielding viscosities of growth medium (black squares): $\eta_M = 12.4 \pm 0.1 \times 10^{-4}$ Pas, sample 1 (green triangles): $\eta_{S1} = 14.1 \pm 0.1 \times 10^{-4}$ Pas, sample 2 (blue inverted triangles): $\eta_{S2} = 20.1 \pm 0.3 \times 10^{-4}$ Pas, sample 3 (red circles): $\eta_{S3} = 35.4 \pm 1.2 \times 10^{-4}$ Pas, sample 3 without bacteria (red diamonds): $\eta_{S3'} = 24.5 \pm 0.4 \times 10^{-4}$ Pas.

The frequency dependence of the true elastic modulus of the growing bacterial suspension measured with one-particle active MR is presented in Fig. 5.13. The modulus $G'(\omega)$ of the growth medium has same frequency response as that of water - zero stiffness at low frequencies and artifacts at $\omega > 30/s$. The measured values of the elastic modulus of bacterial samples are scattered but still some conclusions can be made. $G'(\omega)$ of the bacterial solution is increasing with frequency from zero at low frequencies to around 0.01 Pa at high frequencies. The differences between measured moduli at high and low frequencies $\Delta G' = G'(60/s) - G'(0.6/s)$ are 0.013 Pa for sample 1, 0.016 Pa for sample 2 and 0.023 Pa for sample 3. The corresponding stiffnesses of the medium $k_m = 6\pi a \Delta G'$ are then 3.9×10^{-7} N/m, 4.8×10^{-7} N/m and 7.1×10^{-7} N/m.

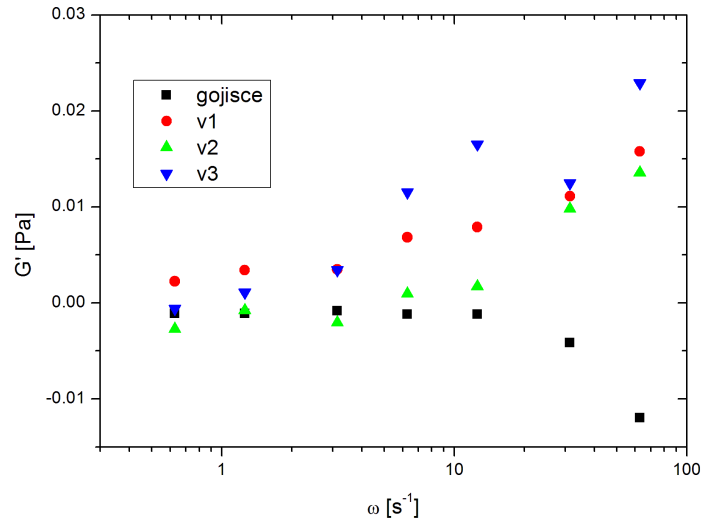


FIGURE 5.13: Elastic modulus G' of bacterial suspensions as a function of angular frequency, measured with one-particle active MR.

5.3.3 Two-particle active MR

As the last and the most complex, the results of two-particle active MR are presented. In two-particle active MR two optical traps are employed to hold two particles. The first trap is stiff and is used to exert an oscillating force on a drive particle, whereas in the second trap a probe particle that serves as a deformation monitor is weakly trapped. A typical set of trajectories recorded in water at trap oscillation frequency $f = 10$ Hz is shown in Fig. 5.14. The oscillating optical trap is used as a reference, the drive bead has slightly lower amplitude and lags behind the trap, whereas the probe bead has small amplitude but its phase is in the front of the trap. The frequency dependence of the amplitude and phase of both beads in the experiment where the drive bead was oscillated in the direction of the line connecting the beads are presented in Fig. 5.15.

The amplitude and the phase dependence of the second bead were used to calculate the complex response functions using (5.22). The real and the imaginary part of parallel $A_{\parallel}(\omega)$ and perpendicular $A_{\perp}(\omega)$ response functions are displayed in Fig. 5.16. Rather complicated expressions for the theoretical real and imaginary part of the response functions with two free parameters, the viscosity of the medium η and its stiffness k_m were fitted to the measured data. The theoretical response functions are in a good agreement with measured points except in the low frequency region where the errors occur due to the low signal-to-noise ratio. Since water is purely viscous medium the low frequency oscillation of the drive trap results in a very small deformation of the medium at the location of the probe bead and therefore the determination of its amplitude and phase has a large relative error. Nevertheless, the measured $A_{\parallel}(\omega)$ and $A_{\perp}(\omega)$ are best fitted with $k_m = 0$ and $\eta = 9.1 \times 10^{-4}$ Pas and $\eta = 9.2 \times 10^{-4}$ Pas, respectively. These values are within 5% of true viscosity

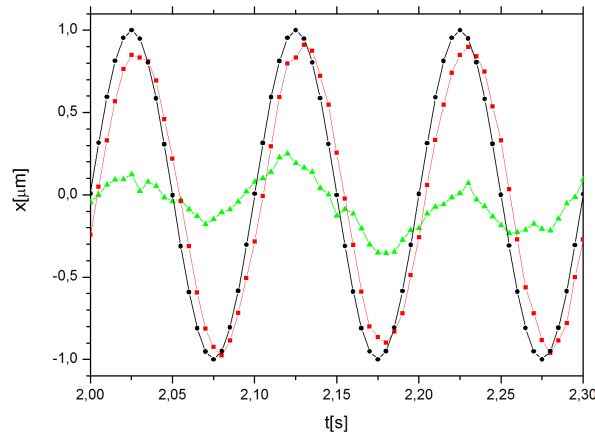


FIGURE 5.14: Part of the trajectories of the drive trap x_0 (black), the drive bead x_1 (red squares) and the probe bead x_2 (green triangles) in a two-particle active MR measurement in water at the trap oscillation frequency $f = 10$ Hz and amplitude $A = 1 \mu\text{m}$.

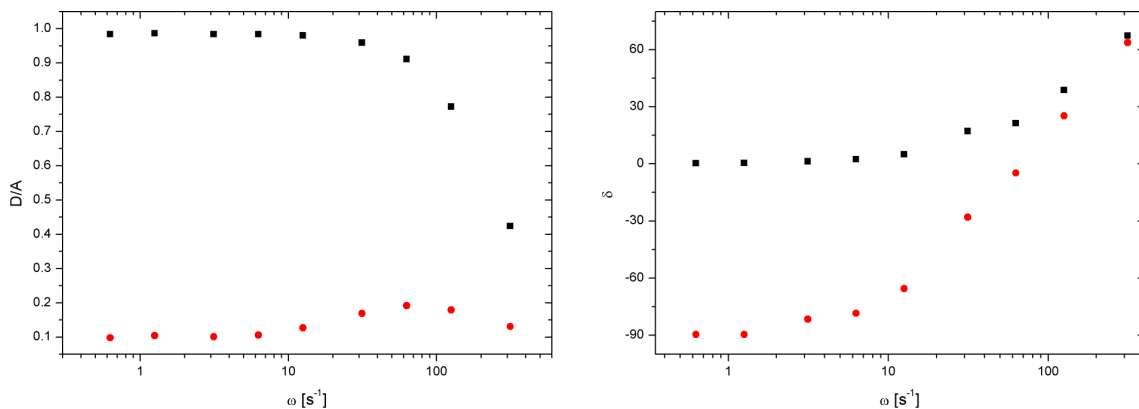


FIGURE 5.15: Active two-particle MR in water. Amplitudes D/A (left) and phase lags δ (right) of the drive bead (black squares) and the probe bead (red circles) as a function of trap oscillation frequency.

of water.

After its demonstration in water, two-particle active MR was used to determine viscoelasticity of the bacterial network. The real and the imaginary part of the perpendicular two-particle response function of the aging bacterial solution, presented in Fig. 5.17, are the second key result of this Chapter. The measured values have been fitted with (5.22) with three adjustable parameters, viscosity η , stiffness k_m of the medium and a scaling factor. Although the trap powers were kept constant in different samples, the measured two-particle responses $A_{\parallel}(\omega)$ and $A_{\perp}(\omega)$ have different magnitudes from sample to sample and the additional linear scaling factor had to be introduced in (5.22) to successfully fit the data. The scaling coefficient does not influence the values of viscosity and stiffness, since the viscosity of a solution is defined by the position of a peak of the real component of the response function

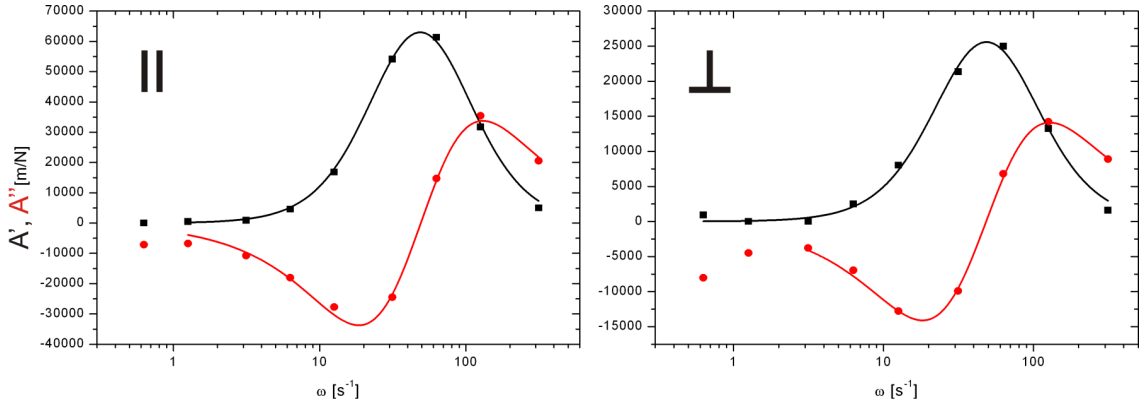


FIGURE 5.16: Real (black squares) and imaginary part (red circles) of apparent two-particle response functions in water. Parallel $A_{||}$ (left) and perpendicular A_{\perp} (right) response functions. The fits of Eq. (5.22) to data points of $A_{||}$ yield $\eta = 9.1 \times 10^{-4}$ Pas and $\eta = 9.2 \times 10^{-4}$ Pas for A_{\perp} (solid curves).

(higher viscosity shifts the peak to lower frequencies), while the stiffness is revealed by the low frequency behavior of the response function.

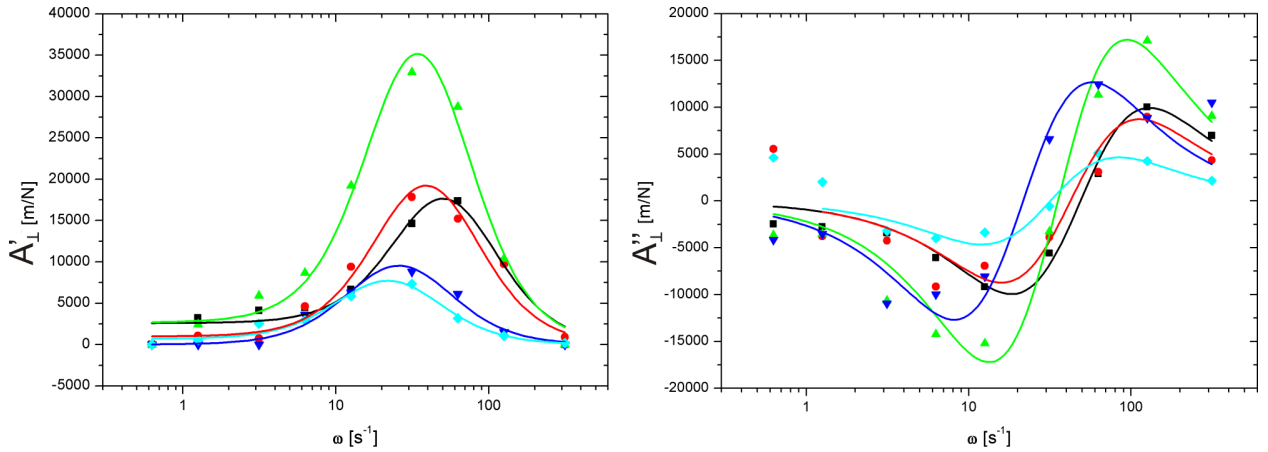


FIGURE 5.17: Real (left) and imaginary (right) part of the apparent two-particle perpendicular response function. Data is shown for the growth medium (black squares), sample 1 (red circles), sample 2 (green triangles), sample 3 (blue inverted diamonds) and sample 3 with bacteria removed (cyan diamonds). Solid lines are the theoretical curves (5.22) with three adjustable parameters: η , k_m and scaling coefficient.

The measured values of the real part of two-particle complex response functions are in a good agreement with the theoretical response given by linearly scaled (5.22), whereas the measured imaginary parts of the response are only in qualitative agreement. The viscosities and stiffnesses of the investigated bacterial samples, obtained from various two-particle response functions, are presented in the following table.

Obtained from:	A'_{\perp}	A''_{\perp}	A'_{\parallel}	A'_{\perp}	A'_{\parallel}
Sample	$\eta[10^{-4} \text{ Pas}]$	$\eta[10^{-4} \text{ Pas}]$	$\eta[10^{-4} \text{ Pas}]$	$\mathbf{k}_m[10^{-8} \text{ N/m}]$	$\mathbf{k}_m[10^{-8} \text{ N/m}]$
G. medium	14.7	14.5	14.9	15	0
Sample 1	18.4	16.7	17.2	4.9	9.4
Sample 2	21.1	19.9	21.8	7.4	9.8
Sample 3	33.1	32.7	34	8.8	10
Mesh-only	27.3	22.2	25	0	7.4

5.4 Conclusion and outlook

We used optical tweezers and high resolution video particle tracking to measure the microrheology of the bacterial extracellular matrix, produced by *Vibrio* sp. The investigated samples were probed with three different MR techniques. The simplest was passive one-particle MR, where thermal fluctuations of $3.22 \mu\text{m}$ silica bead, trapped in a weak optical trap, were recorded to calculate the complex viscoelastic modulus of the medium. In active one-particle MR, viscoelastic properties were extracted from the response of a probe particle to a harmonically oscillating optical trap. For two-particle active MR two optical traps were employed. One was used to sinusoidally oscillate one bead, whereas another, weaker trap, was holding the probe bead. The rheological properties of the samples were calculated from the response of the probe bead to the oscillations of the trap.

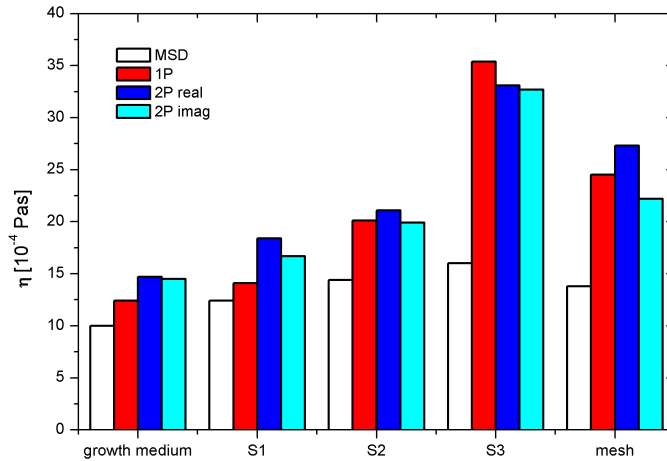


FIGURE 5.18: Comparison of measured viscosity η of various samples with one-particle passive MR (MSD, white), one-particle active MR (red) and two-particle active MR (blue - real part, cyan - imaginary part of two-particle response function).

All MR techniques were first tested on water, where the measured viscosities ranged from $8.7 \times 10^{-4} \text{ Pas}$ to $10.8 \times 10^{-4} \text{ Pas}$. The true value of the viscosity of water in room temperature region varies from $8.9 - 10.0 \times 10^{-4} \text{ Pas}$, therefore the maximum error was less than 10%. The most accurate results were obtained with active MR - the error of two-particle active MR was less than 5%.

After the successful demonstration in water, the techniques were used for monitoring the viscoelastic modulus of the growing bacterial population. Samples of the solution in the lag, log and stationary phase of the growth curve were analyzed using the MR techniques and the summarized results are presented in Fig. 5.18.

One-particle passive MR detected the increasing viscosity of the aging bacterial solution, but the values seem to be highly underestimated. The viscosities obtained with the active techniques are in a good agreement - the values in each sample are within $\pm 10\%$ of the average value. The viscosity of the "mesh-only" sample (sample 3 with bacteria removed by spinning) was found to be 25% lower than the viscosity of the sample 3, which is reasonable since spinning removes bacteria and cellular debris and therefore lowers the density of the solution.

The conclusion about the storage modulus G' of the extracellular matrix is not completely clear. The storage moduli, measured with one-particle active MR, were on the order of 0.01 Pa, which equivalents to the medium stiffness $k_m \approx 3 \times 10^{-7}$ N/m. The stiffnesses, found with two-particle MR, had highly scattered values and were on the order of $k_m \approx 5 \times 10^{-8}$ N/m. The stiffness of bacterial samples was definitely far below the stiffness of the optical traps ($k \approx 2 \times 10^{-6}$ N/m) that were used in the experiments.

We demonstrated the use of optical tweezers microrheology to probe the viscoelastic modulus of a complex biological sample. The best results were obtained with the active MR techniques. The experimental setup will be used to perform more detailed measurements of bacterial cultures and to study the influence of various environmental parameters on the rheological properties of the bacterial network.

Conclusion

This thesis presents experimental studies in three subfields of condensed soft matter, namely interparticle potentials in nematic colloids, self-ordering of colloidal particles into complex structures under the influence of external magnetic field and the rheology of a developing biological system. Magneto-optical tweezers, a new micro-manipulation tool with combined advantages of optical tweezers and homogenous magnetic tweezers, were used to perform experiments that would be otherwise hardly feasible.

★

The first part of the thesis deals with interparticle forces between colloidal particles in a confined nematic liquid crystal (LC). The tangential anchoring of LC molecules on the particles induced defects with quadrupolar symmetry which resulted in a repulsive force between the particles. Static experiments, where the LC-mediated repulsion was balanced by attractive magnetic force, enabled precise measurement of the interparticle force over four orders of magnitude. This was the first accurate measurement of the force at particle center-to-center separations as small as $1.1 \times$ particle diameter. The $1/r^6$ force dependence, predicted by theoretical calculations, was confirmed on wide interparticle separation range. In dynamic measurements, where the LC-mediated force was obtained from the velocities of particles drifting apart, we determined the same separation dependence of the force. This confirms that the effective drag coefficient $\gamma = F_{LC}/v$ is independent on interparticle separation. The force was found to be temperature dependent, $F \propto (T_{NI} - T)^\beta$ with $\beta = 0.40$ when approaching the nematic-isotropic transition temperature T_{NI} .

We also experimentally confirmed that the interaction between colloidal particles in a confined NLC is different from that in bulk. We demonstrated that at small separations, the interparticle potential follows the power-law dependence, whereas at large separations the potential decreases exponentially with the characteristic decay length proportional to the sample thickness. The observed crossover in the potential occurs at particle separation that is comparable to the sample thickness. This double-regime behavior and reduction of the long range of the potential has to be considered when designing new colloidal structures.

★ ★

The central part of the thesis is focused on an experimental study of the relationship between the isotropic interparticle interactions and the formation of ordered structures in a system of superparamagnetic colloidal particles. The interaction was induced by the external magnetic field and controlled by the spatial constraints. In the quasi two-dimensional system with a hard core/softened repulsive interaction several self-assembled mesophases were formed depending on the volume filling fraction. We observed the square, hexagonal and honeycomb lattices as well as the labyrinthine structure. This was the first experimental validation of theoretical predictions related to such interparticle interaction.

More complex interparticle potentials were realized by the precession of the magnetic field on a surface of a cone. By variation of the cone opening angle we were able to tune the ratio between dipolar repulsion and attraction. At the magic opening angle the dipolar interaction should have vanished, but we observed the attraction between particles. Numerical calculations showed that the attraction arises due to the effects of the local magnetic fields and follows $1/r^6$ separation dependence.

The "magic angle" colloidal system showed pronounced many-body effect, i.e. the interaction energy of many particles doesn't equal to the sum of all pair energies. The isotropic attractive pair potential and the pair-wise non-additivity of the interaction promote the formation of colloidal pairs from single particles, the growth of longer chains out of particle pairs and larger hexagonal close-packed colloidal sheets from small planar clusters. If the volume filling fraction is high enough, 3D colloidal crystals grow from small crystallites. The experiment revealed that two dimensional colloidal sheets are the most energetically favorable structures. This was also confirmed by numerical calculations.

We demonstrated that in the "magic angle" system colloidal particles can be assembled into stable two dimensional superstructures. The system can be therefore used to study the interactions between them, e.g. crystallization and coalescence of vesicles or more complicated structures could be modeled with (decorated) colloidal rings.

More complex interparticle interactions could be engineered by the addition of other external fields. The use of charged beads and consequently $1/r^3$ electrostatic interparticle repulsion would be a simple upgrade of the system. More complex examples include the use of anisotropic solvent (liquid crystals) or different background potentials, such as patterned substrates or light induced potentials.

* * *

The last part of the thesis reports the recent work on laser tweezers microrheology (MR) of soft matter. Using optical tweezers and high resolution video particle tracking we set up a system for microrheological measurements and used it to measure the microrheology of the extracellular matrix of bacteria *Vibrio* sp. The investigated samples were probed with one-particle passive microrheology (MR), one-particle active MR and two-particle active MR. All MR techniques were first tested on water, where the measured viscosities ranged from 8.7×10^{-4} Pas to 10.8×10^{-4} Pas. The most accurate results were obtained with active MR - the error of two-particle active MR was less than 5%.

The techniques were used to measure the viscoelastic modulus of the extracellular matrix in the lag, log and stationary phase of the bacterial growth. One-particle passive MR turned out to be the least accurate and convenient method to probe the rheology of complex biological samples, since the obtained loss moduli of the samples were underestimated. The results obtained with the active techniques are in a good agreement - the viscosities, measured with both techniques, are within $\pm 10\%$ of the average value. We discovered that the viscosity of the extracellular matrix of growing bacterial population changes with time and reaches a maximum of approximately $\eta \approx 3.3 \times 10^{-3}$ Pas in the stationary phase of the growth.

The storage modulus G' of the investigated extracellular matrix was found to be very small. One-particle active MR measurements showed that G' increases with the age of bacterial solution and is on the order of 0.01 Pa. The values of G' , obtained in two-particle MR, were scattered around the average value of 0.001 Pa. The storage modulus of all bacterial samples was definitely at least order of magnitude lower than the apparent storage modulus of optical trap used in the experiment, which was 0.06 Pa.

The experimental setup together with analyzing routines will be in future used by biologists to perform more detailed analysis of microrheology of growing bacterial cultures and to study the influence of various environmental parameters on the rheology of the extracellular matrix.

~

In conclusion, magneto-optical tweezers turned out to be a powerful tool in studies of soft matter. They are convenient method to manipulate micron-sized particles and to precisely exert and measure forces in subpico- to nanonewton range. Moreover, time-varying magnetic field enables creation of complex interparticle potentials which lead to novel self-assembled structures.

Numerical calculation of interaction energy of N particles

We are considering a system of $N - 1$ superparamagnetic particles of diameter σ and susceptibility χ in external magnetic field \mathbf{B}_0 located at positions \mathbf{r}_i . Let us assume that we already know all the magnetic dipole moments \mathbf{m}_i of particles. When N -th particle is added, the local magnetic field at the position \mathbf{r}_N is the sum of external field \mathbf{B}_0 and fields \mathbf{B}_j , created by magnetic dipole moments of other particles (2.11)

$$\mathbf{B}(\mathbf{r}_N) = \mathbf{B}_0 + \sum_j \mathbf{B}_j(\mathbf{r}_i). \quad (\text{A.1})$$

Due to this field, a magnetic dipole moment is induced in the particle

$$\mathbf{m}_i = \frac{4\pi\sigma^3\chi}{24\mu_0} \mathbf{B}(\mathbf{r}_i). \quad (\text{A.2})$$

This magnetization is a source of the magnetic field \mathbf{B}_N which, naively looking, triggers a series of events. The addition of \mathbf{B}_N alters local magnetic fields at position of other particles, therefore their induced magnetic dipole moment \mathbf{m}_i and the resulting field \mathbf{B}_i are altered. This changes the local field at position of the N -th particle and so on... The whole cycle of computation has to be repeated all over again and again until the magnetic moments and local magnetic fields converge.

In order to obtain the energy of the system, we used following iterative algorithm

1. Initialize all the magnetic moments \mathbf{m}_i by making them proportional to the external field (A.2)
2. For all the locations of the particles, update the magnetic field with contributions from other particles

$$\mathbf{B}(\mathbf{r}_i) = \mathbf{B}_0 + \sum_{j \neq i} \mathbf{B}_j(\mathbf{r}_i) \quad (\text{A.3})$$

3. Calculate new magnetic moments using updated fields

$$\mathbf{m}_i = \frac{4\pi\sigma^3\chi}{24\mu_0}\mathbf{B}(\mathbf{r}_i). \quad (\text{A.4})$$

4. If not yet converged, return to 2.

5. Calculate energy as

$$E = -\frac{1}{2}\sum_i \mathbf{m}_i\mathbf{B}(\mathbf{r}_i) \quad (\text{A.5})$$

If the magnetic field is not static, the energies for all orientations of the field in one cycle have to be obtained using the upper procedure and then averaged. For example, in the case of the in-plane rotating field $\mathbf{B}_0 = B_0(\cos \phi, \sin \phi, 0)$ with $\phi = \omega t$ the energy is typically averaged over 8 different field directions, namely $\phi = 0, \pi/4, 2\pi/4 \dots 7\pi/4$.

Simulation of 2D particle structures

Once the calculation of the magnetic energy for any spatial configuration of particles is available, it is just a small step to a simple Brownian dynamics simulation of the system. The forces acting on each particle can be calculated as gradients of energy in x, y and z directions. The effect of thermal fluctuations are included with the addition of appropriate noise to movements of particles. One iteration of simulation loop is outlined below:

1. Randomly pick a particle i that hasn't been selected yet in this iteration.
2. Calculate forces acting on the particle by derivation of the energy with the position of the particle slightly changed. For reasons of brevity, the procedure for movement in x direction only will be presented:

$$F_{ix}(t) = \frac{E(x_i + \epsilon) - E(x_i - \epsilon)}{2\epsilon} \quad (\text{A.6})$$

3. Try to move the particle according to

$$x_i(t + \Delta t) = x_i(t) + \frac{F_{ix}(t)}{\gamma}\Delta t + r(t), \quad (\text{A.7})$$

where Δt is time step, γ the viscous drag coefficient of the particle and $r(t)$ random noise with average $\langle r(t) \rangle = 0$. In the simulation $r(t)$ is a random number chosen from Gaussian distribution with variance $2k_B T \Delta t / \gamma$.

Reject the movement if the new location of the particle is in the excluded volume of other particles or outside the simulation box.

4. If not all particles have been selected yet, return to 1.

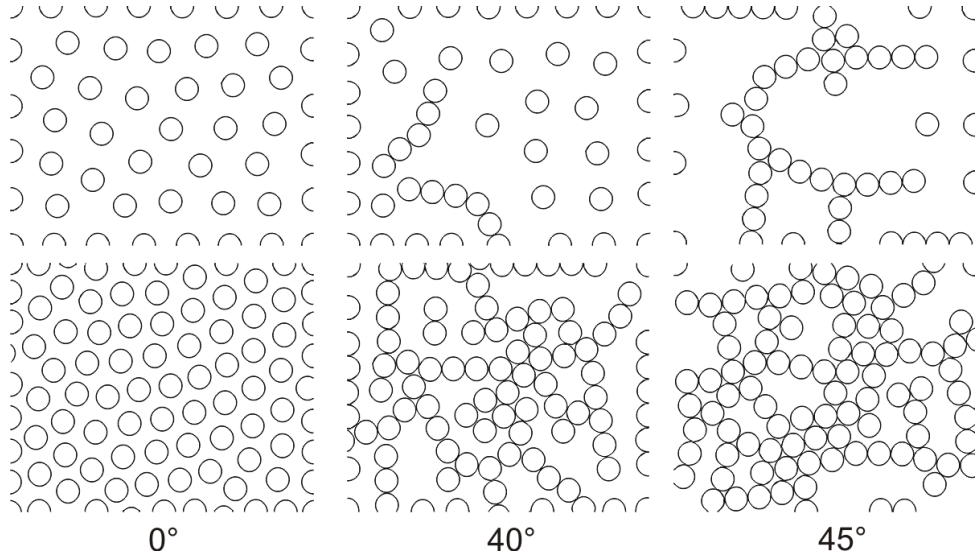


FIGURE A.1: Simulation snapshots of the 2D system for different angles θ_p of magnetic field rotation. The system in the upper row has 50 particles (filling fraction $\eta = 0.30$), the system in the lower row 96 particles ($\eta = 0.58$).

Simulations of the 2D system with two different filling fractions, $\eta = 0.30$ and $\eta = 0.58$, were performed. The resulting structures shown in Fig. A.1 are similar to experimentally observed mesophases. If the field is vertical to the plane of the particles, $\theta = 0^\circ$, the dipolar repulsion forces the particles into hexagonal arrangement. With the opening of the field cone, the dipolar repulsion is weakened, but at $\theta = 30^\circ$ still strong enough to sustain hexagonal ordering. At even higher cone opening angle, $\theta = 40^\circ$, the effects of the local fields overcome dipolar repulsion. The interaction is not a sum of dipolar pair interactions. The many-body effect induces the formation of single chains as preferred structures. Increased opening angle $\theta = 45^\circ$ results in single cross-linked chains in the system with low filling fraction, whereas in the dense system the chains merge into 2D sheets.

Appendix B

Calculation of pair energy

In this Appendix a calculation of the interaction energy of two superparamagnetic particles in a magnetic field is presented. The external magnetic field is precessing on a surface of a cone with the opening angle θ_p ,

$$\mathbf{B}_0 = B_0(\sin \theta_p \cos \phi, \sin \theta_p \sin \phi, \cos \theta_p) \quad (\text{B.1})$$

with $\phi = \omega t$.

The energy of a system of induced dipoles in general is $E = -\frac{1}{2} \sum_i \mathbf{m}_i \cdot \mathbf{B}(\mathbf{r}_i)$, where \mathbf{r}_i are the locations of the particles with volume V , magnetic susceptibility χ and $\mathbf{m}_i = \frac{\chi V}{\mu_0} \mathbf{B}(\mathbf{r}_i)$ are the induced magnetic moments which are proportional to the magnetic field "felt" by each particle. For a system of two particles with the same susceptibility, where the first particle is located at the origin of the coordinate system and the second at \mathbf{r} , the last equation simplifies to

$$E = -\frac{1}{2} \mathbf{m} \cdot \mathbf{B}, \quad (\text{B.2})$$

since the particles are interchangeable so both the moments $\mathbf{m}_1 = \mathbf{m}_2 = \mathbf{m}$ and the magnetic fields $\mathbf{B}(\mathbf{0}) = \mathbf{B}(\mathbf{r}) = \mathbf{B}$ are the same. The magnetic field \mathbf{B} is a sum of the external magnetic field \mathbf{B}_0 and the correction $\Delta \mathbf{B}$ due to the field of the other particle:

$$\mathbf{B}(\mathbf{r}) = \mathbf{B}_0 + \Delta \mathbf{B} \quad (\text{B.3})$$

The second term is given by $\Delta \mathbf{B} = \frac{\mu_0}{4\pi} \frac{3(\mathbf{m}\hat{\mathbf{r}})\hat{\mathbf{r}} - \mathbf{m}}{r^3}$, where $\hat{\mathbf{r}} = \mathbf{r}/|\mathbf{r}| = (\sin \theta, \mathbf{0}, \cos \theta)$ is the direction of the vector connecting both particles. Also each induced magnetic moment is a sum of two components: the major contribution comes from the external magnetic field

$$\mathbf{m}_0 = \chi V \mathbf{B}_0 / \mu_0 \quad (\text{B.4})$$

and a correction $\Delta \mathbf{m}$ due to the field produced by the other particle

$$\mathbf{m} = \mathbf{m}_0 + \Delta \mathbf{m}. \quad (\text{B.5})$$

Using (B.3) and (B.5) in (B.2) yields

$$E = -\frac{1}{2} (\mathbf{m}_0 + \Delta \mathbf{m}) \cdot (\mathbf{B}_0 + \Delta \mathbf{B}) \quad (\text{B.6})$$

$$E = -\frac{1}{2} [\mathbf{m}_0 \mathbf{B}_0 + \mathbf{m}_0 \Delta \mathbf{B} + \Delta \mathbf{m} \mathbf{B}_0 + \Delta \mathbf{m} \Delta \mathbf{B}]. \quad (\text{B.7})$$

Now let us have a look at all terms individually. The dominant contribution to the total energy is the first term, $E_1 = -1/2\mathbf{m}_0\mathbf{B}_0 = -\chi V B_0^2/2\mu_0$, which is the coupling of the undisturbed induced dipole to the external field. This energy contribution is independent of the position and the orientation of the dipole and thus does not affect the structure of the system in any way.

The second term $E_2 = -1/2\mathbf{m}_0\Delta\mathbf{B}$ is the standard dipole-dipole interaction - the interaction of the undisturbed induced dipole of the first particle with the field produced by the second particle. The averaged interaction over one cycle of the external magnetic field yields

$$\begin{aligned}
 \overline{E}_2 &= -\frac{1}{2\pi} \int_0^{2\pi} E_2(\phi) d\phi \\
 &= -\frac{\mu_0}{8\pi^2} \int_0^{2\pi} \frac{3(\mathbf{m}_0\hat{\mathbf{r}})^2 - m_0^2}{r^3} d\phi \\
 &= -\frac{\mu_0 m_0^2}{8\pi^2 r^3} \int_0^{2\pi} \left[3 \sin^2 \theta_p \sin^2 \theta \cos^2 \phi + \cos^2 \theta_p \cos^2 \theta + \right. \\
 &\quad \left. 2 \sin \theta_p \cos \theta_p \sin \theta \cos \theta \cos \phi - 1 \right] d\phi \\
 &= -\frac{(\chi V B_0)^2}{4\pi\mu_0 r^3} \left[\frac{3}{2} \sin^2 \theta_p \sin^2 \theta + \cos^2 \theta_p \cos^2 \theta - 1 \right], \tag{B.8}
 \end{aligned}$$

which is proportional to χ^2 . At magic angle $\theta_p = \theta_m = \arccos(\sqrt{1/3}) \approx 54.7^\circ$, $\sin^2 \theta_p = 2/3$ and $\cos^2 \theta_p = 1/3$, so that the above expression vanishes. The dipolar interaction between two dipoles that follow the direction of the field is therefore zero if the field is precessing at the magic angle.

The third term $E_3 = -1/2\Delta\mathbf{m}\mathbf{B}_0$ represent the coupling of the magnetization induced by the local field of the second particle and the external magnetic field. The averaging of this term over one cycle of the external field reads

$$\begin{aligned}
 \overline{E}_4 &= -\frac{\chi V}{8\pi^2\mu_0} \int_0^{2\pi} \frac{3(\mathbf{m}_0\hat{\mathbf{r}})(\mathbf{B}_0\hat{\mathbf{r}}) - \mathbf{m}_0\mathbf{B}_0}{r^3} d\phi \\
 &= -\frac{(\chi V B_0)^2}{4\pi\mu_0 r^3} \left[\frac{3}{2} \sin^2 \theta_p \sin^2 \theta + \cos^2 \theta_p \cos^2 \theta - 1 \right], \tag{B.9}
 \end{aligned}$$

which is the same result as (B.8) and therefore vanishes at magic angle $\theta_p = \theta_m$.

The last term is the energy of the magnetic dipole induced by the local field of the second particle in the field of that same particle. The energy of this coupling is necessarily negative because the induced magnetic moment always points in the direction of the field. Again, average over one cycle of the precession of the external field yields

$$\begin{aligned}
\bar{E}_4 &= -\frac{\chi V}{2\pi\mu_0} \int_0^{2\pi} \left(\frac{\mu_0}{4\pi} \frac{3(\mathbf{m}_0\hat{\mathbf{r}})\hat{\mathbf{r}} - \mathbf{m}_0}{r^3} \right)^2 d\phi \\
&= -\frac{\mu_0\chi V}{32\pi^3 r^6} \int_0^{2\pi} \left(3(\mathbf{m}_0\hat{\mathbf{r}})^2 + m_0^2 \right) d\phi \\
&= -\frac{\chi^3 V^3 B_0^2}{32\pi^2 \mu_0 r^6} \left[\frac{3}{2} \sin^2 \theta_p \sin^2 \theta + \cos^2 \theta_p \cos^2 \theta + 1 \right], \tag{B.10}
\end{aligned}$$

The expression in brackets is very similar to (B.8) except that instead of subtraction of 1 there is its addition. At magic angle, therefore, (B.10) doesn't disappear, but reads

$$\bar{E}_4 = -\frac{\chi^3 V^3 B_0^2}{16\pi^2 \mu_0} \frac{1}{r^6}. \tag{B.11}$$

The lowest-order nonzero correction to E_1 is thus isotropic attractive $1/r^6$ interaction, analogous to the Debye dipole-induced dipole interaction. The pair potential is independent of the relative orientation of the particles.

Particle tracking algorithms

Particle recognition and tracking of videos where objects do not come into contact is based on standard digital video microscopy tracking algorithms [52]: a threshold level T is defined either by user or automatically with Otsu's method, the image I is binarized then center of each object is calculated as

$$\begin{aligned} x_c &= \frac{\sum_{x,y} x |I(x,y) - T|}{\sum_{x,y} |I(x,y) - T|} \\ y_c &= \frac{\sum_{x,y} y |I(x,y) - T|}{\sum_{x,y} |I(x,y) - T|}. \end{aligned} \quad (\text{C.1})$$

Each pixel in center calculation is weighted according to its deviation from the threshold, e.g. if a dark particle on a bright background is tracked then black pixels have higher weight than gray pixels comprising the object.

Simple tracking algorithm fails either if tracked objects come into contact or if the image background is not uniform. Under such circumstances advanced recognition techniques have to be used. In our software we implemented convolution based tracking. An image of the targeted object I_{obj} of size $(2M + 1) \times (2N + 1)$ pixels is taken from a desired frame of the video and to be used as a convolution kernel $K(i, j) = I_{obj}(i, j) - \bar{I}_{obj}$ its average value is subtracted. For each pixel $I(x, y)$ of the original image the following convolution I_C is calculated

$$I_C(x, y) = \sum_{i=-M, j=-N}^{M, N} K(i, j) I(x + i, y + j). \quad (\text{C.2})$$

After all pixels of the image are processed in such manner, a new image is created from the normalized convolution values $I_{new}(x, y) = 255 \cdot \frac{I_C(x,y) - \min(I_C)}{\max(I_C) - \min(I_C)}$. The new image is bright in regions where the original image I is similar to the targeted object and dark in all other regions. If two particles are in contact in the original image they show up as two clearly separated white spots in the new image. The convoluted image I_{new} can be therefore further analyzed with the standard tracking algorithms described above to obtain particle positions.

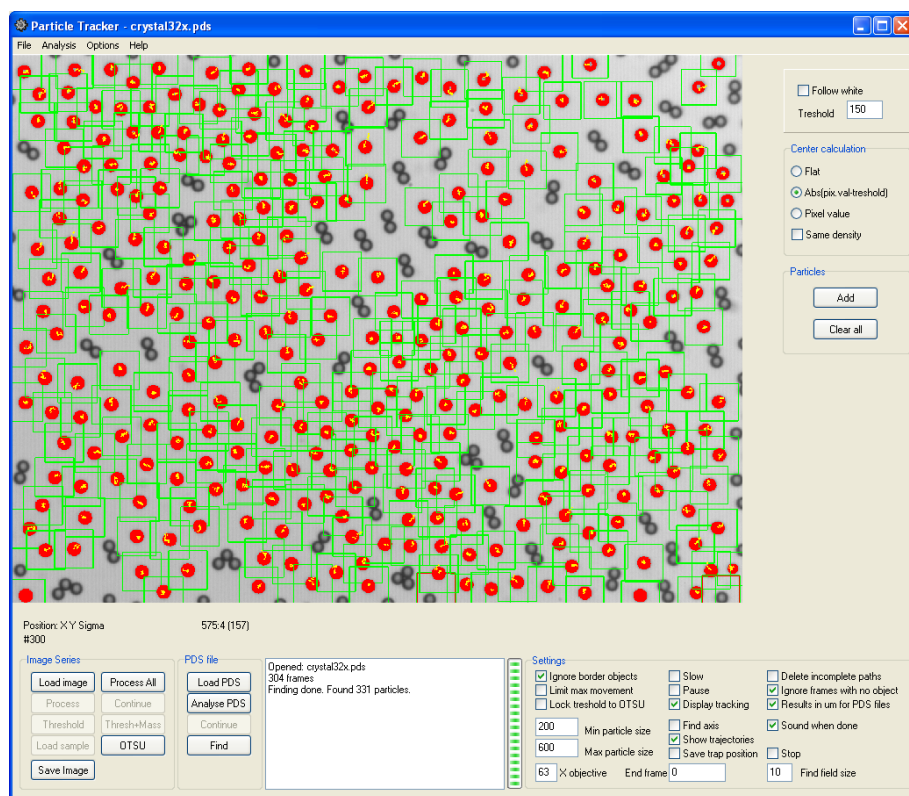


FIGURE C.1: Screenshot of *PartTrack* software after successful tracking of 331 beads. Tracked particles are labeled with red, their trajectories through the video are marked with yellow lines.

Bibliography

- [1] Chaikin, P. M. and Lubensky, T. C., *Principles of Condensed Matter Physics*, Cambridge University Press, 2000.
- [2] Kleman, M. and Lavrentovich, O. D., *Soft Matter Physics, An Introduction*, Springer-Verlag New York, 2003.
- [3] Stark, H., Phys. Rep. **351** (2001) 387.
- [4] Kuksenok, O. V., Ruhwandl, R. W., Shiyanovskii, S. V., and Terentjev, E. M., Phys. Rev. E **54** (1996) 5198.
- [5] Yada, M., Yamamoto, J., and Yokoyama, H., Phys. Rev. Lett. **92** (2004) 185501.
- [6] Smalyukh, I. I., Lavrentovich, O. D., Kuzmin, A. N., Kachynski, A. V., and Prasad, P. N., Phys. Rev. Lett. **95** (2005) 157801.
- [7] Smalyukh, I. I., Kuzmin, A. N., Kachynski, A. V., Prasad, P. N., and Lavrentovich, O. D., Appl. Phys. Lett. **86** (2005) 021913.
- [8] Smalyukh, I. I., Kachynski, A. V., Kuzmin, A. N., and Prasad, P. N., Proc. Natl. Acad. Sci. U.S.A. **103** (2006) 18048.
- [9] Škarabot, M. et al., Phys. Rev. E **77** (2008) 031705.
- [10] Ognysta, U. et al., Phys. Rev. Lett. **100** (2008) 217803.
- [11] Muševič, I. et al., Phys. Rev. Lett. **93** (2004) 187801.
- [12] Poulin, P., Cabuil, V., and Weitz, D. A., Phys. Rev. Lett. **79** (1997) 4862.
- [13] Noël, C. M., Bossis, G., Chaze, A.-M., Giulieri, F., and Lacis, S., Phys. Rev. Lett. **96** (2006) 217801.
- [14] Whitesides, G. M. and Grzybowski, B., Science **295** (2002) 2418.
- [15] Grzybowski, B. A., Wilmer, C. E., Kim, J., Browne, K. P., and Bishop, K. J. M., Soft Matter **5** (2009) 1110 .

BIBLIOGRAPHY

- [16] Russel, W. B., Saville, D. A., and Schowalter, W. R., *Colloidal Dispersions*, Cambridge Univ. Press, 1989.
- [17] Kremer, K., Robbins, M. O., and Grest, G. S., Phys. Rev. Lett. **57** (1986) 2694.
- [18] Mau, S.-C. and Huse, D. A., Phys. Rev. E **59** (1999) 4396.
- [19] Nelson, D. R., Nano Letters **2** (2002) 1125.
- [20] Yethiraj, A. and van Blaaderen, A., Nature **421** (2003) 513.
- [21] Malescio, G. and Pellicane, G., Nat Mater **2** (2003) 97.
- [22] Jagla, E. A., J. Chem. Phys. **110** (1999) 451.
- [23] Norizoe, Y. and Kawakatsu, T., Europhys Lett **72** (2005) 583.
- [24] Glaser, M. A. et al., Europhys Lett **78** (2007) 46004.
- [25] Mason, T. G. and Weitz, D. A., Phys. Rev. Lett. **74** (1995) 1250.
- [26] Mason, T. G., Ganesan, K., van Zanten, J. H., Wirtz, D., and Kuo, S. C., Phys. Rev. Lett. **79** (1997) 3282.
- [27] Gisler, T. and Weitz, D., Curr Opin Colloid Interface Sci **3** (1998) 586.
- [28] Freundlich, H. and Seifritz, W., Zeitschrift fur physikalische chemie **104** (1922) 233.
- [29] Evans, E. A. and Skalak, R., *Mechanics & Thermodynamics Of Biomembranes*, CRC Press, 1980.
- [30] Radmacher, M., Fritz, M., and Hansma, P., Biophys. J. **69** (1995) 264.
- [31] Valentine, M. T., Dewalt, L., and Ou-Yang, H. D., J Phys Condens Matter **8** (1996) 9477.
- [32] Ziemann, F., Rädler, J., and Sackmann, E., Biophys. J. **66** (1994) 2210.
- [33] Amblard, F., Maggs, A. C., Yurke, B., Pargellis, A. N., and Leibler, S., Phys. Rev. Lett. **77** (1996) 4470.
- [34] Bausch, A. R., Ziemann, F., Boulbitch, A. A., Jacobson, K., and Sackmann, E., Biophys. J. **75** (1998) 2038.
- [35] Furst, E. M., Curr Opin Colloid Interface Sci **10** (2005) 79.
- [36] Atakhorrami, M., Koenderink, G. H., Schmidt, C. F., and MacKintosh, F. C., Phys. Rev. Lett. **95** (2005) 208302.
- [37] Ashkin, A., Phys. Rev. Lett. **24** (1970) 156.

-
- [38] Ashkin, A. and Dziedzic, J. M., *Appl. Phys. Lett.* **19** (1971) 283.
- [39] Ashkin, A., Dziedzic, J. M., Bjorkholm, J. E., and Chu, S., *Opt. Lett.* **11** (1986) 288.
- [40] Sheetz, M. P., editor, *Laser Tweezers in Cell Biology (Methods in Cell Biology, V. 55)*, Academic Press Inc., 1998.
- [41] Grier, D. G., *Nature* **424** (2003) 810.
- [42] Ashkin, A., Dziedzic, J. M., and Yamane, T., *Nature* **330** (1987) 769.
- [43] Finer, J. T., Simmons, R. M., and Spudich, J. A., *Nature* **368** (1994) 113.
- [44] Yin, H. et al., *Science* **270** (1995) 1653.
- [45] Perkins, T., Smith, D., and Chu, S., *Science* **264** (1994) 819.
- [46] Ashkin, A., *Biophys. J.* **61** (1992) 569.
- [47] Smith, S. B., Finzi, L., and Bustamante, C., *Science* **258** (1992) 1122.
- [48] Strick, T. R., Allemand, J.-F., Bensimon, D., Bensimon, A., and Croquette, V., *Science* **271** (1996) 1835.
- [49] Strick, T. R., Croquette, V., and Bensimon, D., *Nature* **404** (2000) 901.
- [50] Fonnum, G., Johansson, C., Molteberg, A., Morup, S., and Aksnes, E., *J. Magn. Magn. Mater.* **293** (2005) 41, Proceedings of the Fifth International Conference on Scientific and Clinical Applications of Magnetic Carriers.
- [51] Loudet, J. C., Hanusse, P., and Poulin, P., *Science* **306** (2004) 1525.
- [52] Crocker, J. C. and Grier, D. G., *J Colloid Interface Sci* **179** (1996) 298.
- [53] Poulin, P., Stark, H., Lubensky, T. C., and Weitz, D. A., *Science* **275** (1997) 1770.
- [54] Loudet, J.-C., Barois, P., and Poulin, P., *Nature* **407** (2000) 611.
- [55] Smalyukh, I. I. et al., *Phys. Rev. Lett.* **93** (2004) 117801.
- [56] Nych, A. B. et al., *Phys. Rev. Lett.* **98** (2007) 057801.
- [57] Meeker, S. P., Poon, W. C. K., Crain, J., and Terentjev, E. M., *Phys. Rev. E* **61** (2000) R6083.
- [58] Guzmán, O., Kim, E. B., Grollau, S., Abbott, N. L., and de Pablo, J. J., *Phys. Rev. Lett.* **91** (2003) 235507.
- [59] Muševič, I., Škarabot, M., Tkalec, U., and Ravnik, M. and Žumer, S., *Science* **313** (2006) 954.

BIBLIOGRAPHY

- [60] Škarabot, M. et al., Phys. Rev. E **76** (2007) 051406.
- [61] Loudet, J. C. and Poulin, P., Phys. Rev. Lett. **87** (2001) 165503.
- [62] Stark, H., Phys. Rev. E **66** (2002) 041705.
- [63] Pergamenschchik, V. M., Phys. Rev. E **48** (1993) 1254.
- [64] Rapini, A. and Papoular, M., J. Phys. Paris C **C4** (1969).
- [65] Ramaswamy, S., Nityananda, R., Raghunathan, V. A., and Prost, J., Mol Cryst Liq Cryst **288** (1996) 175.
- [66] Ruhwandl, R. W. and Terentjev, E. M., Phys. Rev. E **55** (1997) 2958.
- [67] J.Fukuda, Lev, B. I., and Yokoyama, H., J Phys Condens Matter **15** (2003) 3841.
- [68] de Gennes, P. G. and Prost, J., *The Physics of Liquid Crystals, 2nd ed.*, Oxford Science, Oxford, 1993.
- [69] Chandrasekhar, S., *Liquid Crystals, 2nd edition*, Cambridge University Press, Cambridge, 1992.
- [70] Jackson, J. D., *Classical Electrodynamics, 2nd ed.*, John Wiley & Sons, New York, 1975.
- [71] Poulin, P. and Weitz, D. A., Phys. Rev. E **57** (1998) 626.
- [72] Bogi, A., Martinot-Lagarde, P., Dozov, I., and Nobili, M., Phys. Rev. Lett. **89** (2002) 225501.
- [73] Pires, D., Fleury, J.-B., and Galerne, Y., Phys. Rev. Lett. **98** (2007) 247801.
- [74] Chen, G.-P., Takezoe, H., and Fukuda, A., Liq. Cryst. **5** (1989) 341.
- [75] Torquato, S., Soft Matter **5** (2009) 1157.
- [76] Camp, P. J., Phys. Rev. E **68** (2003) 061506.
- [77] Zahn, K., Mendez-Alcaraz, J. M., and Maret, G., Phys. Rev. Lett. **79** (1997) 175.
- [78] Zahn, K. and Maret, G., Phys. Rev. Lett. **85** (2000) 3656.
- [79] Pieranski, P., Strzelecki, L., and Pansu, B., Phys. Rev. Lett. **50** (1983) 900.
- [80] Tlusty, T. and Safran, S. A., Science **290** (2000) 1328.
- [81] Helgesen, G., Pieranski, P., and Skjeltorp, A. T., Phys. Rev. Lett. **64** (1990) 1425.
- [82] Sandre, O. et al., Phys. Rev. Lett. **59** (1999) 1736.

-
- [83] Melle, S., Fuller, G. G., and Rubio, M. A., Phys. Rev. E **61** (2000) 4111.
- [84] Bleil, S., Marr, D. W. M., and Bechinger, C., Appl. Phys. Lett. **88** (2006) 263515.
- [85] Sawetzki, T., Rahmouni, S., Bechinger, C., and Marr, D. W. M., Proc. Natl. Acad. Sci. U.S.A. **105** (2008) 20141.
- [86] Tierno, P., Muruganathan, R., and Fischer, T. M., Phys. Rev. Lett. **98** (2007) 028301.
- [87] van Blaaderen, A., Ruel, R., and Wiltzius, P., Nature **385** (1997) 321.
- [88] Lin, K. et al., Phys. Rev. Lett. **85** (2000) 1770.
- [89] Gardel, M., Valentine, M., and Weitz, D., *Microscale Diagnostic Techniques*, Springer Berlin Heidelberg, 2005.
- [90] MacKintosh, F. and Schmidt, C., Curr Opin Colloid Interface Sci **4** (1999) 300 .
- [91] Waigh, T. A., Rep. Prog. Phys. **68** (2005) 685.
- [92] Cicuta, P. and Donald, A. M., Soft Matter **3** (2007) 1449.
- [93] Mason, T. G. and Weitz, D. A., Phys. Rev. Lett. **75** (1995) 2770.
- [94] Liu, J. et al., Phys. Rev. Lett. **96** (2006) 118104.
- [95] Gittes, F., Schnurr, B., Olmsted, P. D., MacKintosh, F. C., and Schmidt, C. F., Phys. Rev. Lett. **79** (1997) 3286.
- [96] Addas, K. M., Schmidt, C. F., and Tang, J. X., Phys. Rev. E **70** (2004) 021503.
- [97] Brau, R. R. et al., J. Opt. A: Pure Appl. Opt. **9** (2007) S103.
- [98] Hough, L. and Ou-Yang, H., Journal of Nanoparticle Research **1** (1999) 495.
- [99] Levine, A. J. and Lubensky, T. C., Phys. Rev. Lett. **85** (2000) 1774.
- [100] Valentine, M. T. et al., Phys. Rev. E **64** (2001) 061506.
- [101] Valentine, M. et al., Biophys. J. **86** (2004) 4004.
- [102] Chen, D. T. et al., Phys. Rev. Lett. **90** (2003) 108301.
- [103] Hough, L. A. and Ou-Yang, H. D., Phys. Rev. E **65** (2002) 021906.
- [104] Atakhorrami, M. et al., Phys. Rev. E **73** (2006) 061501.
- [105] Towler, B. W., Rupp, C. J., Cunningham, A. B., and Stoodley, P., Biofouling **19** (2003) 279.

BIBLIOGRAPHY

- [106] Cense, A. et al., *J. Microbiol. Methods* **67** (2006) 463.
- [107] Plopper, G., *Cells*, Jones and Bartlett Publishers, 2006.
- [108] NCBI taxonomy database, T., *Vibrio* sp. dsm 14379.
- [109] Thompson, F., Iida, T., and Swings, J., *Microbiol Mol Biol Rev.* **68** (2004) 403.

List of publications related to the work described in this thesis

1. KOTAR, Jurij, VILFAN, Mojca, OSTERMAN, Natan, BABIČ, Dušan, ČOPIČ, Martin, POBERAJ, Igor. Interparticle potential and drag coefficient in nematic colloids. *Phys. rev. lett.*, 2006, vol. 96, 207801-1-207801-4.
2. OSTERMAN, Natan, BABIČ, Dušan, POBERAJ, Igor, DOBNIKAR, Jure, ZIHERL, Primož. Observation of condensed phases of quasilplanar core-softened colloids. *Phys. rev. lett.*, 2007, 99, 248301-1-248301-4.
3. VILFAN, Mojca, OSTERMAN, Natan, ČOPIČ, Martin, RAVNIK, Miha, ŽUMER, Slobodan, KOTAR, Jurij, BABIČ, Dušan, POBERAJ, Igor. Confinement effect on interparticle potential in nematic colloids. *Phys. rev. lett.*, 2008, 101, 237801-1-237801-4
4. BABIČ, Dušan, OSTERMAN, Natan, POBERAJ, Igor, DOBNIKAR, Jure, FRENKEL, Daan, ZIHERL, Primož. Crystalline colloidal membranes. *in preparation*

Razširjeni povzetek v slovenskem jeziku

(Abstract in Slovene)

6.1 Uvod

Kondenzirana mehka snov [1, 2] so materiali, ki se po svojih strukturnih in dinamičnih lastnostih nahajajo med kristali in tekočinami, obsegajo pa mnogo različnih oblik. Mehka snov je sestavljena iz gradnikov, ki med seboj šibko interagirajo, tako da termične fluktuacije, zunanja polja in robni pogoji močno vplivajo na njeno strukturo in lastnosti. Med mehko snov uvrščamo tekoče kristale, koloide, polimerne raztopine, pene, gele, najbolj kompleksni predstavniki pa so biološki sistemi različnih velikostnih skal.

Napredek v raziskavah mehke snovi v največji meri omogočajo razpoložljive eksperimentalne tehnike. Eno izmed novejših eksperimentalnih orodij za manipulacijo mikrodelcev je magneto-optična pinceta, kombinacija optične pincete in magnetne pincete s homogenim poljem, ki združuje prednosti obeh metod. Optična pinceta omogoča lokalno mikromanipulacijo posameznih delcev in aplikacijo ter meritev sil v območju pikonewtonov. Magnetna pinceta ustvarja homogeno magnetno polje poljubne velikosti in smeri ter tako povzroča interakcijo med induciranimi dipoli superparamagnetnih delcev.

V disertaciji z uporabo magneto-optične pincete raziskujemo tri zanimive probleme s področja mehke snovi. V prvem delu se osredotočimo na meddelčne potencialne nematskih koloidov. Natančno izmerimo odbojno strukturno silo med dvema koloidnima delcema s kvadrupolno simetrijo direktorja in pojasnimo njeno odvisnost od meddelčne razdalje. Preučimo vpliv ogradjenosti tekočega kristala na meddelčni potencial.

V drugem delu se posvetimo povezavi med meddelčnimi potenciali in nastalimi večdelčnimi strukturami. Z magnetno pinceto induciramo razne tipe meddelčnih potencialov v dvo- in tridimenzionalnih sistemih superparamagnetnih koloidnih delcev. S kombinacijo pravokotnega statičnega zunanjega polja in geometrijske ogradjenosti v 2D dosežemo zmešan izotropni odbojni potencial, ki stabilizira neobičajne mezofaze koloidnih delcev. Kompleksni meddelčni potenciali ustvarimo tudi s časovno modulacijo zunanjega magnetnega polja. Precesija polja po površini stožca z "magičnim" vršnim kotom 54.7° izpovpreči $1/r^3$ člen v interakciji in povzroči izotropen privlačen meddelčni potencial, ki v 3D stabilizira tesno zložene heksagonalne "plahte".

V zadnjem delu obravnavamo nekaj metod za meritev mikroreoloških lastnosti z optično pinceto. S kombinacijo optične pincete, ki služi za mikromanipulacijo

sond, in modula za videomikroskopijo zgradimo sistem za pasivne enodelčne ter aktivne eno- in dvodelčne mikrereološke meritve. Sistem testiramo v vodi in ga nato uporabimo za meritve mehanskih lastnosti rastoče bakterijske populacije *Vibrio sp.*

6.2 Eksperimentalne metode

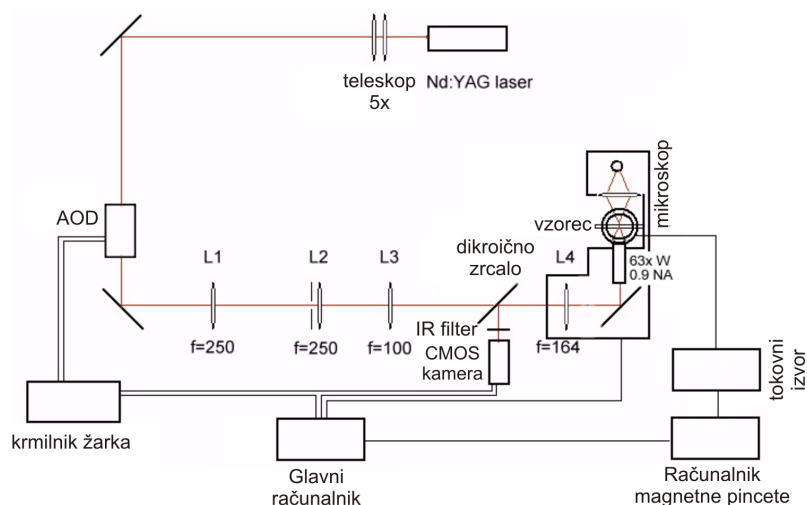
Optična pinceta

Optična pinceta je naprava, ki s pomočjo močno fokusiranega laserskega snopa omogoča brezkontaktno manipulacijo mikronskih in submikronskih delcev ter meritev sil v območju pikonewtonov. Ashkin [37] je leta 1970 pokazal, da mikronske delce z lomnim količnikom, večjim od okoliškega medija, povleče v središče močno fokusiranega laserskega snopa. Od leta 1986, ko so Ashkin, Chu in sodelavci razvili enožarkovno gradientno optično pinceto, ki omogoča ujetje delca v 3D prostoru (in ne samo ob površinah eksperimentalne celice), se tehnika stalno razvija. Danes optična pinceto uporabljajo na mnogih področjih (pregled v [40, 41]), še posebno v biologiji za neinvazivno manipulacijo celic, organel, kompleksnih molekul in drugih delcev s submikronsko natančnostjo ter v biofiziki za meritev sil v območju od 0.1 do 100 pN.

Optična past je ustvarjena s fokusiranjem laserskega snopa z mikroskopskim objektivom. Na delec v pasti deluje optična sila, sestavljena iz dveh komponent: sipalne komponente (fotonski pritisk) v smeri širjenja žarka in gradientne komponente v smeri največjega gradienta intenzitete žarka. Če je gradientna komponenta večja od sipalne komponente, je delec ujet v točki, kjer se uravnotežijo sila teže, vzgon in optična sila.

Optična pinceta je sestavljen iz treh glavnih elementov: laserja, sistema za krmiljenje laserskega snopa ter objektiva z veliko numerično aperturo. Pinceta je ponavadi postavljena na komercialni optični mikroskop, običajno invertni, saj tako gravitacijska sila deluje v nasprotno smer kot sipalna komponenta optične sile, kar omogoča stabilnejše ujetje delca v treh dimenzijah. Za krmiljenje laserskega snopa obstaja več načinov, npr. z zrcali na piezo elementih, prostorskim modulatorjem svetlobe (holografska optična pinceta) ali akusto-optičnimi deflektorji.

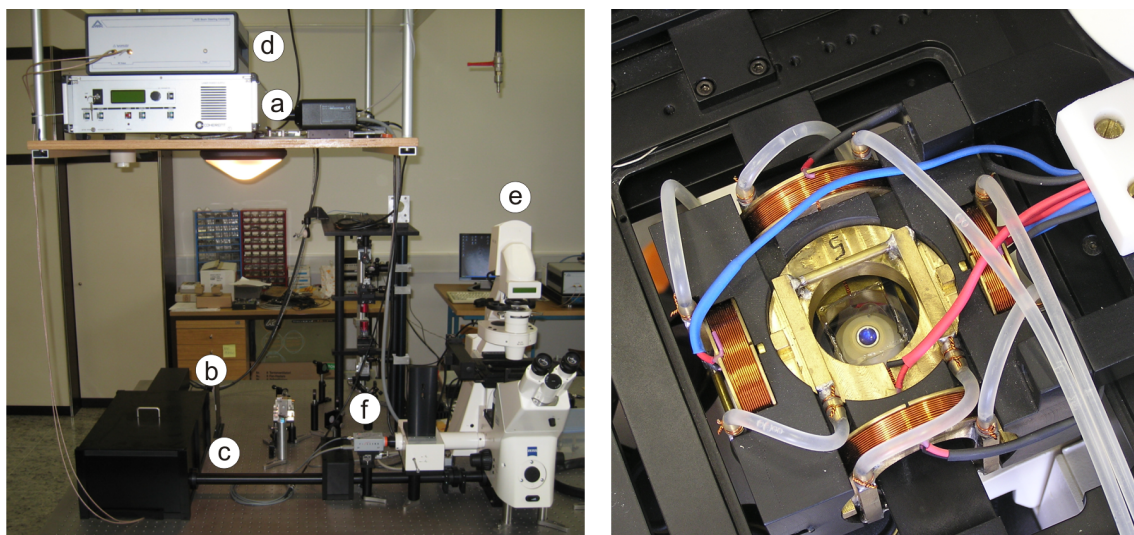
V raziskavah smo uporabljali optično pinceto, zgrajeno okrog invertnega optičnega mikroskopa (Zeiss, Axiovert200M) z objektivom (Zeiss, Achroplan 63x/0.9W; vodna imerzija, N.A. 0.9) in diodno črpanega trdninskega laserja (Coherent, Compass 1064-2500, valovna dolžina 1064 nm, maksimalna moč 2.5 W). Laserski snop usmerjata dva pravokotno postavljena akusto-optična deflektorja (AA Opto-electronic, DTSXY-250-1064-002, akustična frekvenca 60-90 Mhz), akustično valovanje zanj pa proizvaja računalniško nadzorovan kontroler za krmiljenje žarka (Aresis, BSC-01). Ta omogoča nanometersko natančnost določanje lege pasti in časovno deljenje žarka na več tisoč "hkratnih" neodvisnih optičnih pasti. Sliko zajema CMOS kamera (Pixelink, PLA-741), ki podpira snemanje s hitrostjo do 1000 slik na sekundo.



SLIKA 6.2: Shema postavitve magneto-optične pincete. Laserski snop je razširjen in voden skozi par pravokotno postavljenih akusto-optičnih deflektorjev na vhodno zenico objektivna z veliko numerično aperturo. Glavni računalnik nadzira krmilnik žarka, kamero in invertni mikroskop ter je povezan z računalnikom, ki nadzoruje tokovni izvor magnetne pincete.

Magnetna pinceta

Magnetna pinceta je naprava, ki deluje na magnetne delce s silo z uporabo gradienta magnetnega polja. Zaradi primerne območja dosegljivih sil (do nanonewtonov) in preproste arhitekture je magnetna pinceta pogosto orodje v biofizikalnih raziskavah, npr. za manipulacijo posameznih molekul, reologijo mehke snovi in preučevanje vpliva sil na delovanje celic [47, 48, 49].



SLIKA 6.3: *Levo*: Postavitev eksperimenta: (a) laserski gonilnik, (b) laserska glava, (c) akusto-optična deflektorja, (d) krmilnik žarka, (e) invertni mikroskop, (f) CMOS kamera. *Desno*: Magnetna pinceta, pritrjena na mikroskop; v sredini sta vidna objektiv in vzorec.

Druga možnost ustvarjanja magnetne sile je uporaba homogenih magnetnih polj in superparamagnetnih delcev. Sila v tem primeru ne deluje na posamezen delec,

temveč vedno med dvema (ali večimi) delci. Magnetna sila se pojavi med induciranimi magnetnimi dipolnimi momenti delcev. S primerno izbiro smeri magnetnega polja se lahko doseže privlačno ali odbojno meddelčno silo.

V našem sistemu magnetno polje ustvarjajo tri ortogonalno postavljene pari tuljav. Tokove zanje ustvarja računalniško nadzorovan tokovni generator. Ta ima 6 neodvisnih kanalov, v katerih se oblika toka ustvarja s tehnologijo direktne sinteze (DDS), kar v končni fazi omogoča poljubno obračanje in spreminjanje velikosti magnetnega polja v vzorcu. Največje dosegljivo statično magnetno polje v smeri optične osi mikroskopa (z-smer) je 40 mT, v pravokotni smeri pa zaradi večjega razmika med tuljavami 5.8-krat manj, torej 7 mT. V primeru oscilirajočega polja so zaradi induktivnosti tuljav dosegljivi manjši električni tokovi, tako da je npr. največje nepopačeno sinusno oscilirajoče magnetno polje v ravnini vzorca pri frekvenci 400 Hz v veliko približno 4 mT, kar pa več kot dovolj za izvajane poskuse.

Magnetna sila

V eksperimentih smo uporabljali dve vrsti superparamagnetnih kroglic *Dynabeads* proizvajalca Dynal, *MyOne Carboxy* premera $1.05 \mu\text{m}$ in *M450* s premerom $4.4 \mu\text{m}$, njihova magnetna susceptibilnost χ pa je 1.37 oz. 1.63 [50]. V zunanjem magnetnem polju \mathbf{B} se v superparamagnetnem delcu s prostornino V inducira magnetni dipolni moment \mathbf{m} , ki je za majhna polja (do 10 mT) približno sorazmeren polju,

$$\mathbf{m} = \chi V \frac{\mathbf{B}}{\mu_0}. \quad (6.3)$$

Interakcijska energija dveh dipolnih momentov \mathbf{m}_1 in \mathbf{m}_2 , ki ju povezuje vektor \mathbf{r} , je

$$E = \frac{\mu_0}{4\pi} \left(\frac{(\mathbf{m}_1 \cdot \mathbf{m}_2)}{r^3} - \frac{3(\mathbf{m}_1 \cdot \mathbf{r})(\mathbf{m}_2 \cdot \mathbf{r})}{r^5} \right). \quad (6.4)$$

Če sta delca enaka, se gornji izraz v posebnih primerih zelo poenostavi. Če je magnetno polje pravokotno na ravnino delcev, je interakcija

$$E = \frac{\chi^2 V^2 B_0^2}{4\pi \mu_0 r^3} \quad (6.5)$$

odbojna, ko pa je magnetno polje v smeri vektorja, ki povezuje delca, je interakcija

$$E = -\frac{\chi^2 V^2 B_0^2}{2\pi \mu_0 r^3} \quad (6.6)$$

privlačna in dvakrat močnejša. Če magnetno polje hitro kroži v ravnini delcev, povprečenje energije po enem obratu da

$$\bar{E} = -\frac{\chi^2 V^2 B_0^2}{8\pi \mu_0 x^3}, \quad (6.7)$$

kar pomeni izotropno privlačno parsko interakcijo.

6.3 Meddelčni potencial v ograjenem nematiku

Interakcije med krogelnimi delci v nematskem tekočem kristalu (TK) povzročijo bogat nabor pojavov, npr. urejanje delcev v linearne verige [53, 54] ali v dvodimenzionalne koloidne kristale [59, 60]. Izvor opaženih pojavov je v močno anizotropnih silah dolgega dosega, ki jih posredujejo elastične deformacije TK [3]. Vsak v TK vstavljen koloidni delec deformira okoliško direktorsko polje, kar povzroči nastanek TK *defektov*, tj. območij z nezveznim direktorskim poljem. Deformacija direktorja je odvisna od velikosti in oblike delca ter jakosti in tipa sidranja na njegovi površini. Homeotropno sidranje (površina delca vsiljuje pravokotno ureditev TK molekul) povzroči, odvisno od jakosti, dipolno ali kvadrupolno simetrijo direktorskega polja okrog delca, planarno sidranje (površina delca vsiljuje vzporedno ureditev TK molekul) pa kvadrupolno simetrijo direktorja [3, 4]. Koloidne delce skupaj z okoliško deformacijo direktorja pogosto krajše imenujemo elastični dipoli oz. kvadrupoli.

Interakcije med koloidnimi delci v nematskem TK so študirali s kombinacijo optične mikroskopije in optične pincete. Statično silo med dvema elastičnima dipoloma so merili z optično pinceto [5, 6, 7, 8]. S kombinacijo dinamičnih in statičnih meritev so izmerili kotno odvisnost sile med dvema elastičnima kvadrupoloma [7]. Z dinamičnimi meritvami, kjer so opazovali pot delca, ki so ga spustili iz optične pasti, so določili interakcije med elastičnimi kvadrupoli in dipoli [9, 10].

Optična pinceta je priročno orodje za manipulacijo koloidnih delcev, toda močno električno polje laserja vpliva na direktorsko polje TK [11], kar oteži interpretacijo merskih rezultatov. Reorientacijskim vplivom pincete se je moč izogniti z uporabno TK manjše dvolomnosti ali z zmanjšanjem moči laserja [7, 6], toda v obeh primerih se zmanjša jakost pasti. Alternativni način merjenja elastičnih sil med delci v TK z magnetnimi delci in magnetnim poljem za njihovo manipulacijo, saj majhna magnetna polja nimajo znatnega vpliva na direktor. Prvo meritev te vrste je opravil Poulin [12], v njej pa so v TK dodali ferrofluidne kapljice, z zunanjim statičnim magnetnim poljem pa so povzročali odbojne sile med njimi. Statično magnetno polje je bilo uporabljeno tudi za analizo sil med delci s homeotropnim sidranjem [13].

Podobne eksperimente smo izvedli z magneto-optično pinceto. Optična pinceta omogoča manipulacijo posameznih koloidnih delcev, ko pa so ti na pravih položajih, se optično pinceto ugasne, privlačne ali odbojne sile med delci pa se ustvari z magnetnim poljem. Tako smo lahko natančno izmerili kvadrupolno interakcijo med sferičnimi delci v nematskem TK za široko območje medsebojnih razdalj, določili efektivni koeficient upora delcev, karakterizirali vpliv ograjene geometrije na interakcijo ter izmerili temperaturno odvisnost kvadrupolne sile.

Kvadrupolna interakcija in vpliv ograjene geometrije

Parski potencial med sferičnimi koloidnimi delci v TK je možno analitično izračunati v približku multipolnega razvoja [65, 66, 3]. Če predpostavimo, da direktorsko polje okrog delca obdrži dipolno ali kvadrupolno strukturo, se Frankova eno-konstantna

elastična energija s prispevkom zaradi sidranja na površni delca zapiše kot

$$F = \int \frac{1}{2} K [(\nabla \cdot \mathbf{n})^2 + (\nabla \times \mathbf{n})^2] d^3 r - \oint \frac{1}{2} W(\mathbf{n} \cdot \mathbf{v})^2 dS. \quad (6.8)$$

Jakost sidranja W je pozitivna v primeru homeotropnega sidranja in negativna pri planarnem sidranju. Za šibko sidranje $Wr_0/K \ll 1$ (r_0 je radij delca, K elastična konstanta TK) ali dovolj daleč od drugih delcev, je možno diferencialno enačbo za minimum Frankove proste energije linearizirati in nato izračunati direktorsko polje okoli delca. Interakcijska energija dveh delcev se izračuna iz prekrivanja deformacijskih območij direktorskih polj in je za dva elastična kvadrupola [3]

$$U = \frac{16\pi K c_1 c_2}{r^5} \left(1 - 10 \cos^2 \theta + 105/9 \cos^4 \theta\right). \quad (6.9)$$

Tu je θ kot med vektorjem od prvega do drugega delca \mathbf{r} in smerjo nemotenega direktorja \mathbf{n} , c_1 in c_2 sta kvadrupolna momenta delcev. Za enaka delca, ki se nahajata v ravnini pravokotno na direktor ($\theta = \pi/2$), se zgornji izraz poenostavi. Zaradi preprostosti uvedemo še nov prefaktor, tako da lahko interakcijsko energijo med delcema v neskončnem nematskem mediju zapišemo kot

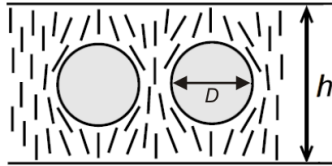
$$U = \frac{C_U}{(x/D)^5}, \quad (6.10)$$

meddelčno silo pa kot

$$F_{LC} = \frac{C_F}{(x/D)^6}, \quad (6.11)$$

kjer je x razdalja med delcema.

V realnosti TK medij ni neskončen. Površine celice, v kateri se nahaja TK, vplivajo na meddelčno interakcijo, saj omejujejo načine elastičnih deformacij medija in lahko preko TK interagirajo z delci [67]. Vpliv površin je moč modelirati podobno kot vpliv prevodnih plošč v elektrostatici [68, 69] z metodo zrcalnih slik nabojev. Elektrostatski potencial kvadrupola med dvema prevodnima ploščama se zapiše v obliki modificirane Besselove funkcije $K_0(kx)$, ki za velike x pojema eksponentno [70]. V eksperimentih smo uporabljali nematski tekoči kristal 5CB in superparamagnetne



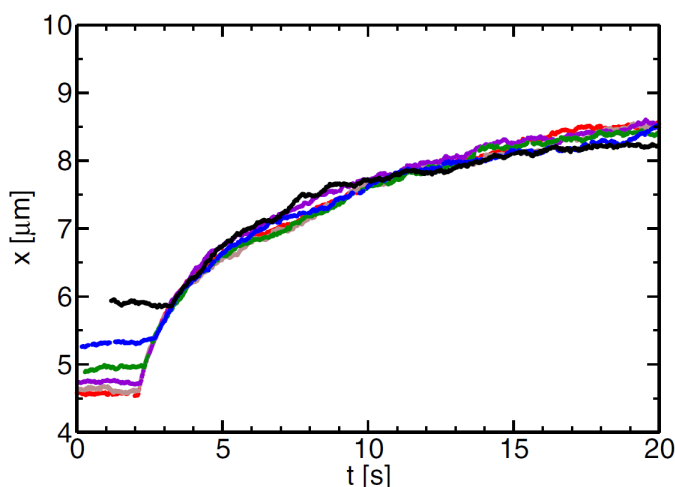
SLIKA 6.4: Stranski pogled na TK celico debeline h s kroglicama premera D . Palčke simbolizirajo direktorsko polje okrog planarnih kroglic v homeotropni celici.

kroglice *Dynal Dynabeads M-450* premera $D = 4.4 \mu\text{m}$. Suhe kroglice smo z ultrazvočno kopeljo dispergirali v TK, nato pa vse skupaj zaprli med dve silanizirani stekelci z medsebojno razdaljo malo več od premera kroglic, hkrati pa manj od dveh premerov. Debelino celice smo določili naknadno iz opazovanja nagnjenih parov kroglic v stiku. Stekelci sta vsiljevali homeotropno, površine kroglic pa planarno ureditev TK (slika 6.4).

Rezultati

Opravili smo več tipov eksperimentov. Pri najpreprostejšemu smo z magnetno silo delca približali na določeno medsebojno razdaljo (kjer je bila privlačna magnetna sila enaka odbojni TK sili), nato magnetno polje izklopili ter opazovali gibanje delcev. Tipične poti za različne začetne medsebojne razdalje so prikazane na sliki 6.5.

Na grafu se vidi, da so poti delcev neodvisne od začetne razdalje. Prekrivanje poti kaže, da so relaksacijski procesi v nematskem TK mnogo hitrejši od gibanja kroglic, tako da lahko direktorsko polje obravnavamo kot kvazistacionarno. Gibanje kroglic določa samo efektivni koeficient upora γ_{eff} , ki vključuje upor zaradi gibanja po mediju, vpliv površin celice in upor zaradi distorzij TK.



SLIKA 6.5: Meddelčna razdalja x v odvisnosti od časa t za različne začetne razdalje x_0 .

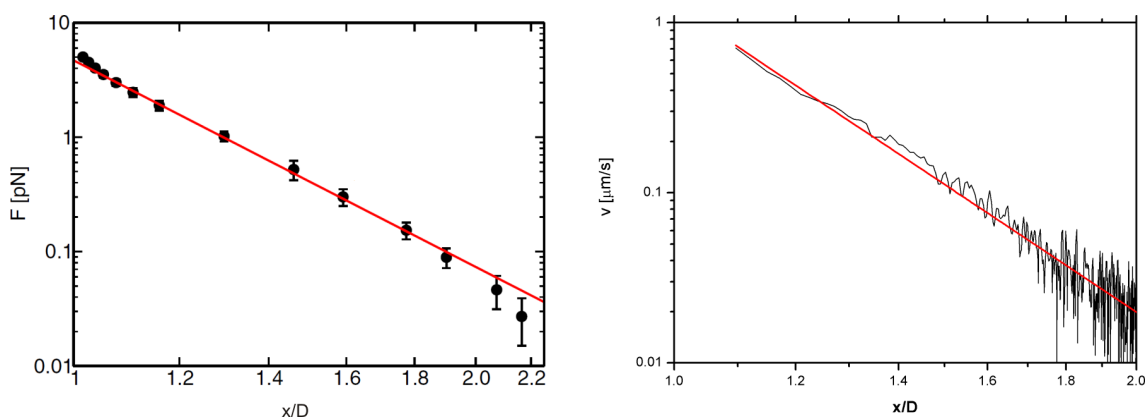
V statičnih meritvah meddelčne sile smo TK odbojno silo uravnotežili z magnetno privlačno silo (6.7), ki jo je induciralo vrteče magnetno polje v ravnini delcev. Pri različnih velikostih magnetnega polja smo izmerili meddelčno razdaljo, na kateri sta se kroglici ustalili, in iz tega izračunali velikost TK odbojne sile. Med ponavljanjem meritev (enkrat smo magnetno polje povečevali, drugič zmanjševali) sta bili kroglici pri danem magnetnem polju vedno na isti razdalji, kar dokazuje, da se direktorsko polje okrog kroglic s spreminjanjem meddelčne razdalje spreminja zvezno in reverzibilno.

Statična odbojna TK sila v odvisnosti od normirane meddelčne razdalje je prikazani na sliki 6.6. Izmerkom se lepo prilagaja izraz (6.11) z vrednostjo $C_F = 4.69(1 \pm 0.18)$ pN. Odstopanja pri majhnih razdaljah so pričakovana, saj izraz drži samo za delce, ki so dovolj narazen. Odstopanje pri velikih razdaljah je posledica ograjenosti TK.

Odvisnost dinamične odbojne TK sile od meddelčne razdalje smo določili iz hitrosti oddaljevanja delcev. S privlačnim magnetnim poljem smo kroglici potegnili skupaj, nato pa polje izklopili, tako da je nanju delovala samo še odbojna TK sila, ki ju je potiskala narazen. Odboj je uravnotežila sila upora kroglice,

$$F_{LC}(x) = \gamma_{eff}v(x). \quad (6.12)$$

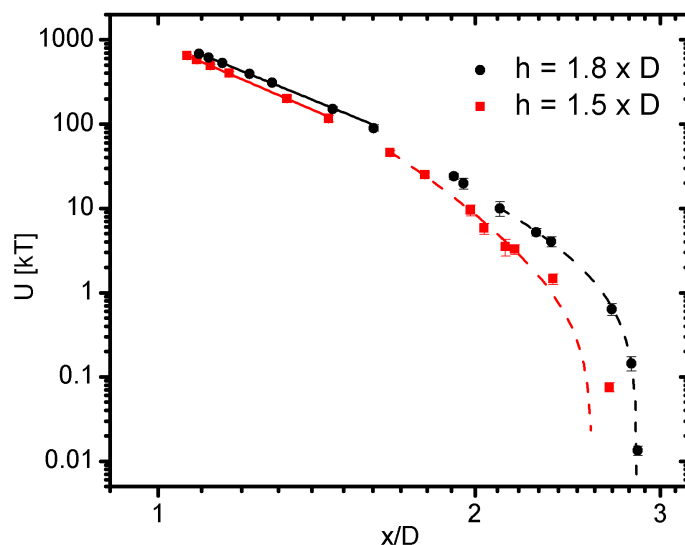
Iz poteka $v(x)$ (slika 6.6) smo ugotovili, da ima dinamična TK sila enako odvisnost



SLIKA 6.6: *Levo*: Meddelčna TK sila v odvisnosti od normirane meddelčne razdalje x/D . Rdeča črta je prilagoditev potenčne odvisnosti $1/(x/D)^6$ izmerkom. Odstopanje od nje pri majhni razdalji je pričakovano, saj 6.11 drži samo za delce, ki so dovolj narazen. Odstopanje pri velikih razdaljah je posledica ograjenosti TK. *Desno*: Hitrost oddaljevanja delcev v odvisnosti od normirane meddelčne razdalje x/D . Delca narazen potiska TK odbojna sila. Rdeča črta je prilagoditev funkcije $v(x) \propto 1/x^6$ izmerkom.

od razdalje kot statična sila, torej $1/x^6$. Efektivni koeficient upora γ_{eff} je neodvisen od razdalje.

Vpliv ograjenosti TK na meddelčno interakcijo smo preučevali v različno debelih celicah, v katerih smo z zgoraj opisano metodo natančno merili statično odbojno TK silo. Izmerjene odvisnosti sile od meddelčne razdalje smo nato numerično integrirali, da smo dobili meddelčno potencialno energijo $U(x)$. Za dve različni debelini vzorcev h je prikazana na sliki .



SLIKA 6.7: Meddelčni potencial v odvisnosti od normirane meddelčne razdalje x/D pri dveh različnih debelinah celice h . Nepretrgane črte prikazujejo potenčno odvisnost pri malih razdaljah, črtkane pa eksponentno pojemanje pri večjih razdaljah.

Izmerjenim vrednostim potenciala je možno pri majhnih meddelčnih razdaljah ($x \leq 0.9h$) prilagoditi potenčno odvisnost $U(x) = C/(x/D)^\beta$ s koeficientoma

$\beta = 5.1(1 \pm 0.05)$ pri $h = 1.8 \times D$ in $\beta = 5.4(1 \pm 0.10)$ pri $h = 1.5 \times D$, kar je konsistentno z izrazom (6.7). Pri večjih meddelčnih razdaljah, ko je razdalja med površinama kroglic primerljiva z debelino celice ($x \geq 1.2h$) pa parski potencial eksponentno pojema, $U = c_2 \exp(-x/\lambda)$. Izmerjeni karakteristični dolžini sta $\lambda = 0.18(1 \pm 0.15)h$ pri $h = 1.8 \times D$ in $\lambda = 0.14(1 \pm 0.20)h$ pri $h = 1.5 \times D$. Elektrostatska potencialna energija dveh kvadrupolov med prevodnima ploščama za velike razdalje eksponentno pojema z karakteristično dolžino $\lambda = 0.16h$, kar je izvrstno ujemanje z izmerjenimi dolžinama.

Vzrok za eksponentno pojemanje parskega potenciala pri večjih razdaljah je ograženost TK. Ko postane meddelčna razdalja primerljiva z debelino celice, močno sidranje TK na njenih stenah relativno zmanjša vpliv ene kroglice na direktorsko polje na mestu druge kroglice. Interakcija je "zasenčena" in z razdaljo pojema eksponentno s karakteristično dolžino, ki je sorazmerna debelini celice.

6.4 Samourejanje superparamagnetnih koloidov v magnetnem polju

Eden izmed pomembnih problemov fizike mehke snovi je povezava med meddelčnim interakcijskim potencialom in večdelčno strukturo, ki jo tak potencial stabilizira. Tematika je posebno zanimiva s stališča samosestave (self-assembly), procesa v katerem se gradniki sistema (atomi, molekule, koloidni delci ali drugi osnovni gradniki) spontano organizirajo v večje urejene in/ali funkcionalne večdelčne strukture [14, 15]. Obliko končnih makroskopskih struktur določajo meddelčne interakcije na mikroskopski skali.

Povezave med meddelčno interakcijo in posledičnimi večdelčnimi strukturami v atomskih in molekulskih sistemih običajno študirajo teoretično in z numeričnimi simulacijami, neposrednih eksperimentov pa ni, saj je spreminjanje medatomskih interakcij nemogoče. Približno pred tremi desetletji so za *koloidne* ugotovili, da so odličen model kondenzirane snovi. Koloidi so disperzije trdnih delcev, kapljic ali plinskih mehurčkov (značilne velikosti od nekaj nm do nekaj $10 \mu m$) v gostiteljskem mediju. Koloidni sistemi so zaradi velikosti primerni za opazovanje, hkrati pa je možno spreminjati njihove lastnosti, npr. z uporabo koloidnih delcev druge velikosti, spremembo gostiteljskega medija ali vklopom dodatnega zunanjskega polja (npr. električnega ali magnetnega).

Omejitev koloidnih sistemov je krogelna oblika večine komercialno dostopnih monodisperznih koloidnih delcev, kar se odraža v *izotropnem* meddelčnem interakcijskem potencialu. Najpogostejši urejeni strukturi sta zato heksagonalna mreža v dveh dimenzijah in ploskovno centrirana kubična mreža v treh dimenzijah [17, 18]. Obstajata dve poti do kompleksnejših koloidnih struktur: (i) z *anizotropnimi* meddelčnimi interakcijami, kar se doseže z obdelavo površin delcev [19], zunanji polji [20], anizotropnim gostiteljskim medijem [3] ali z (ii) *izotropnimi* meddelčnimi interakcijami z radialnim profilom, ki je bolj zapleten kot potenčni zakon $r^{-\beta}$, ki običajno nastopa v potencialih. Preprost primer take interakcije je izotropni potencial z radialnim profilom z dvema dolžinskima skalama, kombinacijo trdega jedra in mehkejšega odbojnega dela ("hard-core/soft-shoulder"). Numerične simulacije

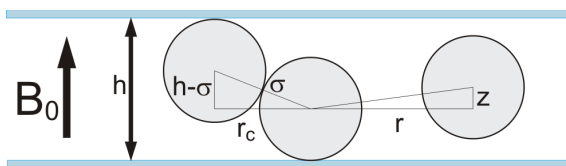
napovedujejo, da taka parska interakcija ustvari množico mezofaz [21, 22, 23, 24] med tekočino in tesno zloženo kristalno mrežo.

Z uporabo magneto-optične pincete smo v sistemu superparamagnetnih koloidnih delcev ustvarili različne tipe interakcijskih potencialov in opazovali kakšne urejene faze stabilizirajo. Kombinacija statičnega magnetnega polja in geometrijske ograjenosti ustvari izotropen parski potencial, čigar profil v smeri prečno na polje določa debelina vzorca. Pri kritični debelini dobimo kombinacijo trdega jedra in zmehčanega odbojnega potenciala, ki stabilizira nove faze.

Nato smo se osredotočili na izotropne potenciale, ustvarjene z vrtenjem magnetnega polja. Zanimivo interakcijo dobimo, če magnetno polje precesira po plašču stožca z "magičnim" kotom $\theta_p = 54.7^\circ$ ob vrhu osnega preseka. Člen $1/r^3$ v dipolni interakciji med induciranimi dipolnimi momenti delcev izgine, toda zaradi vplivov lokalnega polja je parski potencial izotropno privlačen. Odvisno od gostote sistema se pri takem potencialu samosestavijo različne oblike struktur.

Eksperimentalne podrobnosti

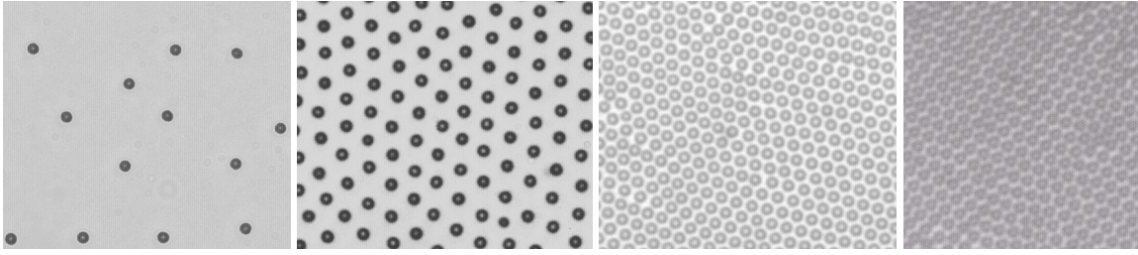
V poskusih smo uporabili superparamagnetne kroglice s premerom $\sigma = 1.05 \mu\text{m}$ (*Dynabeads, MyOne Carboxy*), z magnetno pinceto pa smo ustvarili zunanje magnetno polje, ki je induciralo meddelčne potenciale (slika 6.8). Tipične velikosti polj v eksperimentih so bile nekaj mT, tako da je bila interakcijska energija dveh dotikajočih kroglic, postavljenih v smeri zunanjega statičnega magnetnega polja od nekaj 10- do nekaj 100-krat večja od termične energije $k_B T$. Osredotočeni smo bili na ravnovesne oz. kvaziravnovesne večdelčne strukture, ustvarjene z različnimi tipi meddelčnih potencialov. Zaradi nizke "temperature" sistema so se strukture vzpostavile v nekaj sekundah po vklopu magnetnega polja.



SLIKA 6.8: Shema eksperimentalne celice debeline h s koloidnimi kroglicami premera σ . Zunanje magnetno polje \mathbf{B}_0 je pravokotno na ravnino vzorca.

S statičnim magnetnim poljem je možno doseči izotropen meddelčni potencial, če je polje usmerjeno pravokotno na ravnino vzorca. Med delci deluje odbojna dipolna interakcija (6.5), ki povzroči njihovo razporeditev v heksagonalno mrežo. Na sliki 6.9 so prikazane tipične faze 2D sistema pri konstanti velikosti odbojne interakcije za različne površinske gostote¹ sistema. Pri nizki gostoti je sistem v tekoči fazi, z višanjem gostote pa se delci uredijo v odprto in nato v tesno zloženo heksagonalno mrežo.

¹Površinska gostota sistema pove delež površine, prekrit z delci: $\eta = \pi\sigma^2 n/4$, kjer je n številčna gostota delcev (število delcev/površino).



SLIKA 6.9: Slike tipičnih faz 2D sistema superparamagnetnih koloidnih kroglic v magnetnem polju, pravokotno na ravnino vzorca. Pri nizki gostoti je sistem v tekoči fazi (levo). Pri višjih gostotah nastane odprta oz. tesno zložena heksagonalno mrežo.

Statično magnetno polje v kvazi-2D sistemu

S statičnim pravokotnim magnetnim poljem in ustrezno geometrijo eksperimentalne celice je možno doseči zmehčano izotropno odbojno interakcijo. Če je debelina vzorca malo večja od premera kroglic, njihovi središči nista več strogo omejeni na eno ravnino. Posledično je pri manjših meddelčnih razdaljah parska interakcija manj odbojna kot pa v primeru, če se delca nahajata v isti ravnini.

Interakcijska energija dveh delcev se lahko zapiše kot

$$E(r, z) = K \frac{r^2 - 2z^2}{(r^2 + z^2)^{5/2}}, \quad (6.13)$$

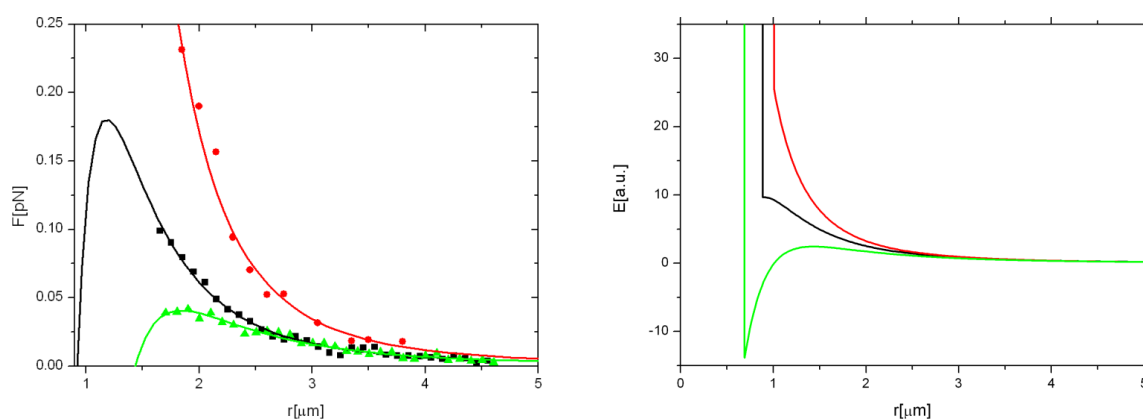
kjer sta r in z horizontalna in vertikalna komponenta razdalje med središčema obeh kroglic (slika 6.8), $K = \frac{\pi\sigma^6\chi^2 B^2}{144\mu_0}$ pa interakcijska konstanta. Obliko meddelčnega potenciala neposredno določa debelina celice. Če je ta enaka premeru delcev, $h = \sigma$, ti interagirajo dipolno $E = K/r^3$, pri večjih debelinah celice je omogočen $z > 0$ (za dva delca je energetsko najugodnejše, da je en pri spodnji steni celice, drug pa pri zgornji), kar zmanjša meddelčni odboj oz. lahko vodi do privlaka pri majhnih meddelčnih razdaljah. Pri kritični debelini celice

$$h_m = \sigma(1 + 1/\sqrt{5}) \approx 1.447\sigma \quad (6.14)$$

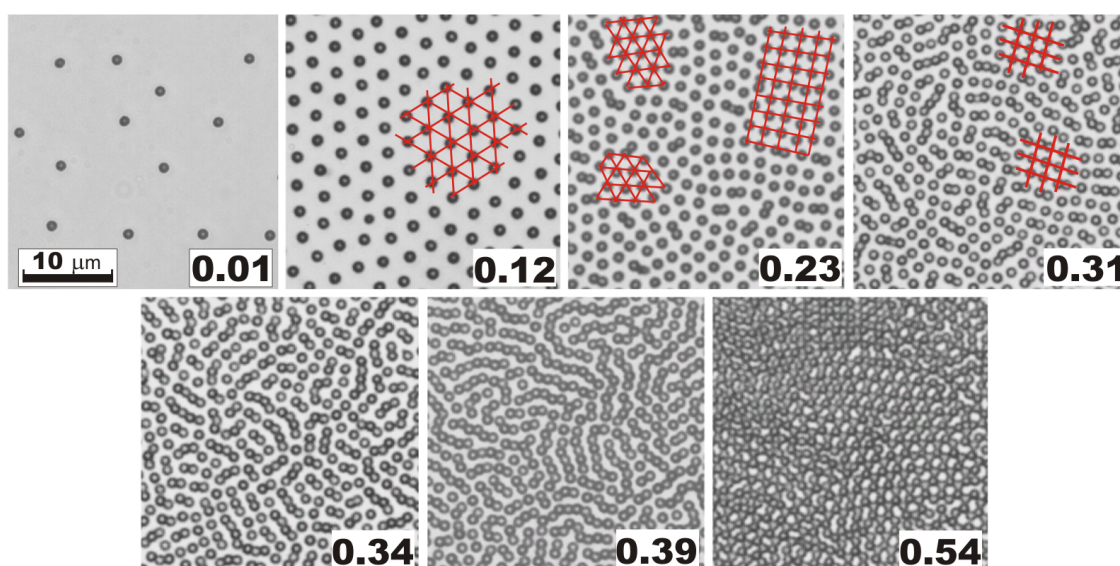
meddelčna interakcija preide iz odbojne (pri vseh meddelčnih razdaljah) v privlačno (pri malih meddelčnih razdaljah). Z optično pinceto smo izmerili meddelčno interakcijo v različno debelih celicah h . Na sliki 6.10 so prikazani izmerki sile in izračunani parski potenciali, ki so kombinacija trdega jedra, čigar doseg je definiran s premerom kroglic, in zmehčanega odbojnega dela pri $h < h_m$ oz. privlačnega dela pri $h > h_m$.

V sistemu z zmehčanim odbojnim potencialom (pri kritični debelini $h = h_m$) smo opazovali urejene mezofaze, ki nastanejo pri različnih površinskih gostotah sistema. V vzorcu smo poiskali območje ustrezne debeline, nato pa s segrevanjem vzorca s pomočjo optične pincete lokalno nakopičili več kot 10^4 delcev. Po vklopu prečnega magnetnega polja se je zaradi odbojne interakcije površinska gostota sistema zmanjševala od začetne $\eta > 0.6$ do $\eta \approx 0.01$.

Na sliki 6.11 so prikazane mezofaze, ki se porajajo pri različnih površinskih gostotah sistema η . Pri zelo visokih gostotah ($\eta \geq 0.5$) nastanejo domene satovja in goste kvadratne mreže. Z nižanjem površinske gostote ($\eta = 0.39$) se gosta mreža



SLIKA 6.10: *Levo*: Izmerjeni profili komponente meddelčne sile v ravnini vzorca za 3 različne debeline celice: odboj r^{-4} v tanki celici ($h \approx \sigma$; rdeči krogi), zmehčan odboj ($h \approx h_m$; črni kvadrati) in privlačna interakcija v debeli celici ($h > h_m$, zeleni trikotniki). Nprekinjene črte prikazujejo teoretično odvisnost sile za $h = \sigma$, $h = 1.46\sigma$ in $h = 1.72\sigma$. *Desno*: Parski potenciali: dipolni odboj ($h \approx \sigma$; rdeče), zmehčan odboj ($h \approx h_m$; črno) in privlačen potencial v debeli celici ($h > h_m$, zelena).



SLIKA 6.11: Slike reprezentativnih mezofaz pri različnih površinskih gostotah η . Na nekaterih slikah so z rdečo poudarjene urejene strukture kroglic.

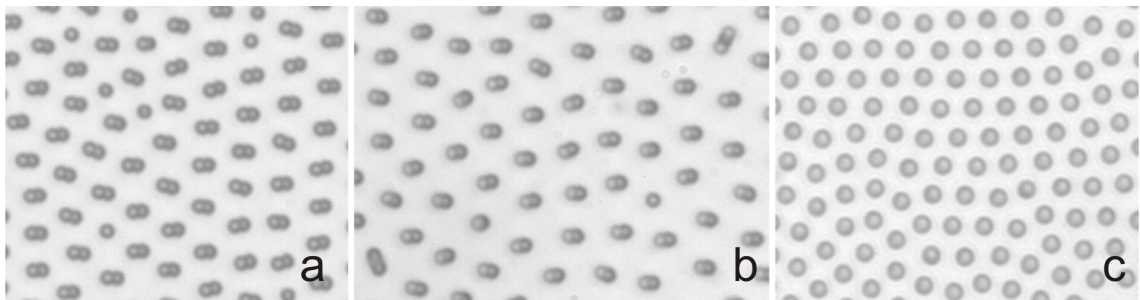
razširi v labirintno strukturo enojnih verig iz dotikajočih kroglic. Pri nižji gostoti ($\eta = 0.34$) so stabilne krajše verige, ki so lokalno poravnane. Pri $\eta = 0.31$ opazimo koeksistenco razširjene kvadratne mreže in kratkih verig, večinoma dimerov in trimerov. Ti z nižanjem površinske gostote ($\eta = 0.23$) razpadejo na posamezne kroglice, ki se razporedijo v razširjeno heksagonalno ali kvadratno mrežo. Ko je gostota dovolj majhna, sistem preide v razširjeno heksagonalno fazo ($\eta = 0.12$) in na koncu v tekočo fazo ($\eta = 0.01$).

Mezofaze, opažene v eksperimentu, so podobne rezultatom numeričnih simulacij [76, 21, 22]. Čeprav so v nekaterih simulacijah za potencial uporabljene močno idealizirane kombinacije trdega jedra in mehkega odbojnega dela, je ujemanje z

eksperimentalnimi fazami presenetljivo dobro, iz česar sklepamo, da so strukture in mehanizmi nastanka precej robustni.

Statično magnetno polje v 3D sistemu

Če je širina celice večja od kritične širine $h_m \approx 1.447\sigma$, pravokotno magnetno polje povzroči privlačen potencial med delci (slika 6.10). Če je površinska gostota sistema majhna, so stabilni parčki kroglic. Ti se postavijo navpično (v smeri magnetnega polja), če le imajo dovolj prostora ($h > 2\sigma$). Med parčki ddeluje odbojna sila, tako da se razporedijo v heksagonalno mrežo (slika 6.12(c)). Če je debelina celice manjša, a še vedno nad kritično debelino h_m , so parčki nagnjeni ((a), (c)).



SLIKA 6.12: Slike koloidnih mezofaz pri nizki gostoti sistema v treh različnih debelinah celice h (a) $h \approx h_m$; zaradi rahlega privlaka so parčki stabilni kljub nizki gostoti (b) $h \approx 1.5\sigma$. (c) Celica je dovolj debela, da se par postavi pokončno v smer magnetnega polja. Izotropni odboj med pari povzroči razporeditev v heksagonalno mrežo.

Pri večjih gostotah sistema kroglice ne morejo ostati v ločenih skupkih, zato se tvorijo enojne verige, ki so sestavljene iz dotikajočih se kroglic. Minimizacija energije povzroči, da se npr. prva kroglica v verigi dotika zgornje stene celice, druga spodnje stene, tretja spet zgornje in tako naprej. Na sliki 6.13 so prikazani trije primeri gostih sistemov pri različnih debelinah celic. Pri debelini pod dvema premeroma kroglic ($h = 1.6\sigma$ na levi in $h = 1.8\sigma$ na srednji sliki) so stabilne dolge enojne verige kroglic z lepo vidno izmenjujočo sestavo gor-dol, pri večji debelini pa se vzpostavijo pari v smeri magnetnega polja ($h = 2.1\sigma$ na desni sliki). Odboj med njimi jih razporedi v heksagonalno mrežo z mrežno razdaljo, ki je odvisna od gostote sistema. Če je mreža tesno zložena, se pri povečanju gostote sistema začnejo vzpostavljati "defekti", kjer se pokončni parčki povežejo z dodatno skupno kroglico.

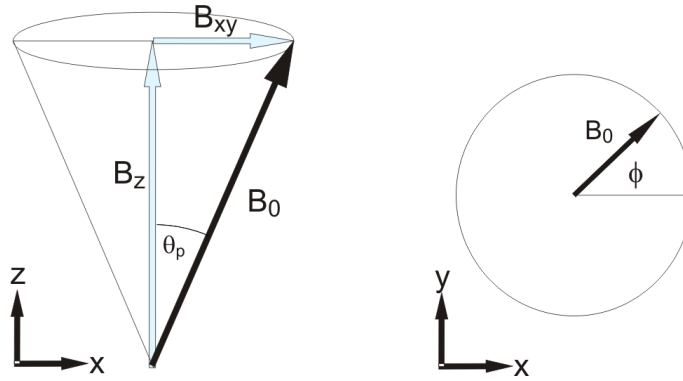
Urejene strukture smo obravnavali tudi z numeričnim izračunom energij. Izračun pojasni stabilnost enojnih verig in pokaže, da se verige med seboj odbijajo, oboje pa je v skladu z opaženimi mezofazami pri nizkih ter visokih gostotah sistema.

Vrteče nagnjeno magnetno polje

Vrtenje zunanjega magnetnega polja omogoča ustvarjanje še kompleksnejših interakcijskih potencialov. V ravnini vrteče magnetno polje med delci inducira izotropno privlačno interakcijo (6.7) in z navorom deluje na skupke delcev. Pojav je dobro znan [81, 82, 83] in je praktično uporaben je za samosestavo in vrtenje mikročr-palk iz koloidnih delcev [84, 85]. Skupna značilnost omenjenih eksperimentov je



SLIKA 6.13: Tipične mezofaze za različne debeline celice h pri veliki gostoti sistema. *Leva*: $h \approx 1.6\sigma$, stabilne strukture so enojne verige. *Sredina*: $h \approx 1.8\sigma$, enojne verige z malim številom razvejišč. *Desna*: $h \approx 2.1\sigma$. Navpični parčki kroglic se zložijo v heksagonalno mrežo. Rdeč krog označuje dva "defekta", kjer so tri parčki povezani s skupno kroglico.



SLIKA 6.14: Skupno zunanje magnetno polje $\mathbf{B}_0 = \mathbf{B}_z + \mathbf{B}_{xy}$ precesira po obodu stožca z vršnim kotom θ_p . Azimut ϕ je kot med ravninsko komponento polja in smerjo osi x .

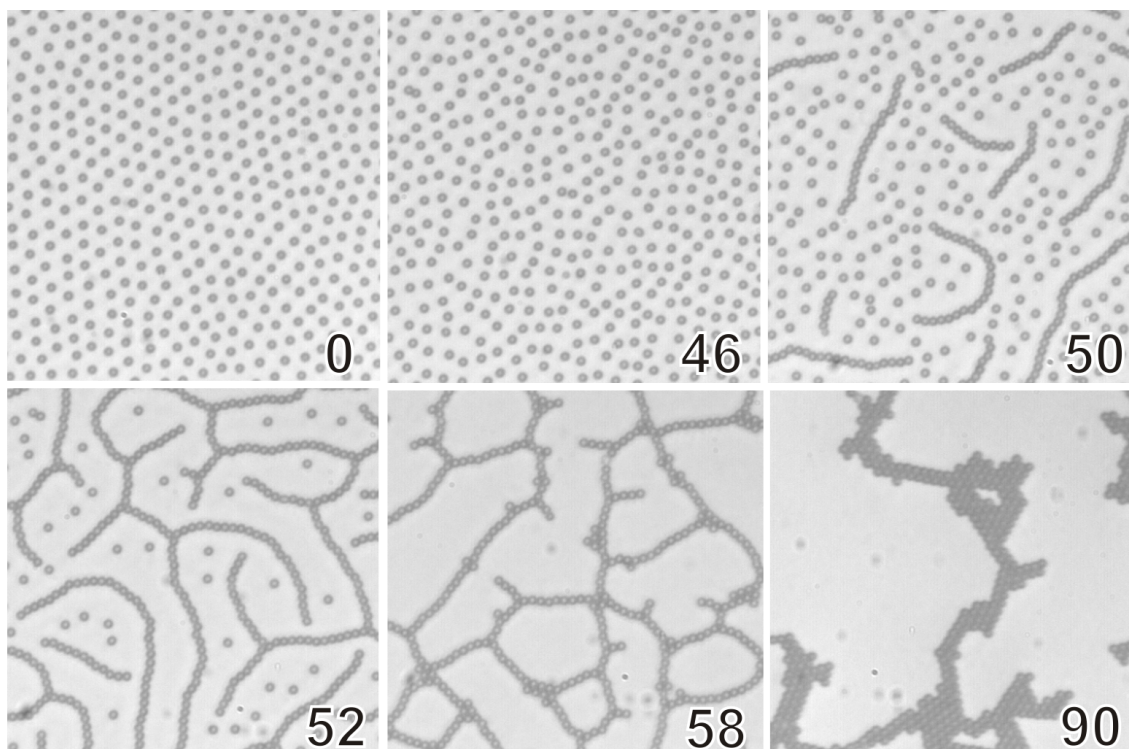
vrtenje polja v eno smer, kar povzroči vrtenje večdelčnih struktur. Z našim sistemom lahko magnetno polje izmenično vrtimo - torej en obrat v smeri urinega kazalca, naslednji v obratni smeri, tako da na strukture efektivno ne deluje magnetni. Pod vplivom nastale izotropno privlačne magnetne interakcije delci v dveh dimenzijah tvorijo skupke tesno zložene heksagonalne mreže.

Če je vklopljena kombinacija navpičnega statičnega polja B_z in v ravnini vrtečega polja B_{xy} , vektor celotnega magnetnega polja $\mathbf{B}_0 = B_0(\sin \theta_p \cos \phi, \sin \theta_p \sin \phi, \cos \theta_p)$ precesira po obodu stožca z vršnim kotom θ_p (slika 6.14), ki je odvisen od relativne velikosti ravninske $B_{xy} = \sqrt{B_x^2 + B_y^2}$ in navpične komponente polja B_z :

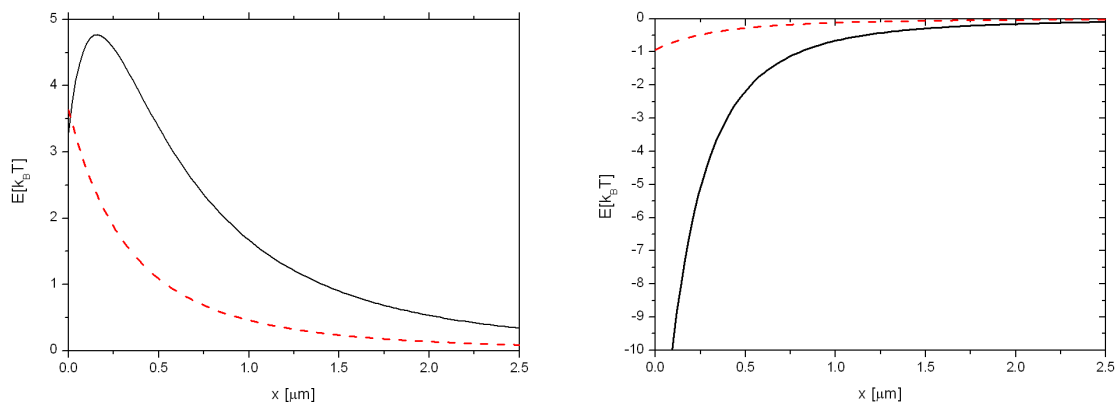
$$\tan \theta_p = \frac{\sqrt{B_x^2 + B_y^2}}{B_z}. \quad (6.15)$$

Meddelčno interakcijo je možno kontrolirati s spreminjanjem kota θ_p . Pri navpičnem polju, $\theta_p = 0$, je interakcija izotropno odbojna, druga skrajnost, pri $\theta_p = 90^\circ$, je izotropno privlačna interakcija med delci v 2D sistemu. V območju, ko sta velikosti odboja in privlaka približno enaki, pride do zanimivih pojavov. Na sliki 6.15 so predstavljene stabilne faze, ki v sistemu nastanejo pri različnih kotih θ_p .

Čeprav je pri $\theta_p < 54.7^\circ$ odbojna komponenta dipolne interakcije močnejša od privlačne se koloidni delci združijo v stabilno enojno verigo, kar je jasen znak privlaka



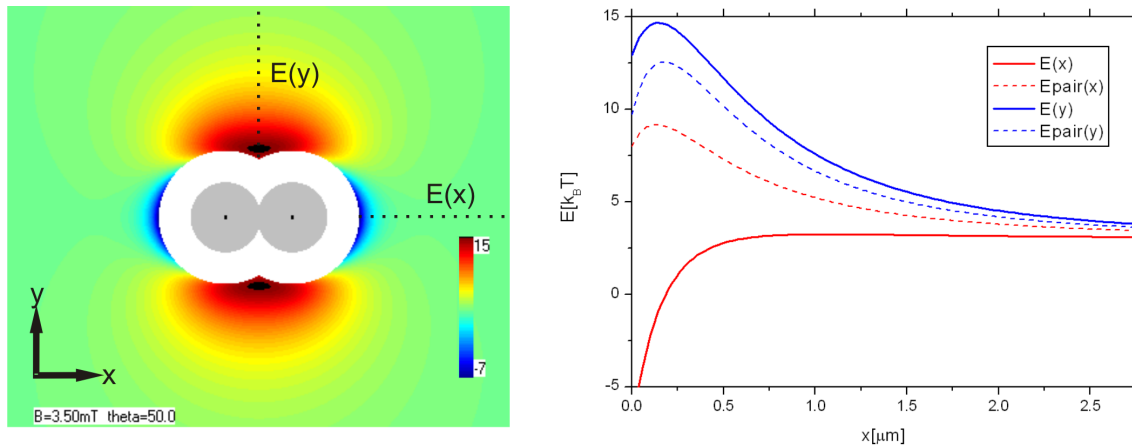
SLIKA 6.15: Slike 2D sistema z nizko gostoto delcev v magnetnem polju, ki kroži po obodu stožca pri različnih vrednostih vršnega kota θ_p (označen).



SLIKA 6.16: Energija dveh delcev v krožečem magnetnem polju kot funkcija razdalje med njima pri $\theta_p = 50^\circ$ (levo) in $\theta_p = 56^\circ$ (desno). S črno je narisana prava energija, črtkano pa dipolni potencial brez popravkov zaradi lokalnega polja.

med njimi. Vzrok za to je vpliv lokalnega magnetnega polja delcev. To se najlažje pojasni na paru dveh delcev: ko krožeče magnetno polje kaže v smeri para, se lokalno magnetno polje inducirane dipola prvega delca sešteje z zunanjim magnetnim poljem, kar povzroči večjo magnetizacijo drugega delca. Ko pa magnetno polje kaže pravokotno na smer para, pa lokalno polje prvega delca zmanjša magnetno polje na mestu drugega delca, tako da je njegova magnetizacija manjša. Ta pojav znatno spremeni parski potencial, kar je za dva kota θ_p prikazano na sliki 6.16.

Poleg vpliva lokalnega polja so v takem sistemu pomembni tudi večdelčni prispevki



SLIKA 6.17: Izračun energije treh delcev v xy -ravnini *Levo*: Potencial okoli para delcev pri $\theta_p = 50^\circ$ in $B_0 = 3.5$ mT. *Desno*: Energija sistema v odvisnosti od razdalje med parom in testnim delcem za dve posebni smeri (črtkani na levi sliki): v smeri dolge osi ($E(x)$, modra) in kratke osi para ($E(y)$, rdeča). Črtkane krivulje predstavljajo energijo istega sistema, izračunano kot vsoto treh parskih energij.

- v sistemu več delcev energija ni enaka vsoti posameznih parskih energij, kar se lepo ilustrira že v sistemu treh delcev. Na sliki 6.17 je z različnimi barvami prikazana energija sistema treh delcev: na sredini je fiksni par delcev (sivo), testni delec pa se premika po xy -ravnini. Barva v vsaki točki slike simbolizira energijo sistema, če se središče tretjega delca nahaja v tisti točki. V belo območje tretji delec ne more zaradi trdega jedra.

Par deluje privlačno v smeri dolge osi, v smeri kratke osi pa odbojno. Taka oblika potenciala povzroči nastanek verig pri nizkih θ_p . Pri višjih θ_p privlačen potencial postane še močnejši, odboj v prečni smeri izgine, tako da se verige združijo v mrežo (slika 6.16). Tovrsten potencial je uporaben za stabilizacijo superstruktur iz koloidnih delcev. Nekaj primerov takih struktur, ki smo jih iz posameznih kroglic sestavili s pomočjo optične pincete, je prikazano na sliki 6.18.

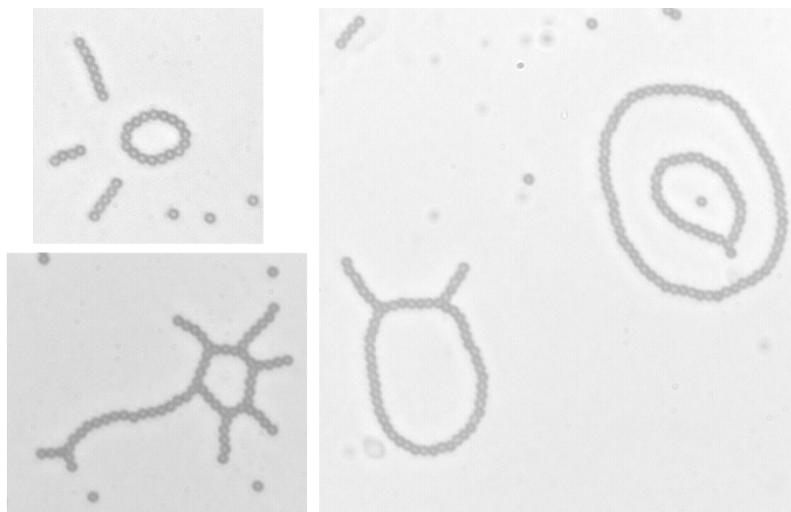
Vrteče magnetno polje pri magičnem kotu

Če je vršni kot stožca po katerem precesira polje enak magičnemu kotu $\theta_m = \arccos(1/\sqrt{3}) \approx 54.7^\circ$, v meddelčni dipolni interakciji člen z odvisnostjo $1/r^3$ izgine. Najnižji neničelni popravek k energiji para dveh induciranih dipolov v magnetnem polju znaša

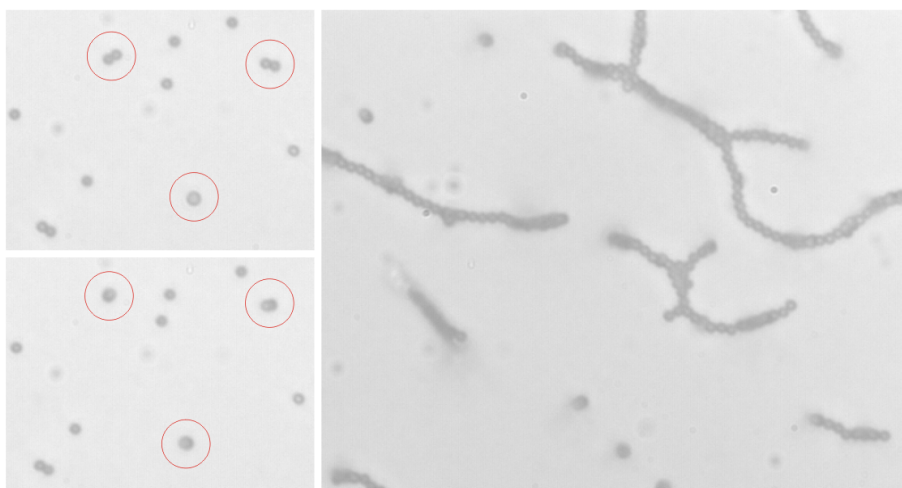
$$\bar{E} = -\frac{\chi^3 V^3 B_0^2}{16\pi^2 \mu_0} \frac{1}{r^6}. \quad (6.16)$$

Ta interakcija je prostorsko izotropno privlačna, zato se v nadaljevanju osredotočimo na 3D sisteme s to interakcijo. Zaradi privlaka pride do združevanja posameznih kroglic v pare, ki so orientirani v vse smeri (slika 6.19). Sila para delcev je privlačna v smeri dolge osi, v prečni smeri pa je doseg privlaka približno $0.5 \mu\text{m}$, pri večjih razdaljah pa je rahel odboj. Taka interakcija privede do rasti verig.

Z vsakim dodatnim delcem v verigi se prečni odboj zmanjša in tako se pri dolžini okoli 8 delcev ali več lahko nov delec verigi pridruži tudi od strani. Tak ravninski



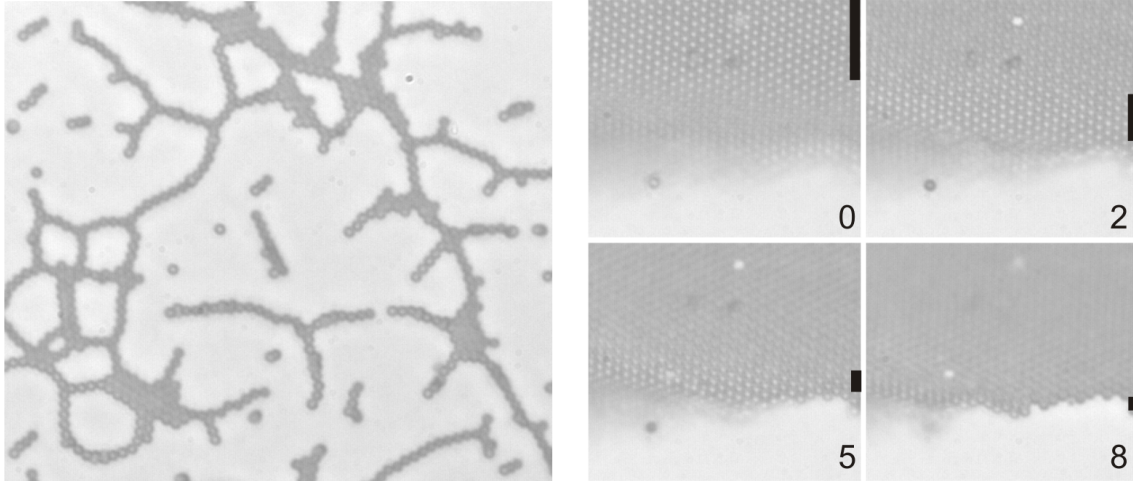
SLIKA 6.18: Stabilne koloidne superstrukture, zgrajene z optično pinceto ($\theta_p = 53^\circ$, $B_0 = 3.5$ mT).



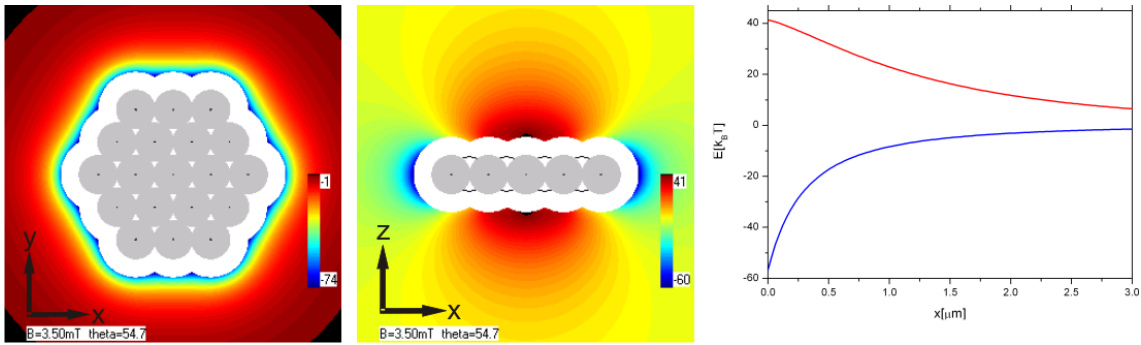
SLIKA 6.19: Slike samosestavljenih verig iz koloidnih delcev pri rotaciji magnetnega polja $B_0 = 3.5$ mT pri magičnem kotu. *Levo*: Dve zaporedni sliki redkega sistema. Zaradi izotropne narave interakcije so pari kroglic stabilni ne glede na njihovo orientacijo. *Desno*: Po dolgem času se v redkem sistemu stabilizirajo enojne in dvojne verige delcev.

trikotnik delcev (2 iz verige + 1 dodatni) povzroči privlačni potencial okoli njega in predstavlja nukleacijsko jedro za rast 2D struktur. Pri srednji gostoti sistema nastane kombinacija 2D heksagonalno zloženih skupkov, povezanih z enojnimi verigami delcev (slika 6.20 levo). Pri visoki gostoti sistema se delci zložijo v tesno zloženo heksagonalno "plahto" poljubne orientacije, npr. na desni sliki 6.20 je "plahta" zaradi sedimentacije na dnu celice, njen rob pa je zavihan navzgor in seže $8 \mu\text{m}$ nad dnom.

Nastanek koloidnih "plaht" je energetsko ugoden proces. Na sliki 6.21 je obravnavan ravninski kristal, sestavljen iz 19 tesno zloženih delcev. V njegovi ravnini je potencial privlačen, tako da pritegne morebitne okoliške proste delce in tako raste. V pravokotni smeri je potencial odbojen kar preprečuje rast v tretjo dimenzijo.



SLIKA 6.20: Heksagonalni tesno zloženi 2D kristali ($\theta_p = \theta_m$, $B_0 = 3.5$ mT). *Levo*: Na mestih večje lokalne gostote delcev nastanejo 2D kristaliti. *Desno*: Slike samosestavljene koloidne "plahte" pri različnih goriščnih ravninah mikroskopa. Številka pomeni višino fokusa v μm . Črni trakovi poudarjajo oster del slik.



SLIKA 6.21: Tesno zložen 2D kristal iz 19 delcev $\theta_p = \theta_m$, $B_0 = 3.5$ mT. *Levo*: Potencial v xy ravnini. *Sredina*: Potencial v prečni ravnini xz . *Desno*: Energija dodatnega delca v odvisnosti od razdalje od kristala v smeri x (modro) in v prečni smeri z (rdeče).

6.5 Viskoelastičnost bakterijskih mrež

Ena izmed pomembnih snovnih lastnosti je strižni modul, ki je v kompleksnih materialih ponavadi frekvenčno odvisen. Meritev viskoelastičnih lastnosti se tradicionalno opravi z mehničnimi reometri, ki na merjenec delujejo z oscilirajočo strižno deformacijo $\gamma(t) = \gamma_0 \sin(\omega t)$ in merijo napetost merjenca. Če je amplituda deformacije majhna, je napetost $\sigma(t)$ proporcionalna deformaciji

$$\sigma(t) = \gamma_0 [G'(\omega) \sin(\omega t) + G''(\omega) \cos(\omega t)]. \quad (6.17)$$

Tu je $G'(\omega)$ odziv v fazi z deformacijo, imenovan elastični modul, $G''(\omega)$ pa odziv snovi v fazi s hitrostjo deformacije, imenovan viskozni modul. Frekvenčno odvisen strižni modul (imenovan tudi viskoelastični modul) [89] je definiran kot

$$G(\omega) = G'(\omega) + iG''(\omega). \quad (6.18)$$

V zadnjih dveh desetletjih se je razvilo ogromno tehnik za merjenje materialnih lastnosti na mikroskopski velikostni skali s skupnim imenom *mikroreologija* (pregled v [90, 91, 92]). V primerjavi s klasično reologijo ima mikroreologija (MR) več prednosti: potrebna je samo majhna količina vzorca ($1 \mu\text{l}$ je že dovolj), možna je meritev nehomogenih okolij (npr. notranjosti celice), dostopne so višje frekvence (do 10^5 Hz).

MR tehnike se delijo v dva razreda: *pasivne* in *aktivne*. Pri pasivnih tehnikah se spremlja termične fluktuacije sond, ponavadi inertnih kroglic premera od nekaj deset nanometrov do nekaj mikronov, ki so vložene v merjeni material. Iz njihove difuzije se izračuna linearni kompleksni strižni modul [26, 27]. Aktivna MR je podobna klasični reologiji, saj se na sodno deluje s silo, pri tem pa se meri deformacijo medija. Za prvi primer aktivne MR se šteje Freundlichovo [28] manipulacijo magnetnih kroglic z zunanjim magnetnim poljem pred več kot 80 leti. Danes se za aktivno MR uporabljajo mikropipete [29], mikroskopi na atomsko silo [30], optične pincete [31] in mikroreometri z magnetnimi kroglicami [32, 33, 34].

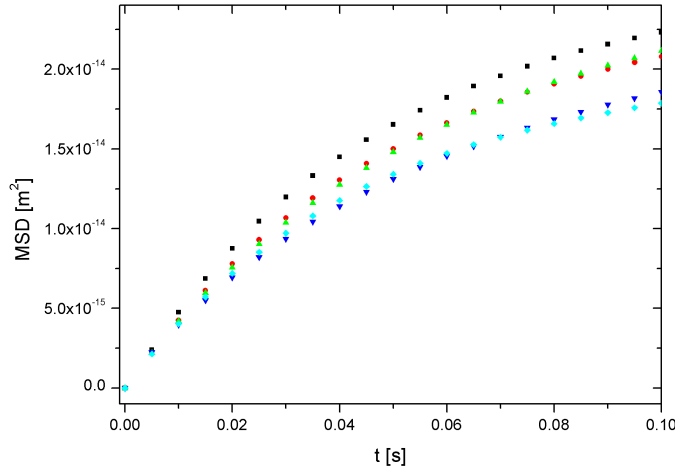
Znotraj obeh razredov obstaja še nadaljnja delitev glede na število uporabljenih sond na *enodelčno* MR, kjer se viskoelastičnost določi iz gibanja ene same sonde in na *dvodelčno* MR, pri kateri se analizira korelirano gibanje dveh (ali več) sond. Dvodelčna MR omogoča meritev viskoelastičnih lastnosti na večjih dolžinskih skalah, kar je prikladno v sistemih, ki so nehomogeni na velikostni skali posamezne sonde.

Optična pinceta je uporabno orodje za MR meritve. Pri enodelčni pasivni MR je sonda ujeta v nepremični optični pasti, njene fluktuacije pa dajejo informacijo o mehanskih lastnostih snovi. Če je snov pretrda in termične fluktuacije ne povzročijo zaznavne deformacije, se lahko uporabi enodelčna aktivna MR, pri kateri je sonda ujeta v sinusno premikajoči optični pasti [31, 35]. Kompleksni viskoelastični modul merjene snovi je izračunan iz odziva sonde na gibanje pasti. Pri dvodelčni aktivni MR [36] se uporabljata dve optični pasti, v vsaki pa je ujeta sonda. S harmoničnim spreminjanjem lege delca v prvi (trdi) pasti se aktivno deformira medij, delec v drugi (šibkejši) pasti pa je indikator deformacije medija na mestu pasti.

V naših meritvah smo kot sonde uporabili kroglice iz silike s premerom $3.22 \mu\text{m}$. Vse MR metode smo testirali v vodi kot primeru vzorca z znano viskoznostjo ($\eta = 9.3 \times 10^{-4}$ Pas pri temperaturi 23°C), nato pa smo z njimi analizirali mehanske lastnosti kompleksnega biološkega vzorca - rastoče bakterijske populacije.

Ko se bakterije znajdejo v hranljivem okolju, se začne proces delitve. Spremembo njihovega števila skozi čas opisuje rastna krivulja, sestavljena iz 4 faz. V adaptivni fazi se bakterije prilagajajo na novo okolje in ne rastejo. Ko se prilagodijo, preidejo v logaritemsko fazo, kjer je rast eksponentna. Bakterijska kultura se znajde v stacionarni fazi, ko začne primanjkovati okoliških hranilnih snovi, nato pa sledi faza odmiranja, ko se njihovo število zmanjšuje zaradi akumuliranih toksinov in pomanjkanja hrane.

Spremljali smo reologijo raztopine bakterijskega seva *Vibrio* sp. DSM 14379 [108]. Vzorca za MR meritve so bili vzeti v adaptivni (vzorec 1), logaritemski (vzorec 2) in stacionarni fazi (vzorec 3). Dodaten vzorec ("samo mreža") smo pripravili iz tretjega vzorca z odstranitvijo bakterij s centrifugo. Merili smo MR celotne bakterijske raztopine, ki sestoji iz gojišča, bakterijskih celic in ekstracelularne matrike (ECM). To sestavlja prepletana mreža vlaknastih beljakovin in dolgih nerazvejanih polisaharidov. Komponente ECM nastanejo v notranjosti bakterijskih celic, nato pa so z



SLIKA 6.22: Enodelčna pasivna MR. Povprečen kvadrat odmika v odvisnosti od časa za rastočo bakterijsko raztopino. Gojišče (črno), vzorec 1 (rdeče), vzorec 2 (zeleno), vzorec 3 (modra), vzorec 3 brez bakterij (svetlomodra).

eksocitozo izločene iz celice, kjer se združijo z obstoječo matriko.

Enodelčna pasivna MR

Pri enodelčni pasivni MR se iz zaporednih leg ujetega delca izračuna povprečen kvadrat odmika (angl. mean square displacement) v času τ . Definiran je z

$$\langle \mathbf{r}^2(\tau) \rangle = \langle |\mathbf{r}(t + \tau) - \mathbf{r}(t)|^2 \rangle. \quad (6.19)$$

Tu je \mathbf{r} položaj delca, oklepaji pa pomenijo povprečenje po celem intervalu meritve. $\langle r^2 \rangle$ in kompleksni viskoelastični modul G povezuje posplošena Stokes-Einsteinova enačba [93]. Če je sonda večja od vseh strukturnih dolžinskih velikostnih skal, v d -dimenzijah velja

$$\tilde{G}(s) = \frac{d k_B T}{3\pi a s \langle \tilde{r}^2(s) \rangle}. \quad (6.20)$$

Tu je s frekvenca v Laplaceovem prostoru, $\langle \tilde{r}^2(s) \rangle$ in $\tilde{G}(s)$ Laplaceovi transformaciji $\langle r^2(t) \rangle$ in $G(t)$. Za primerjavo z rezultati klasične reologije je $\tilde{G}(s)$ pretvorjen v Fourierjev prostor s transformacijo ($s \rightarrow i\omega$).

Če predpostavimo, da sta viskoznost η in elastičnost medija k_m frekvenčno neodvisna, velja

$$G(\omega) = G'(\omega) + iG''(\omega) = \frac{k_m}{6\pi a} - i\omega\eta. \quad (6.21)$$

V vodi smo z enodelčno pasivno MR merili s tremi različno močnimi pastmi: šibko ($k = 0.81 \times 10^{-6}$ N/m), srednjo ($k = 2.0 \times 10^{-6}$ N/m) in trdo ($k = 4.0 \times 10^{-6}$ N/m) ter za viskoznost dobili vrednosti od 8.7×10^{-4} Pas do $\eta = 9.1 \times 10^{-4}$ Pas, kar je malo manj od pričakovane vrednosti. Pri meritvi bakterijskih vzorcev metoda

še posebno pri večjih močeh optičnih pasti ni delovala dobro, saj so močne pasti vase vlekale bakterije, kar je povzročilo artefakte pri meritvi. Povprečne kvadrate odmika smo zato izmerili v šibki pasti (slika 6.22). Izmerjene bakterijske viskoznosti so bile $\eta_M = 10.0 \times 10^{-4}$ Pas, $\eta_{S1} = 12.4 \times 10^{-4}$ Pas, $\eta_{S2} = 14.4 \times 10^{-4}$ Pas, $\eta_{S3} = 16.0 \times 10^{-4}$ in $\eta_{S3'} = 13.8 \times 10^{-4}$ Pas.

Enodelčna aktivna MR

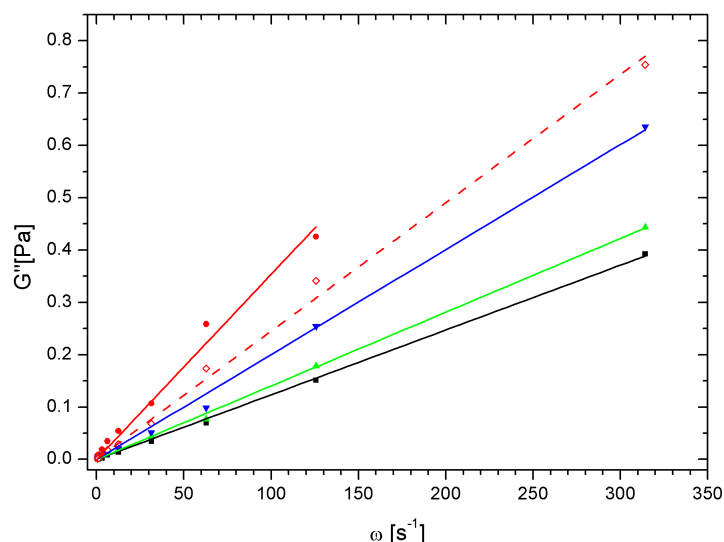
Pri enodelčni aktivni MR se s krožno frekvenco ω in amplitudo A sinusno premika lego pasti z ujeta sondo. Odziv sonde na oscilirajočo silo,

$$x(t) = D(\omega) \sin[\omega t - \delta(\omega)], \quad (6.22)$$

je odvisen od mehanskih lastnosti okoliškega medija. Njegov viskoelastični modul je moč izračunati iz izmerjenega razmerja amplitud $d(\omega) = D(\omega)/A$ in faznega zaostanka $\delta(\omega)$ za lego pasti kot [31, 98]:

$$\begin{aligned} G'(\omega) &= \frac{k_m(\omega)}{6\pi a} = \frac{k}{6\pi a} \left[\frac{\cos \delta(\omega)}{d(\omega)} - 1 \right], \\ G''(\omega) &= \omega \eta(\omega) = -\frac{k}{6\pi a} \left[\frac{\sin \delta(\omega)}{d(\omega)} \right]. \end{aligned} \quad (6.23)$$

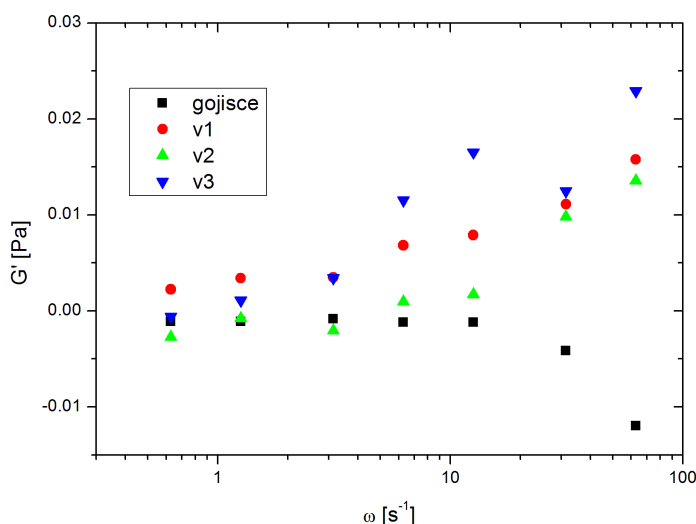
S prilagoditvijo linearne funkcije izmerkom $G''(\omega)$ po enačbi (6.21) smo za viskoznost



SLIKA 6.23: Absolutna vrednost viskoznega modula G'' rastoče bakterijske suspenzije kot funkcija krožne frekvence, izmerjen z enodelčno aktivno MR. Točkam prilagojena linearna funkcija [imaginarni del enačbe (6.21)] da naslednje viskoznosti: gojišče (črna) $\eta_M = 12.4 \pm 0.1 \times 10^{-4}$ Pas, vzorec 1 (zelena) $\eta_{S1} = 14.1 \pm 0.1 \times 10^{-4}$ Pas, vzorec 2 (modra) $\eta_{S2} = 20.1 \pm 0.3 \times 10^{-4}$ Pas, vzorec 3 (rdeča) $\eta_{S3} = 35.4 \pm 1.2 \times 10^{-4}$ Pas, vzorec 3 brez bakterij (črtkana rdeča) $\eta_{S3'} = 24.5 \pm 0.4 \times 10^{-4}$ Pas.

vode dobili $\eta = 9.1 \times 10^{-4}$ Pas. Prilagoditev linearne funkcije izmerkom $G''(\omega)$ v bakterijskem mediju (slika 6.23) so dali naslednje rezultate. Viskoznost gojišča $\eta_M = 12.4 \pm 0.1 \times 10^{-4}$ Pas je rahlo večja od viskoznosti vode, kar je smiselno, saj medij vsebuje nekaj soli in 0.4% glukoze. Viskoznosti bakterijskih vzorcev so bile $\eta_{S1} = 14.1 \pm 0.1 \times 10^{-4}$ Pas, $\eta_{S2} = 20.1 \pm 0.3 \times 10^{-4}$ Pas in $\eta_{S3} = 35.4 \pm 1.2 \times 10^{-4}$ Pas, tretjega vzorca brez bakterij pa $\eta_{S3'} = 24.5 \pm 0.4 \times 10^{-4}$ Pas. Viskoznost raztopine se s časom povečuje, saj število bakterij raste, hkrati pa se gosti ekstracelularna matrika.

Frekvenčna odvisnost elastičnega modula rastoče bakterijske suspenzije, izmerjena z enodelčno aktivni MR je prikazana na sliki 6.24. $G'(\omega)$ z večanjem frekvence narašča od vrednosti nič pri nizkih frekvencah do okoli 0.01 Pa pri visokih. Razlika med vrednostjo pri visoki in nizki frekvenci $\Delta G' = G'(60/s) - G'(0.6/s)$ je 0.013 Pa za vzorec 1, 0.016 Pa za vzorec 2 in 0.023 Pa za vzorec 3. Elastičnosti medija, ki ustrezajo tem elastičnim modulom, so po enačbi $k_m = 6\pi a \Delta G'$ enake 3.9×10^{-7} N/m, 4.8×10^{-7} N/m in 7.1×10^{-7} N/m.

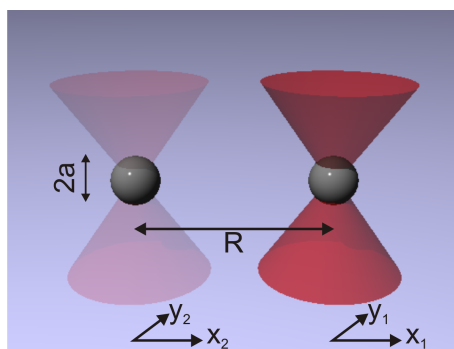


SLIKA 6.24: Elastični modul G' bakterijske suspenzije v odvisnosti od krožne frekvence, izmerjen z enodelčno aktivno MR.

Dvodelčna aktivna MR

Enodelčna reologija poda pravilne rezultate samo v primeru, če je sonda večja od vseh dolžinskih skal medija. Te omejitvi se je moč izogniti z uporabo dvodelčne MR, ki je neobčutljiva na lokalne nehomogenosti, saj meri mehanske lastnosti materiala na dolžinski skali, ki je določena z razdaljo med obema delcema.

Pri dvodelčni aktivni MR je kompleksni viskoelastični modul vzorca določen iz odziva sonde na oscilirajočo silo, ki deluje na pogonski delec (slika 6.25). Teoretičen opis odziva je tu nekoliko bolj zapleten kot pri enodelčni MR.



SLIKA 6.25: Shema dvodelčne aktive MR meritve. Kroglici z radijem a sta ujeti v dveh optičnih pasteh, šibki in močni, na razdalji R .

Če sta dva delca ujeta v optičnih pasteh, ki se nahajata na osi x na medsebojni razdalja R , lahko odmike sonde (delca 2) v smereh x in y zaradi delovanja poljubne sile $F_x^{(1)}$ oz. $F_y^{(1)}$ na pogonski delec (delec 1) v frekvenčnem prostoru zapišemo kot [103, 104]

$$\begin{aligned} x^{(2)}(\omega) &= A_{\parallel}(\omega)F_x^{(1)}(\omega) \\ y^{(2)}(\omega) &= A_{\perp}(\omega)F_y^{(1)}(\omega). \end{aligned} \quad (6.24)$$

Tu sta A_{\parallel} in A_{\perp} sestavljeni kompleksni dvodelčni odzivni funkciji v vzporedni oz. pravokotni smeri, ki sta zaradi vpliva pasti drugačni od lastnih odzivnih funkcij medija $\alpha_{\parallel}(\omega)$ in $\alpha_{\perp}(\omega)$. Sestavljeni sta iz lastnega odziva medija, trdot obeh pasti $k^{(1)}$ in $k^{(2)}$ ter odzivov posameznih delcev, $\alpha^{(1)}$ in $\alpha^{(2)}$, na zunanjo silo:

$$\begin{aligned} A_{\parallel} &= \frac{\alpha_{\parallel}}{(1 + k^{(1)}\alpha^{(1)})(1 + k^{(2)}\alpha^{(2)}) - k^{(1)}k^{(2)}\alpha_{\parallel}^2} \\ A_{\perp} &= \frac{\alpha_{\perp}}{(1 + k^{(1)}\alpha^{(1)})(1 + k^{(2)}\alpha^{(2)}) - k^{(1)}k^{(2)}\alpha_{\perp}^2}. \end{aligned} \quad (6.25)$$

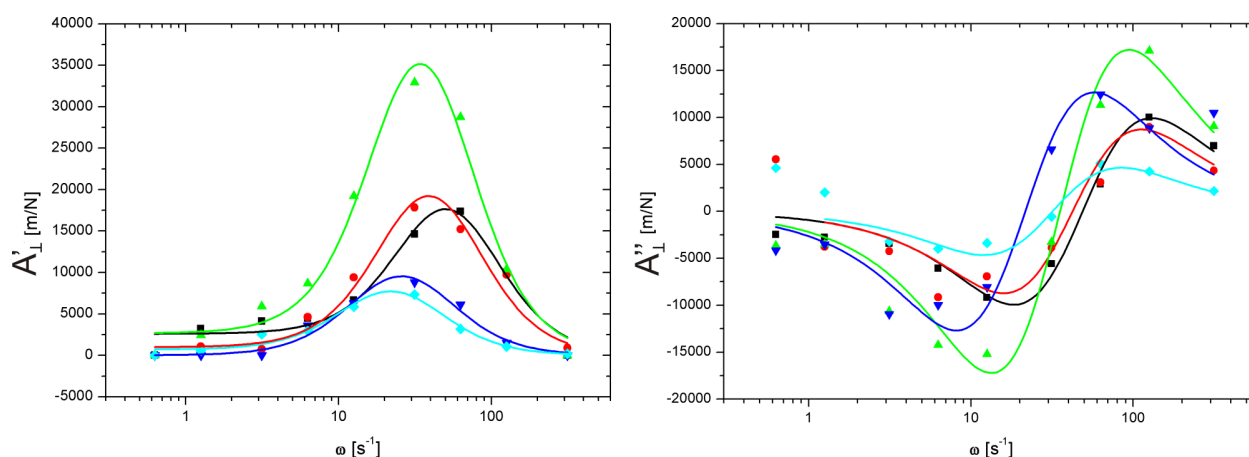
Lastne odzivne funkcije za nestisljivi kontinuum s kompleksnim strižnim modulom $G(\omega)$ opisuje generaliziran Oseenov tenzor [99]:

$$\begin{aligned} \alpha_{\parallel} &= \frac{1}{4\pi R G(\omega)} \\ \alpha_{\perp} &= \frac{1}{8\pi R G(\omega)}. \end{aligned} \quad (6.26)$$

Odzivni funkciji posameznega delca sta v našem primeru enaki, saj tako za sondo kot tudi pogonski delec uporabljamo enaki kroglici:

$$\alpha^{(1)} = \alpha^{(2)} = \frac{1}{6\pi a G(\omega)}. \quad (6.27)$$

V dvodelčni meritvi se izmeri sestavljeno kompleksno dvodelčno odzivno funkcijo kot funkcijo frekvence. S prilagoditvijo izraza (6.25) izmerkoma se ob znani trdoti obeh



SLIKA 6.26: Realni (levi graf) in imaginarni del (desni graf) sestavljene dvodelčne odzivne funkcije v pravokotni smeri. Točke različne barv prikazujejo izmerjene vrednosti v gojišču (črno), vzorcu 1 (rdeče), vzorcu 2 (zeleno), vzorcu 3 (temnomodro) in v istem vzorcu z odstranjenimi bakterijami (svetlomodra). Vrednostim je prilagojena enačba (6.25) s tremi prilagodljivimi parametri: η , k_m in skalirnim koeficientom.

pasti dobi viskoznost η in elastičnost k_m medija. Pri meritvah, ki smo jih izvedli v vodi, so se izmerjenim $A_{\parallel}(\omega)$ in $A_{\perp}(\omega)$ teoretične oblike odzivov odlično prilegale (pri parametrih: elastičnost $k_m = 0$, viskoznosti $\eta = 9.1 \times 10^{-4}$ Pas za vzporedno in $\eta = 9.2 \times 10^{-4}$ Pas za pravokotno dvodelčno odzivno funkcijo).

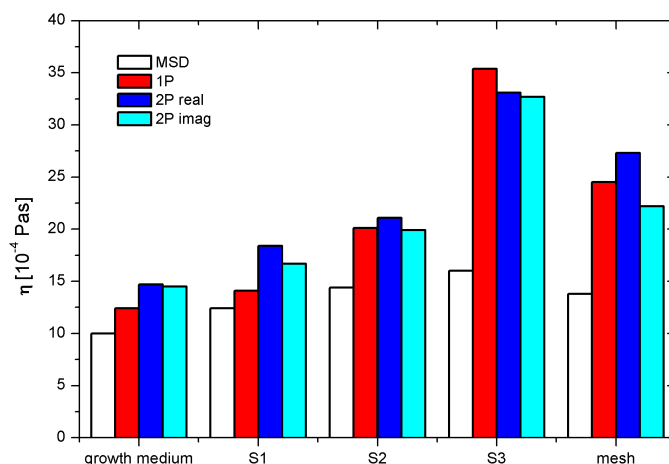
Dvodelčno aktivno MR smo nato uporabili za meritev viskoelastičnosti bakterijske mreže. Realni in imaginarni del dvodelčne odzivne funkcije v pravokotni smeri sta predstavljena na sliki 6.26. Izmerkom smo prilagodili teoretični odzivni funkciji (6.25) s tremi prilagoditvenimi parametri - viskoznostjo η , trdoto medija k_m in skalirnim faktorjem. Čeprav je bila laserska moč v pasteh v vseh poskusih enaka, imata izmerjeni odzivni funkciji $A_{\parallel}(\omega)$ in $A_{\perp}(\omega)$ v različnih vzorcih različno magnitudo, zato je bilo potrebno v (6.25) pri prilagajanju uvesti dodaten skalirni faktor. Ta ne vpliva na vrednosti viskoznosti in elastičnosti medija, saj viskoznost povezana z lego vrha realne komponente odzivne funkcije (pri višji viskoznosti se ta premakne k nižjim frekvencam), elastičnost pa se v odzivni funkciji pozna pri nizkih frekvencah .

Izmerjene vrednosti realnega dela kompleksne dvodelčne odzivne funkcije se dobro kvantitativno ujemajo s teoretičnim odzivom (6.25), medtem ko je pri imaginarni del odziva ujemanje s teorijo samo kvalitativno. Viskoznosti in elastičnosti bakterijskih vzorcev, dobljenih iz raznih dvodelčnih odzivnih funkcij, so prikazane v spodnji tabeli.

Dobljen iz:	A'_{\perp}	A''_{\perp}	A'_{\parallel}	A'_{\perp}	A'_{\parallel}
Vzorec	$\eta[10^{-4} \text{ Pas}]$	$\eta[10^{-4} \text{ Pas}]$	$\eta[10^{-4} \text{ Pas}]$	$\mathbf{k}_m[10^{-8} \text{ N/m}]$	$\mathbf{k}_m[10^{-8} \text{ N/m}]$
Gojišče	14.7	14.5	14.9	15	0
Vzorec 1	18.4	16.7	17.2	4.9	9.4
Vzorec 2	21.1	19.9	21.8	7.4	9.8
Vzorec 3	33.1	32.7	34	8.8	10
"Samo mreža"	27.3	22.2	25	0	7.4

Sklepi

Na sliki 6.27 so povzeti rezultati meritev viskoznosti gojišča in bakterijske suspenzije v adaptivni (S1), logaritemski (S2) ter stacionarni fazi (S3) z različnimi MR metodami. Enodelčna pasivna MR je sicer zaznala povečevanje viskoznosti, toda vrednosti se v primerjavi z drugimi metodami zdijo močno podcenjene. Rezultati enodelčne aktivne MR so bili podobni rezultatom dvodelčna aktivne MR - izmerki v vseh vzorcih so znotraj $\pm 10\%$ povprečne vrednosti. Viskoznost suspenzije s staranjem narašča do $\eta \approx 3.3 \times 10^{-3} \text{ Pas}$, njena elastičnost pa je velikostnega reda $k \sim 10^{-7} \text{ N/m}$.



SLIKA 6.27: Primerjava izmerjenih viskoznosti η vzorcev z enodelčno pasivno MR (belo), enodelčno aktivno MR (rdeče) in dvodelčno aktivno MR (temnomodro - realni del, svetlomodro - imaginarni del dvodelčne odzivne funkcije).

Izjava o avtorstvu

Spodaj podpisani Natan Osterman, univ. dipl. fiz., izjavljam, da sem samostojno izdelal pričujočo doktorsko disertacijo in sem njen avtor.

V Ljubljani, 25.5.2009

Natan Osterman